# Final Project Report:

# Three Integrated Projects to Enhance Non-Contact Rail Inspection Technology for Application to Substructure Health Evaluation on Both Rail and Road Bridges

by
Dr. Elizabeth K. Ervin, Principal Investigator
Dr. Vyacheslav Aranchuk, Co-principal Investigator
Dr. Christopher Mullen, Co-principal Investigator
Dr. James Chambers, Co-principal Investigator

Civil Engineering, Mechanical Engineering, and the National Center for Physical Acoustics
The University of Mississippi
Box 1848
University, Mississippi 38677

NCITEC Project No. 2012-24

conducted for

NCITEC

January 2014

DISCLAIMER

*The contents of this report reflect the views of the authors, who are responsible for the facts and the accuracy of the information presented herein. This document is disseminated under the sponsorship of the Department of Transportation University Transportation Centers Program, in the interest of information exchange. The U.S. Government assumes no liability for the contents or use thereof.*

# ABSTRACT

Causing loss of use and sometimes life, bridge collapses are always high profile and hit many wallets. The economic benefits of condition-based maintenance are well established, including reduced visual inspection and potentially longer structural life. More accurate estimation of remaining life could potentially prevent collapse but, at a minimum, will aid decision-making on a bridge's upkeep.

This project has extended rail technology towards the generation of an inspection methodology for bridge substructure. Non-destructive optical inspection techniques have been used for assessment of rail structural integrity, but lasers have not been employed for assessment of supporting components underneath the rail. Employing a laser Doppler vibrometer, tiny surface vibrations can be measured that reach into substructural components, including rail ties, bridge deck, piers, footings, and soil. Contact non-destructive testing methods have been used for assessment of structural integrity but only in selected locations, which limits their practicality for inspection of large infrastructure. Due to the size of rail and road bridges, large spacing between test locations can result in poor motion capture and thus missed defects. The non-contact vibrometer overcomes this obstacle, quickly providing measurements at a single location or even while moving.

Results are presented for three experimental efforts: a railroad, a scaled reinforced concrete bridge, and an operational on-campus bridge. Traditional cabled accelerometer sensing was used as a basis to determine the feasibility of a vibrometer as an infrastructure inspection tool. The series of experiments reveal that the LDV velocity signals are sensitive enough to use for damage detection in bridges. Once attached to a sturdy base, the moving vibrometer also provided good resonance information despite some slight interference. Limitations include measurement distance and geometrical resolution. In-service traffic excitation is sufficient to provide modal information, and the best case would be multiple large vehicles traversing the bridge at various speeds.

Considering noise and sensitivity issues, a structural health evaluation program was developed to efficiently extract modal information and apply multiple health indicators. Modal comparisons between finite element models and processed experimental data show similarities as well as assist in the challenge of coordinating baseline to damaged modes. The program quantitatively contrasts modes to visualize damage level and location, allowing judgments on damage severity and further inspection needs. This achieves the technical aim of identifying global dynamic property changes resulting from local component damage.

Civil structures are ideal damage detection applications because they experience incremental changes while aging. On the other hand, the associated signal processing can be extremely challenging due to such low frequency resonances. Field measurements did demonstrate the ability of optical vibrometry to remotely monitor bridge motions, advancing inspection of transportation infrastructure. More research is needed to determine ideal indicators and their "safe" thresholds for various classifications of structures.

Enhancing public safety and economic competitiveness, real-time health evaluation and condition-based maintenance are the ultimate aspirations, and a potential product could be a mobile inspection vehicle that would ride along any bridge. The precursory sensitivity studies herein demonstrate that the concept would work: at least one vibrometer on a moving vehicle would be able to provide dynamic bridge data which could then be quickly post-processed to visualize damage level and location. This would indicate that localized inspection and repair action is required before a bridge collapse, for instance.

# ACKNOWLEDGMENTS

The researchers thank Atlantic Track and Turnout in Memphis, Tennessee, with a home office in New Jersey. Jeff Grissom, Director of Engineering and Manufacturing, and Pat Reilly, Manager of Railroad Products, donated the following rail materials to this project: 16 tie plates, 2 splice plates, 32 e-clips, 50 screw spikes, 32 feet of new cross tie, 20 feet of used cross tie, and two 10-foot rail sections.

The researchers also thank B&B Concrete of Oxford, Mississippi, and their home office in Tupelo, Mississippi. Bill Waters, Vice-President, was very responsive and helpful with mix design and form checking. Dean Black provided for dispatch, and we are certain that David Brevard had a financial hand in the concrete donation.

# TABLE OF CONTENTS

# LIST OF TABLES

# LIST OF FIGURES

# INTRODUCTION

American infrastructure is in a precarious state. Bridges are susceptible to damage through both aging and abnormal events, and their remaining life is difficult to estimate. For example, the gusset plate defect was known before the I-35 collapse in Minneapolis; the effect of that local inspection to the overall health of the structure was not identifiable. The technical gap is the identification of global dynamic property changes resulting from significant local component damage, such as stress corrosion cracking, a barge impacting a pier, or hurricane storm surge.

Rail inspection techniques are well developed but have not been applied for substructural evaluation. Current non-destructive inspection methods can be used for assessment of structural integrity of rails themselves, but they cannot assess structural components under the rail, such as rail pads, fastening systems, sleepers, bridge deck, and other bridge components. Rather than a static laser displacement meter, a laser Doppler vibrometer can measure tiny rail vibrations that can provide structural information about the rail support conditions. This dynamic measurement is an extension of current railroad inspection technology to railway or roadway evaluation.

While dynamic inspection measurements can provide valuable information on general structural integrity, analysis methods are not yet capable of defect location. Traditional instrumentation in the form of accelerometers has been successfully used for both rails and their substructure (*1-9*); however, these methods can only be used at pre-selected point locations via contact. This instrumentation scheme is difficult to install and often misses defects. Thus, non-contact techniques are prescribed by wide-ranging use and rapid deployment (*10*).

Damage detection is further complicated in real structures (*11-13*). To better quantify comprehensive structural damage, a rapid assessment tool is needed. Ideally, every structure would be "smart" by having an automated monitoring system that could immediately warn the public of any unsafe condition. Before this scenario becomes a reality, numerous questions need to be answered with a specific focus on massive structures. Infrastructure serves as the greatest challenge for dynamic assessment due to its low frequency and low excitation levels. Any measurements made during normal operation have high noise levels as motion is minimal. Farrar ***et al.*** (*14*) establishes the needs of data acquisition and cleansing, feature selection, and statistical model development. Based upon a study of an I-40 bridge, he also notes that evaluation methods may be less sensitive than environmental factors or signal to noise ratios. Pavic ***et al.*** (*15*) also point out that the massive size of civil structures makes artificial excitation very difficult: sufficiently exciting a massive building is difficult, especially without creating additional damage. Both the level of damage and its location is important; as one member fails, others must carry the displaced load, causing increased stress and risk of progressive failure.

Considering these issues, this integrated effort extends rail technology towards the generation of an inspection methodology for bridge substructure. The three applied research efforts herein aspire to attain the goal of advancing inspection of transportation infrastructure in order to improve public safety and economic competitiveness. In other words, the eventual aim is to provide condition-based maintenance via a cost-effective product that will ride along any bridge and identify an overall change in its stiffness, indicating that localized inspection is required before a bridge collapse, for instance.

# OBJECTIVE

This integrated effort advances non-contact rail inspection technology to evaluate substructural health. Usage of non-contact techniques enhances inspection of transportation infrastructure in order to improve public safety and economic competitiveness. Including sensitivity and detection concerns, the main objective is the determination of structural state from local materials to global assembly at any instant. This objective was achieved by computational evaluations on three experimental setups. Employing state-of-the-art non-contact measurement, the data from these experiments was used to assess various structural health algorithms as well as finite element models.

The five primary activities of the project are individually detailed here as well as separated in the Methodology and Results sections.

1. Experiment 1: Non-Contact Rail Inspection

A mock railway track with substructure was constructed outside the National Center for Physical Acoustics (NCPA) on the University of Mississippi (UM) campus. Test design included the track itself, vibration excitation, vibration measurement, and data acquisition. Experiments were conducted to measure the dynamic characteristics of the railway structure. The measurements were made with a contacting accelerometer (for verification), a stationary laser Doppler vibrometer (LDV), and an LDV on a moving platform. Test cases included several artificial defects in railway track components. The frequency contents of the signals were post-processed with health algorithms.

2. Experiment 2: Bridge Scale Model

A mock bridge was constructed on the UM campus. The structure was designed and built by students since the as-built configuration is the comparison baseline. The instrumentation scheme included vibration excitation, vibration measurement, and data acquisition. Experiments were conducted that measured dynamic characteristics for different levels of defective pier substructure components, simulated by variable bearings. The frequency contents of the signals were post-processed with health algorithms.

3. Experiment 3: Full Scale Bridge Test

No developed methodology can be valid without application to a full scale bridge. An on-campus bridge (Eastgate Bridge on University Avenue) was tested for a baseline comparison to the laboratory scale model. The frequency contents of the signals were post-processed to determine sensitivity of potential health algorithms.

4. Structural Health Monitoring (SHM) Algorithm Development

The specific technical need is the determination of proper damage indication and its threshold beyond which structural failure will occur. The structural health tasks for each data set initiated with reformatting collected data as MATLAB input. Then system information was extracted from measurements. This includes transfer functions, effective system matrices, and modal parameters: this modal decomposition step was not trivial. The last step was to apply damage detection statistical routines to the data. Twelve different routines were programmed, and graphical output was generated for the inspector's benefit.

5. Finite Element (FE) Modeling

This effort considered the scalability of damage detection algorithms from destructive scale model testing to bridge field test. The modeling also aids in examining the effects of local damage on global structural response. Multiple commercial packages were used for the finite element modeling, and their use in health matters was evaluated.

Note that these activities work toward the same end of improved infrastructure inspection. For the first time, the work linked multidisciplinary personnel and facilities in UM Civil Engineering, Mechanical Engineering, the Multi-Function Dynamics Laboratory, and the National Center for Physical Acoustics.

# SCOPE

Technical limitations of this project stem from the project's preliminary nature. While successful damage indicators were identified and explored, the methodology cannot be guaranteed to work for all structures or even all bridges. No developed methodology can be valid without application to a variety of infrastructure. The on-campus bridge test was a single event with a single specimen and thus is not sufficient to extrapolate to all bridges; however, this data did provide noise level analysis considering such factors as excitation, temperature, and reflectivity. This allowed for baseline calibration as well as revealed any potential data collection problems. On-going UM work is further analyzing each indicator and its effectiveness in identifying damage present in various materials and geometries in order to draw broader conclusions.

The long-range hypothesis yet to be proven is that separate classifications of structures will require different damage detection metrics. Once the most effective indication method for a structural system type has been determined, the safety threshold can be determined. This method and its associated threshold parameters will aid decision-making on maintenance based upon structural condition. The ultimate goal is to limit the total damage caused by all abnormal events as well as aging throughout the structure's lifetime to an allowable "safe" threshold.

The technical scope is also limited to overall health (and global modes), so subsequent local inspection may be indicated. Locating of potential damage is still extremely valuable for more pointed inspection and maintenance. To be feasible, the employed health evaluation technique should be more sensitive, reliable, and cost-effective than currently employed visual inspection methods.

Another technical restriction in health evaluation is that large damage events may alter the modal response of the structure such that subjective modal comparisons become even more uncertain. This means that mode shapes calculated from large damage events cannot always be visually compared to baseline mode shapes due to coupling of modes which can cause extreme visual differences between the two cases. Closely spaced modes can also prove troublesome since large modal peaks that can dwarf smaller peaks. There is also a lower frequency limitation based upon instrumentation and post-processing; this can interfere with massive infrastructure, which have low resonant frequencies.

Based upon specific use, the LDV also has its own technical limitations. Speckle noise can mask small vibrations and result in missing structural defects (*16,17*). Speckle noise depends on the reflectivity of the target surface, geometrical parameters of the LDV beam, and Doppler signal demodulation and processing. Additional research is required to estimate the effect of speckle noise on LDV performance for detection of structural defects.

Note that the finite element analyses herein played supporting roles to the planning and evaluation of the project's experiments. Thus, these studies were well reasoned but not exhaustive in nature. A 2013 NCITEC research effort will address component damage effects more thoroughly.

This study does not attempt to produce a deliverable inspection product. While this is a potential application, it is not the stated goal of adapting rail inspection technology for bridges. The precursor techniques and sensitivity studies are undertaken herein that would eventually lead to an innovative health evaluation apparatus. A simplified concept vehicle is shown in Figure 1: an LDV is mounted on a railroad car and is incident on the rail. As the car moves, its wheels excite vibration of the railway track structure. The LDV continuously

measures the vibration of the unconditioned rail down to a nanometer during car motion. Requiring much additional research, the car's suspension system will help to decouple the LDV from rail vibration; thus, measurements will provide dynamic characteristics of the structure and its substructure.

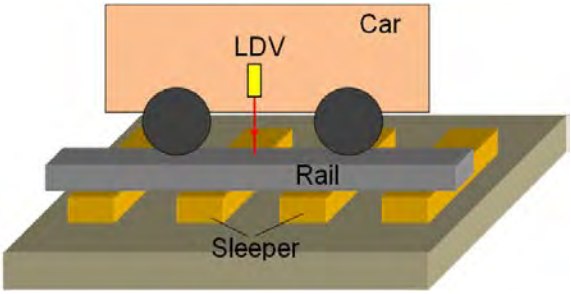


**Figure 1. Concept of rail vibration measurement from a moving platform.**

The speed of the moving LDV measurements was not considered in this study. The maximum speed of an instrumented car is a product of required frequency and special resolution. For example, typical numbers that assure defect detection are 10 centimeters (cm) spatial and 10 Hertz (Hz) frequency resolution, which calls for a speed of 1 m/s. In order to increase the traveling speed to a more reasonable number, time-division multiplexing of multiple LDV beams can be used and would be a good future research effort.

Once the portable inspection product is completed, the stakeholders will include the public at-large, via improved safety and tax dollar efficiency, as well as state transportation departments, via more pointed and cost-effective maintenance. These benefits of improved infrastructure management will aid response to both aging and abnormal events.

At this time, the developed structural health program is limited to internal use only. The program has been designed with maximum applicability and visualization, but the interface will need much attention before delivery to any agency. While publications have resulted, technology transfer will eventually involve code considerations and inspection workshops. Educational impacts for both undergraduate and graduate students did transpire during this project.

# METHODOLOGY

In this section, the methodology behind all five primary activities will be discussed.

## 1. Experiment 1: Non-Contact Rail Inspection

The experimental setup of a mock railway track was the first experimental setup to be constructed. The rail was typical for transport using common attachments, and building a full-scale monorail saved resources. Donated by Atlantic Track and Turnout, the rail weighed 115 pounds per yard, a medium heavy rail. Tie plates were attached to the ties by four screw spikes each. The rail then lay upon the tie plates and was secured by an “e-clip” (spring clips so called because they look like a lower case “e”) on each side of the rail. According to Jeff Grissom of Atlantis Track & Turnout, a two-foot bed of #4 crushed limestone is considered the minimum bed for tracks. The limestone should be compacted in layers of 10", 8", and 6". #4 limestone has a size of 1"-1.5", but this was not available locally; crushed limestone of .75" to 1" was substituted.

Construction began on the railroad bed outside the National Center for Physical Acoustics building in November 2012. A trench was dug 1' deep x 4' wide x 13' long. It was filled with approximately 11" of loose limestone that was compacted to 10". Limestone was added to bring the total depth to 19" and compacted depth to 18" total depth. 8" of gravel running across the bed was removed. In order to physically model the damage mechanism of tie settlement, five stainless steel sheets were placed in that location. The compactor was run over the bed again to smooth the bed for the placement of the ties. These bed preparation steps are documented in Figure 2.

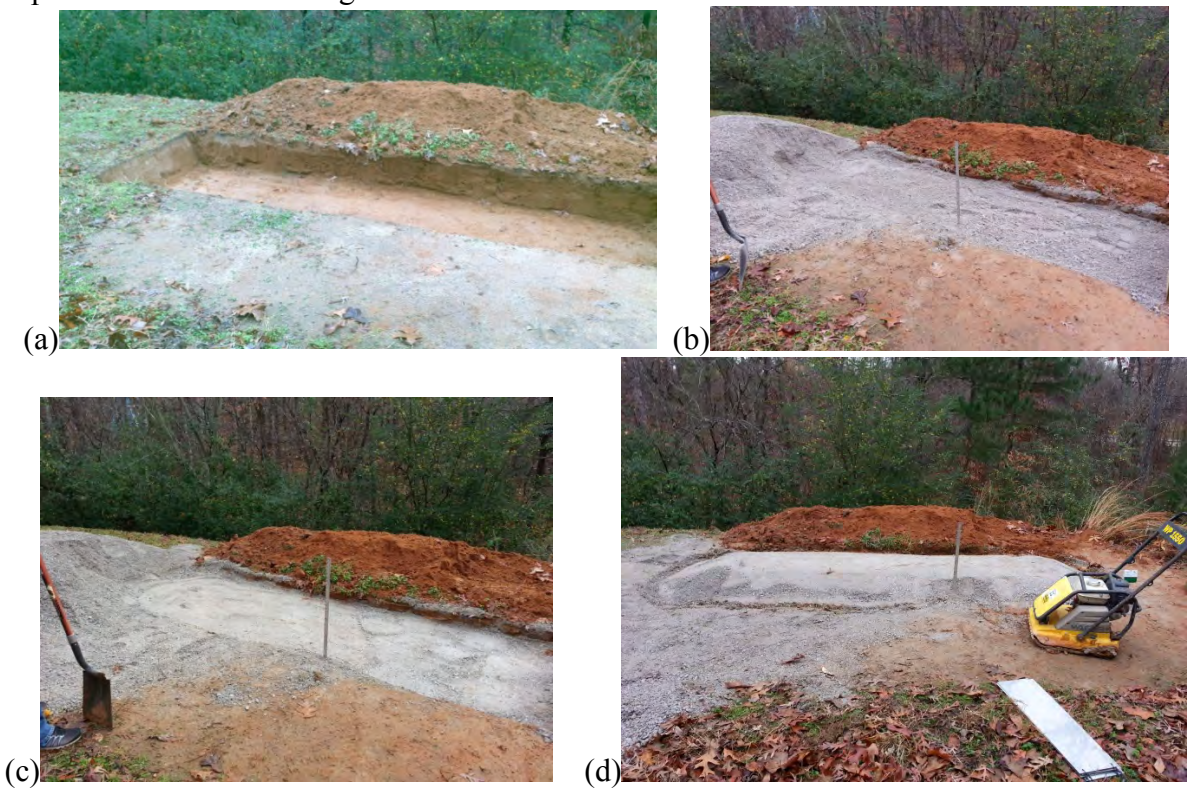


**Figure 2. The rail setup under construction.**

Typical railroad ties were cut in half and then placed on the bed starting at center over the stainless steel plates. They were spaced 19.5" on center, the industry standard. The remaining limestone filled between and was compacted even with the tops of the 6" tall ties, bringing the total depth to 24". The tie plates were placed on top of the wooden ties. The rail was placed in the saddle of all seven tie plates. With the tie plates now properly located, holes for the screw spikes were predrilled in the ties. The screw spikes were installed four per plate with an electric impact wrench. Two e-clips were installed on each tie plate to hold the rail, with the exception of the ends where only one clip could be installed. The result is shown in Figure 3.

**Figure 3. The completed rail setup.**

The monorail's construction was completed as of December 2012. The instrumentation evaluations and associate testing are described herein. The measurement capabilities of the laser Doppler vibrometer (LDV) were examined, and then the rail instrumentation scheme was designed. One measurement setup that was originally designed for soil characterization was eliminated since the LDV on its moving platform induced too much vibratory interference.

The frequency response of LDV Model PDV100 (Polytec, Inc.) in the frequency range from 0.5 Hertz (Hz) to 10 Hz was measured. A standard accelerometer (PCB 356B18) mounted on a shaker has been used as reference sensor. The accelerometer has a constant frequency response from 0.3 Hz to 5000 Hz. The shaker vibration was measured simultaneously by the LDV and the accelerometer. The normalized ratio of vibration velocity measured by the LDV and accelerometer versus frequency is shown in Figure 4. This reveals the excellent news that LDV provides good response correlation, specifically after 2 Hz.

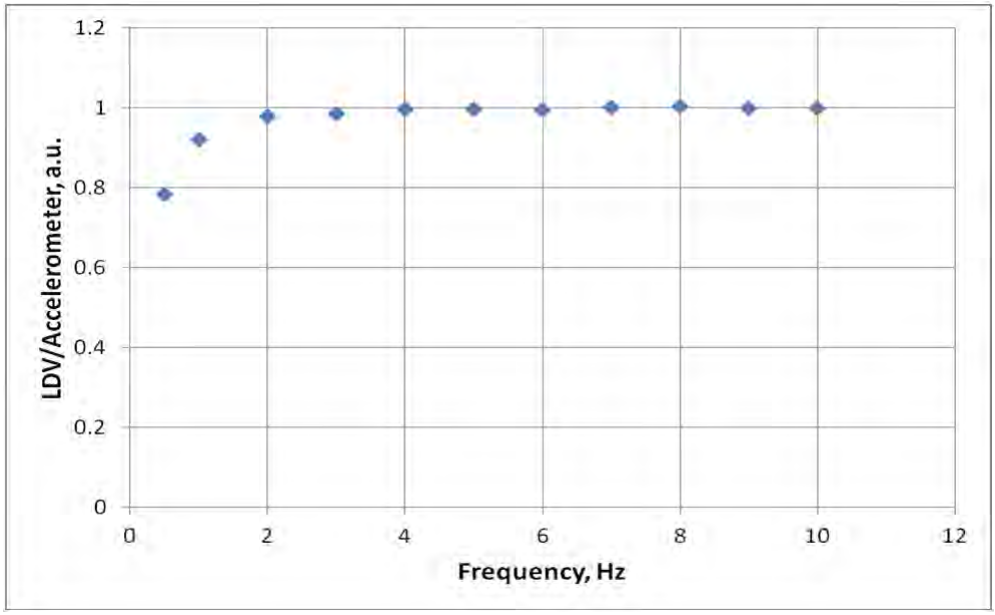


**Figure 4. Frequency response of the LDV PDV100 in the frequency range from 0.5 to 10 Hz.**

Vibration of the rail excited by impact has been recorded using both the LDV and the accelerometer. Photographs of the experimental setup are shown in Figures 5 and 6. The LDV was positioned on a concrete pavement at 340 cm distance from the rail. The LDV height was 198 mm, and its sensitivity was $5 \times 10^{-3}$ m/s/V. The LDV sensitivity to out-of-plane vibration was reduced by half because the angle between the vertical and the laser beam was 30.4 degrees. The accelerometer sensitivity was $9.8 \times 10^{-6}$ m/s$^2$/V (102 mV/(m/s$^2$)). The accelerometer was mounted on the rail as shown in Figure 2; the beam of the LDV mounted on a tripod was incident onto the rail surface close to the accelerometer. Retroreflective tape on the rail surface enhanced reflectivity. The rail vibration was excited with a single plastic hammer impact. Note that plastic material lowers the high frequency content of the signal so that lower frequencies were better observed.


**Figure 5. Photograph of the instrumented rail experiment for LDV sensitivity.**

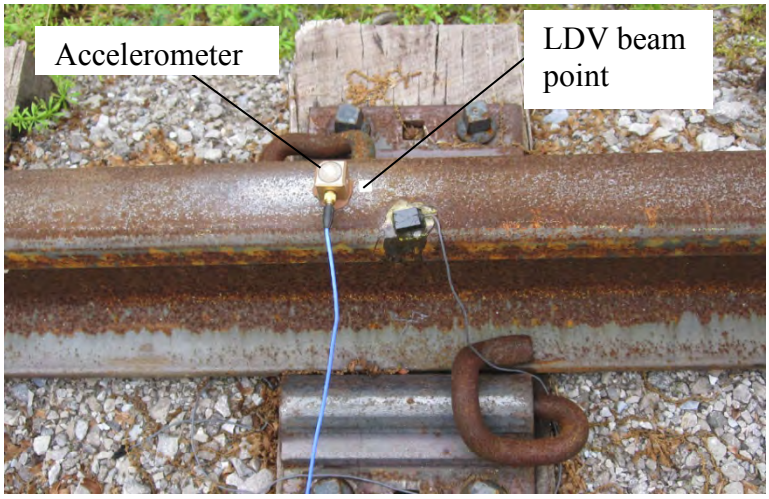


**Figure 6. Measurement target area.**

The LDV and accelerometer signals were recorded using a digital oscilloscope, Agilent Infinium 54831b. The sampling rate was 20,000 Samples/second. The record length was 6.55 seconds (131,072 points). Both the LDV and accelerometer were DC-coupled. An example of the LDV and accelerometer signals is shown in Figure 7. The low frequency component in the LDV signal is most likely due to the LDV tripod's vibration. In order to measure low frequency vibration of the rail track structure, the LDV should be mechanically decoupled from the ground.

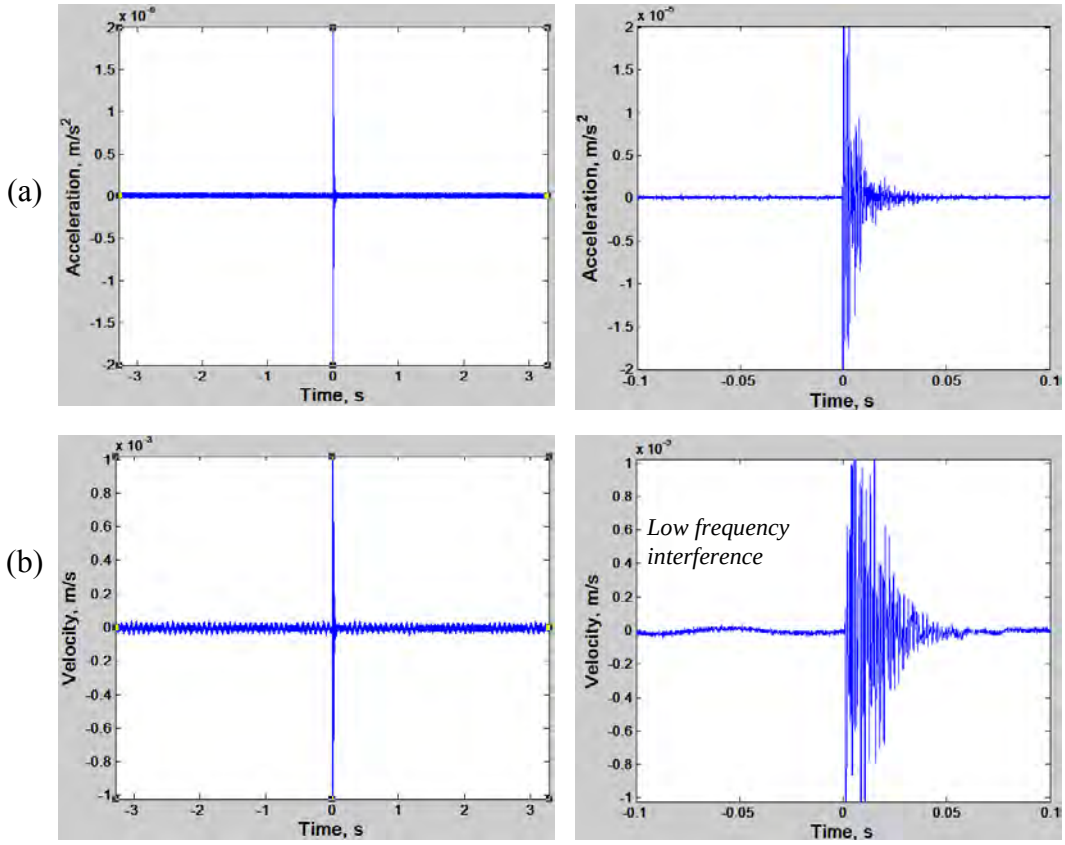


Figure 7. Rail vibration event measured with (a) the accelerometer and (b) LDV for different time scales.

Another experiment was performed to verify the idea that low frequency component in the LDV signal was caused by the tripod response. The LDV beam was directed downward to concrete pavement coated with a retroreflective tape, as shown in Figure 8. The LDV and the accelerometer signals were recorded as the hammer hit the rail. The signals obtained demonstrate again that the LDV signal exhibits low frequency component while the accelerometer does not. The LDV's additive low frequency component is caused by the LDV's vibration itself.

To obtain more usable data from the vibration test on the rail, other configurations need to be considered. To check if the structure produces measurable vibrations at low frequencies, a harder hit is needed with a hammer that transmits more energy into low frequency vibration. The accelerometer should be calibrated for the seismic range, a high sensitivity low frequency accelerometer. If the vibrations are within the LDV range, a new setup is needed to reduce the low frequency interference of the tripod. One past means of this is to use the LDV mounted on a massive platform. As shown in Figure 9, a forklift was used previously to measured ground vibration caused by an impact in a tunnel (*16,17*).

Figure 10 shows the final schematic of the experimental setup for temporal measurements on the rail. Vibration of the monorail structure was excited using an impact on the rail at a point located approximately ten centimeters from the right end of the rail. The resulting vibration over the center tie was measured with a LDV and an accelerometer simultaneously. The LDV (PDV 100, Polytec, Inc.) was mounted on a motorized linear stage,

which was then attached to a massive platform fastened to a forklift. The accelerometer was attached to the rail surface as a basis for comparison: the LDV beam was pointed onto the rail surface near the accelerometer. The captured signals were digitized using an A/D converter and saved into a computer memory. Side and top view photographs of this setup are shown in Figure 11.

**Figure 8. Setup for measuring LDV tripod response.**

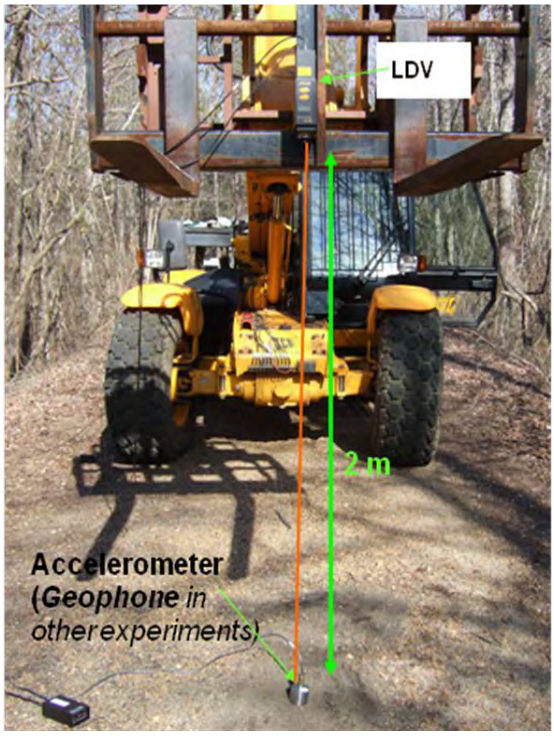


**Figure 9. LDV mounted on the forklift to measure vibration of the ground.**

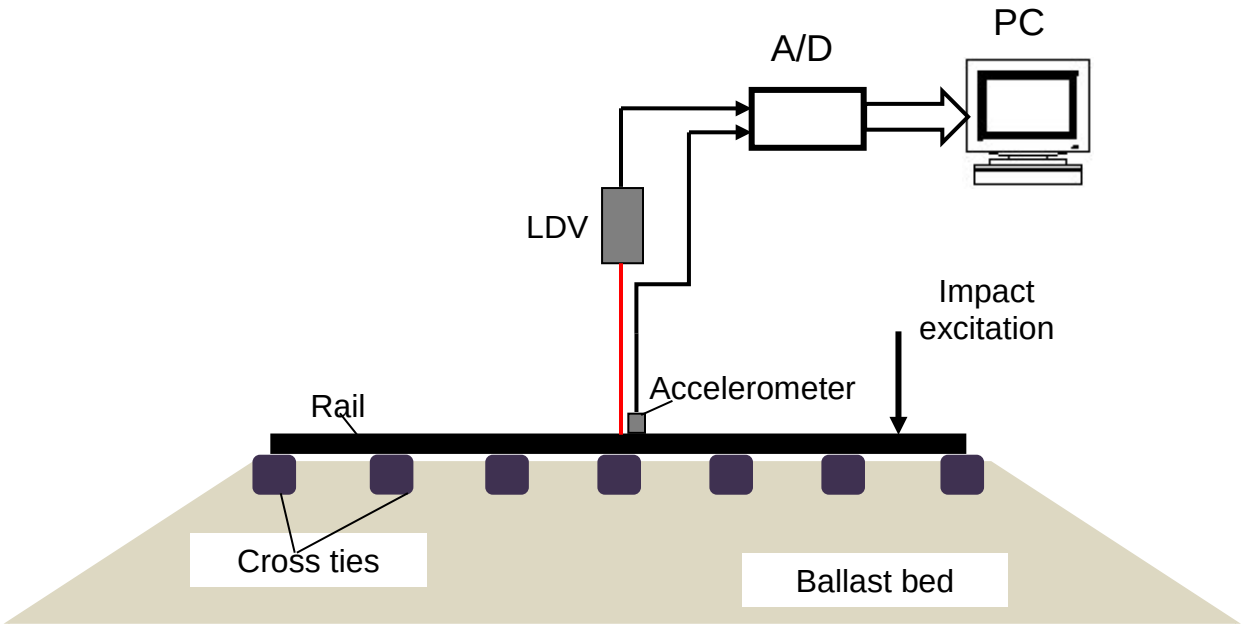


**Figure 10. Schematic of the final rail test setup.**

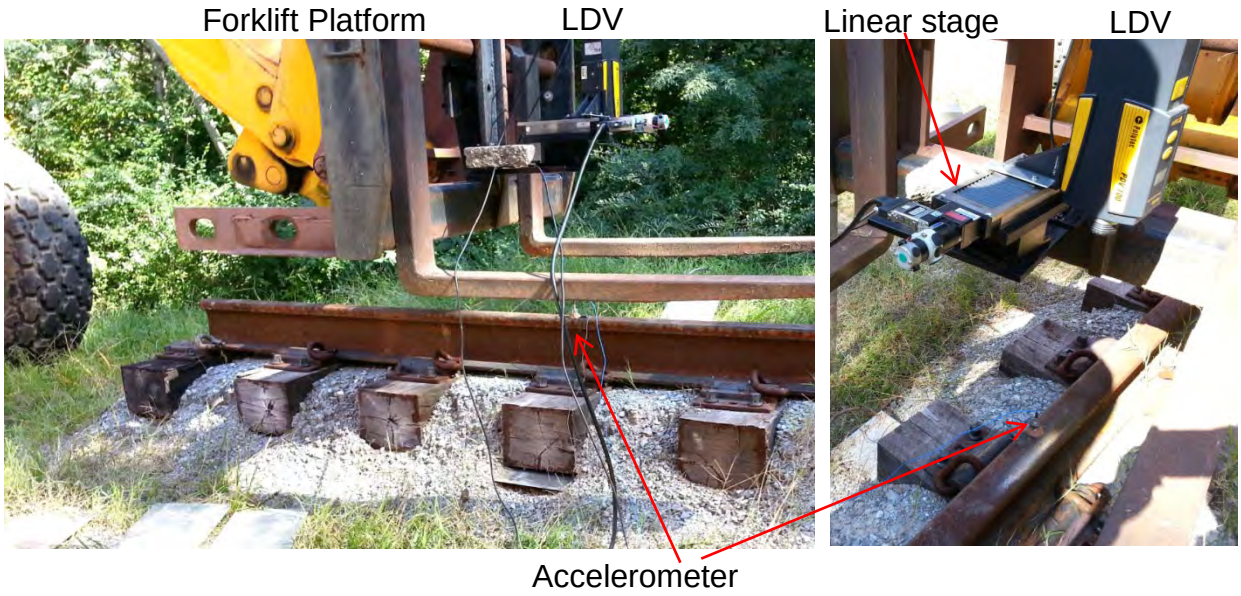


**Figure 11. Photographs of the final rail experiment.**

Structural defects have been induced at the center tie, and measurements occurred in the two nearby spans. Twenty-eight different damage cases were recorded: these varied from removal of screws, e-clips, and tie plate to center tie settlement. These results were compared to the undamaged baseline, or "as-built" configuration.

Vibration response of the railway track with different defects was measured with the LDV in two modes: stationary and moving. The ultimate goal is to have a moving instrument that could be driven across a rail or bridge that could be sensitive enough to measure target vibrations without interference from the vessel. To this end, the moving measurement is quite important and needs to be contrasted to the stationary measurement. The linear stage has a motor that continuously moves the LDV along the rail with its maximum speed of 20 mm/s. Each LDV measurement was completed in parallel with the accelerometer measurement for verification.

## 2. Experiment 2: Bridge Scale Model

A scale model bridge was built for expanded testing based upon the dimensions of the Eastgate Bridge located on University Avenue. As illustrated by SAP2000 (*18*) in Figure 12, attention was first focused on creation and analysis of a 3D finite element (FE) model to guide design and construction of the scale highway bridge test configuration to ensure measurable modal properties under load test vibration conditions. For ease of construction, the bridge scale model has been designed to have reinforced concrete deck slab in three sections and an integrated concrete pier wall and footing. The abutments were designed to model embankments with pier walls, but the end boxes were not required after construction.

The model was used to investigate several scale dimensions from 1:10 to 1:15, and the 1:12 offered the best frequency range at a workable dimension in the laboratory space available at the NCPA. It was important to model the bridge as accurately as possible, maintaining the characteristics of its larger counterpart. The scale model bridge consisted of two inverted T-shaped piers, two end slabs with shear keys, two end walls, and one center slab. Note that the slab thicknesses were not to scale: since a two-inch slab is impractical, a six-inch minimum slab thickness was used for enough rebar cover. Plans for a backup center slab were also included, but due to the volume of concrete delivered, the form was not able to be filled to its designed height and therefore served as a possible additional damaged case. The scale model bridge pieces were precast; the forms were built and transported outside of the NCPA building for a single concrete pour. After 35 days, the pieces were unformed and assembled inside of the lab.

Adjustable rubber bearings were designed to simulate bearing and substructure damage/weakening. Sample moduli and sizes were obtained from a manufacturer of rubber pads up to 1/2 inch thickness and four-inch wide strips that can be cut as needed.

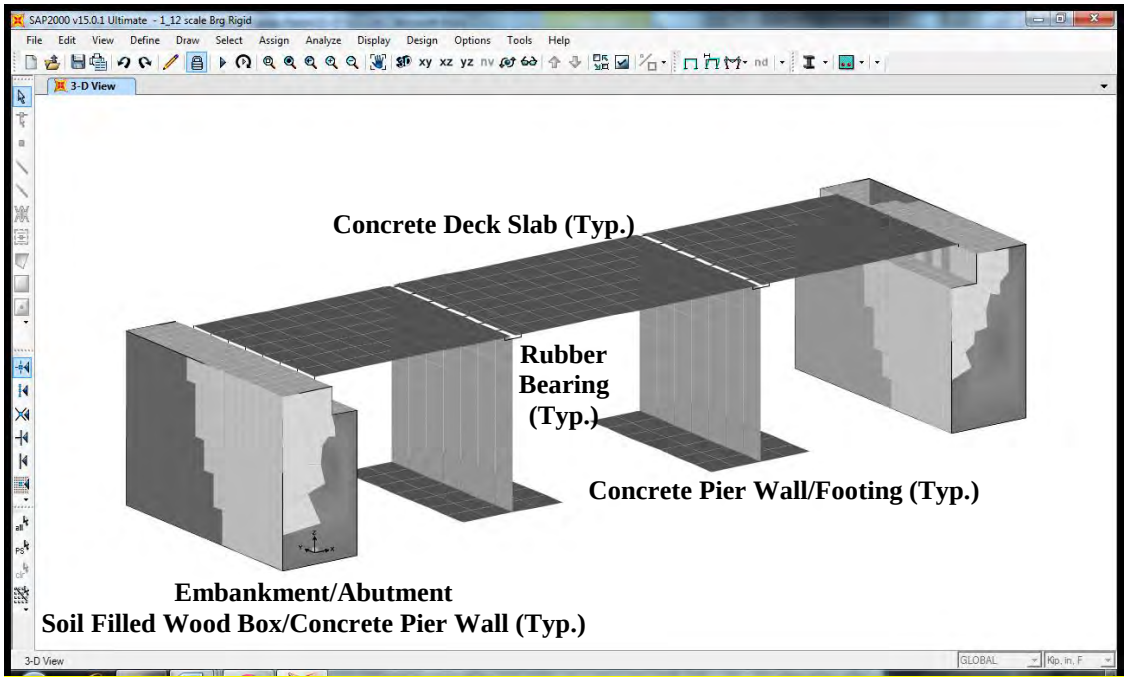


**Figure 12. Initial SAP2000 design of the scale model bridge.**

Figure 13 visually displays the timeline for completion of the scale model bridge. The design took place in Fall 2012 by Dr. Mullen's team. Detailed technical considerations are described in a Master's thesis (*20*). The planning and construction of the forms – which took over 150 manhours to complete – occupied the majority of the allotted time, taking 65 days to complete. Thirty-five days elapsed from the concrete pour to the scale model bridge move date. During this "waiting period," the concrete was allowed to cure past the 28-day mark so that it had gained over 90% of its strength. The final move on May 10, 2013, took under five hours using a forklift and occurred without introducing any visible damage to the scale model bridge pieces.


**Figure 13. Model bridge construction timeline.**

Planning and construction of the forms was carried out by Gary Bell, an undergraduate civil engineering student with previous field work experience, with the assistance of Ty Gunter, another undergraduate civil engineering junior. They were supervised by PI Dr. Ervin and graduate student Steven Worley. Form construction began with the end slabs, shown in Figure 14. The design of the end slabs includes a shear key which was added for increased longitudinal stability of the finished scale model bridge. This induces safety by increasing slab sliding resistance as well as end wall tipping resistance. The end slab measures 54x42x6-inches with the shear key measuring 3x42x8-inches. Forms construction proceeded with construction of the center slab form, shown in Figure 15. The center slab measures 60x42x6 inches.

**Figure 14. The first of two end slab forms.**

**Figure 15. The second of two center slab forms.**

The remaining bridge forms were also constructed for the t-shaped piers and end walls, shown in Figures 16 and 17. Integrating slab support with the footing, the t-shaped piers were formed and poured upside down for two reasons: only a single pour was needed, and the possibility of introducing air voids in the finished pier was reduced, effectively eliminating the need of a concrete vibrator. The large base on the t-shaped piers also allowed for increased scale model stability during laboratory testing. The measurements for the t-shaped piers are 32x42x13-inches for the bottom section and 8x42x23-inches for the top section. The end walls were formed as a simple rectangular slab measuring 36x42x6-inches.

**Figure 16. The first of two t-shaped pier forms.**

**Figure 17. The second of two end wall forms.**

The forms were wired in order to support reinforcement for the scale model bridge pieces. Preliminary calculations indicated that no reinforcement was necessary, but reinforcement was added in order to achieve consistency between the scale model bridge and its counterpart. The reinforcement chosen was the available #4 rebar and was placed with consistent cover for each of the forms. Each of the three slabs has two longitudinal reinforcement bars. Poured horizontally for consistency, the end walls have three vertical reinforcing bars once in place. The t-shaped piers have three vertical and two horizontal reinforcing bars: the bars were wired together for cross-coupling. The bars are located for all pieces in Figure 18.

After construction and wiring of the forms for reinforcement, the forms were coated with motor oil in order to allow for easy cast removal. Motor oil was applied in coats over the course of five days in order to allow the oil to penetrate the wood, leaving an outer coat during the concrete pour. The oiling of the forms proved to be a useful and successful endeavor as the pieces were removed from the forms without much trouble, yielding excellent results.

Concrete for the scale model bridge was poured on Friday, April 5, 2013, beginning at 12:07pm. Each of the forms was placed on a separate pallet outside of the NCPA before the pour as seen in Figure 19. The forms were then wetted in order to provide additional protection against the concrete sticking to the forms.

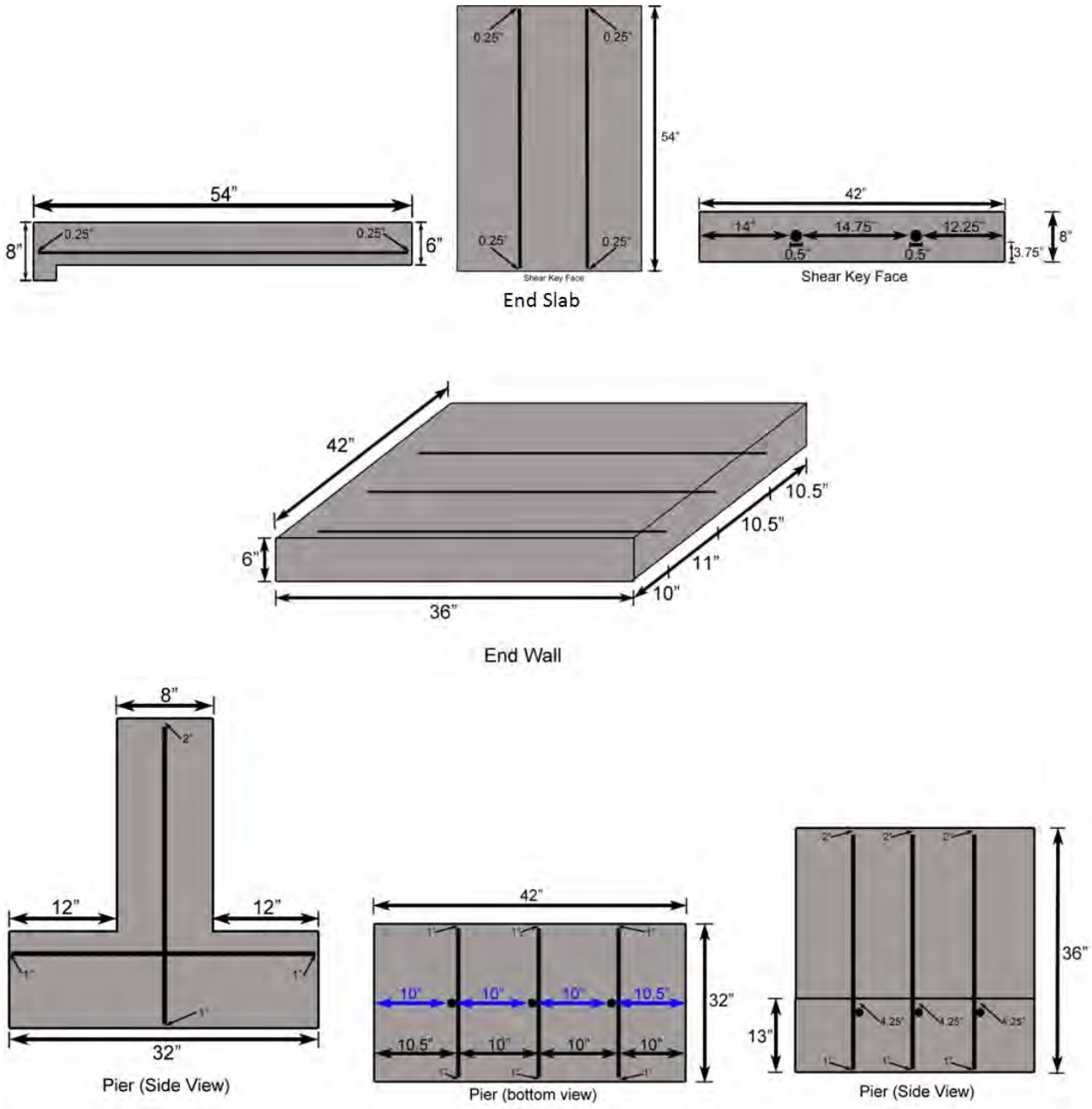


**Figure 18. Precast pieces showing dimensions and rebar placement.**

**Figure 19. Moving and wetting the scale model bridge forms.**

Three cubic yards of concrete was delivered by B&B Concrete. The mix was especially selected for this project: it is a derivative of a grouting mix used to fill concrete masonry blocks at the local high school. The aggregate to fines ratio was adjusted to 60% pea gravel to 40% fines. A superplasticizer was also added to mix with the final amounts as provided in Table 1.

**Table 1. Concrete mix provided by B&B Concrete.**

| Description | Amount |
|---|---|
| Pea Gravel | 4360 lb |
| Fly Ash | 385 lb |
| WRDA 35 | 87 oz |
| Sand | 4580 lb |
| Water | 47 gal |
| MIRA 110 | 198 oz |
| Cement | 1565 lb |
| Daravair | 12 oz |

All of the forms were filled in one pour from the same truck via chute over the course of 30 minutes. Several student and faculty volunteers were on hand to assist in the pouring process. The volunteers were equipped with hammers in order to strike the forms, effectively vibrating the concrete and removing any trapped air. Two by fours were also provided in order to spread the concrete evenly throughout the form while striking off any excess (Figure 20). After pouring most of the forms, the mix appeared to be running out. The decision was made to abandon the effort to pour a second identical center slab: the second center slab (or backup slab) retained enough concrete for a thinner center slab, so it was kept for use as a possible damage scenario during the later testing phase.

**Figure 20. Hammers used for vibrating forms and volunteers striking off excess concrete.**

Two 6x12 inch cylinders were also cast during the pour for compressive strength and Young's modulus testing. Sampling of the concrete was conducted in accordance with ASTM C 172 *Standard Practice for Sampling Freshly Mixed Concrete*. As shown in Figure 21, a slump test was also conducted in accordance with ASTM C 143 *Standard Test Method for Slump of Hydraulic-Cement Concrete*. The slump test yielded a slump of about 9.25 inches. According to the standard, a slump greater than about nine inches may not be adequately cohesive for the test to have significance. This slump does, however, indicate that the samples cast in the cylinders can be rodded since the slump was over one-inch. The concrete was sampled from the middle of the load and scooped into the cylinders. The concrete was then consolidated with a tamping rod in three separate layers with the sides of the cylinders being tapped with a mallet after each layer in order to close any insertion holes from the rod. The cylinders were then placed on a flat surface and allowed to cure for seven days before being removed and immersed in water until testing.

**Figure 21. Cylinder casting and slump test.**

The two cylinders were tested three days before the bridge move (32 days after pouring) in order to determine a representative strength "at time of move" for the concrete. The cylinder testing took place on May 7, 2013, in the Test Mark machine at the Ole Miss Jackson Avenue Center. The cylinders were removed from the water bath one day prior and dried, and they were then transported carefully to the site for the break. After being outfitted

with a compressometer to measure average strain during testing, the cylinders were loaded at a virtually static rate of 1000 pounds per second and were subjected to this increasing vertical axial stress until breakage (Figure 22).


**Figure 22. Testing of a cylinder and the resulting break.**

The results for both cylinders fractured at very high loads within 1.72% difference. The first cylinder broke at 7171 pounds per square inch (psi) while the second cylinder broke at 7049 psi. The two values were averaged to determine 7110 psi as the effective strength "at time of move" for the bridge pieces. Both cylinders broke in the same formation, which appeared to be between a cone and cone with shear split. The breakage occurred through the binder and did not break through any of the pea gravel aggregate in the cylinder samples.

Three days after the cylinder tests for a total of 35 days from pour, the scale model bridge pieces were moved from outside of the NCPA into the lab. Each piece was partially unformed before loading onto the chosen method of transportation. Bridge pieces were moved using a combination of pallet jacks for the slabs and a forklift for the t-shaped piers and end walls. Moving challenges included rotating the t-shaped piers and maneuvering the forklift into place in order to set the scale model bridge up correctly, both of which are illustrated in Figure 23. The piers were rotated using a combination of the forks on the forklift and towing straps while the tight maneuvering was overcome thanks to the expertise of the forklift driver.


**Figure 23. Challenges of moving one of the t-shaped piers.**

After five hours of moving pieces of the scale model bridge, the pieces were finally aligned and set into place giving the finished product. Overall, the scale model bridge was successfully formed and set into place yielding a superb finished product that can be easily tested and reconfigured for different damage scenarios. The baseline case, sketched in Figure 24, consisted of the center slab in direct contact with the t-shaped piers directly on either side. This case should give the highest frequency response due to the fact that there is no damping from the rubber bearings as in the damaged cases.

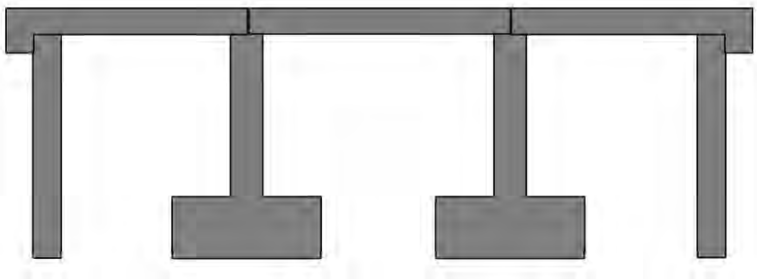

**Figure 24. Baseline case with concrete-on-concrete connections.**

The various damage cases were created by employing rubber bearings. A bottle jack on a pedestal was used to lift the center slab in order to insert and remove rubber bearings for different damage scenarios. The employed bearings varied from 1/16" to ½"-thick 40 and 70 shore durometer Buna-N rubber strips. Both asymmetric and symmetric configurations were tested. Note that a damaged support will have less stiffness due to component wear and more damping due to internal friction. Similar effects are realized for damage to substructural elements, such as pier columns, piles, and soil. The rubber bearings provide these effects for the bridge vibrations and thus produce a "damaged" scenario.

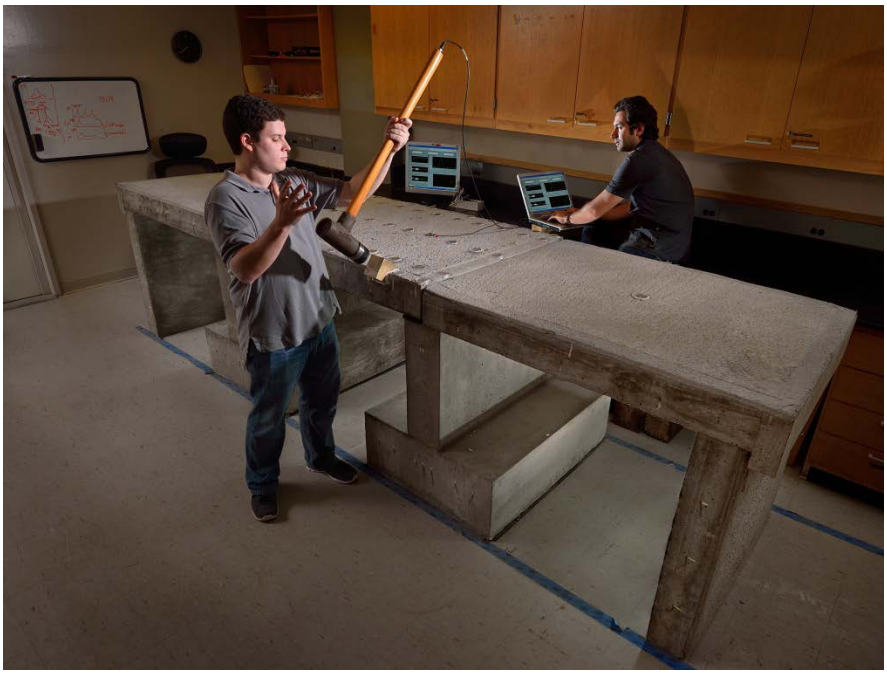

**Figure 25. Impact hammer testing with Steven Worley and labmate Farhad Sedaghati.**

Weighing approximately 1270 pounds, the 60”x42”x6” center slab is the target of the vibration testing. Shown in Figure 25, a twelve-pound PCB sledge hammer impacts the wood block on the bridge, inducing multi-dimensional vibrations. A Dytran tri-axial accelerometer on a level epoxy pad measures these nearly imperceptible motions, and this is repeated for 57 spatially diverse locations. These measurements take about 3 hours to perform and must be repeated for each damage case. A National Instruments CompactDAQ records the signals via NI LabVIEW, and the comma-separated text files are loaded into the MATLAB structural health algorithm for post-processing. Fast Fourier transforms are calculated, and modal peaks are identified for every damage case as well as the baseline. Note that natural frequency identification and mode correlation can be quite subjective: mode shape plots assist in these tasks, but time must be expended to analyze each potential resonance. Also, severe damage prevents modal coordination because the frequency response has experienced major shifts. This caused the damaged cases to be altered by using thinner rubber to represent joint damage. The origin and the associated 57 measurement locations are provided in Figure 26: note that two measurements are each approach slab, which proved very helpful in separating dissimilar modes. The other 55 measurements provide a grid that will allow for mode visualization in all three directions.

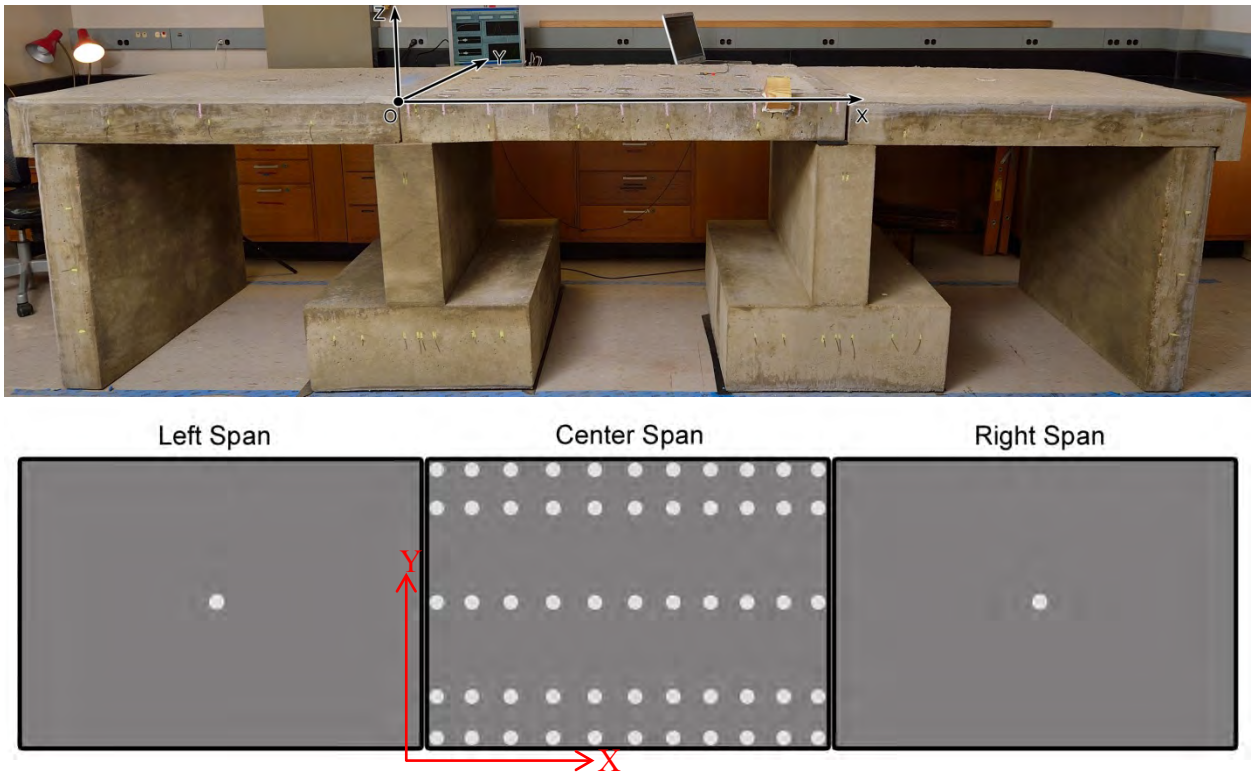


**Figure 26. Scale bridge orientation showing 57 captured data points.**

## 3. Experiment 3: Full Scale Bridge Test

The first step was to design an LDV measurement setup for the in-service bridge test. The NCPA staff developed a setup for fine angular adjustments of the LDV beam. It allows for accurate pointing of the LDV beam onto a selected location on the bridge for both on the top and under the bridge measurements.

Experimental investigation of the amplitude of the LDV signal was completed for different types of retroreflectors located at a distance from 10 feet to 110 feet. It was found that a plastic prism corner cube array provides the highest signal and can be used in the bridge tests at a distance of up to 110 feet.

Consulting all project parties, a field test plan for the on-campus Eastgate bridge was generated by the PI. The skew of the bridge was especially challenging to set an instrumentation grid, but this serves as an important coupling mechanism among modes. The selected grid needed to indicate up to the third bending mode as well as including torsion.

While testing in one lane, traffic on the other three lanes provides excitation. The traffic control plan has limited lane closures to one at a time on deck, but the two-lane road underneath was shut down for safety. A detour was approved by the city, and all relevant personnel (including emergency) were alerted. With cooperation from the City of Oxford and the University's Physical Plant, field tests were conducted on the on-campus Eastgate Bridge during Intersession 2013 (Figure 27).

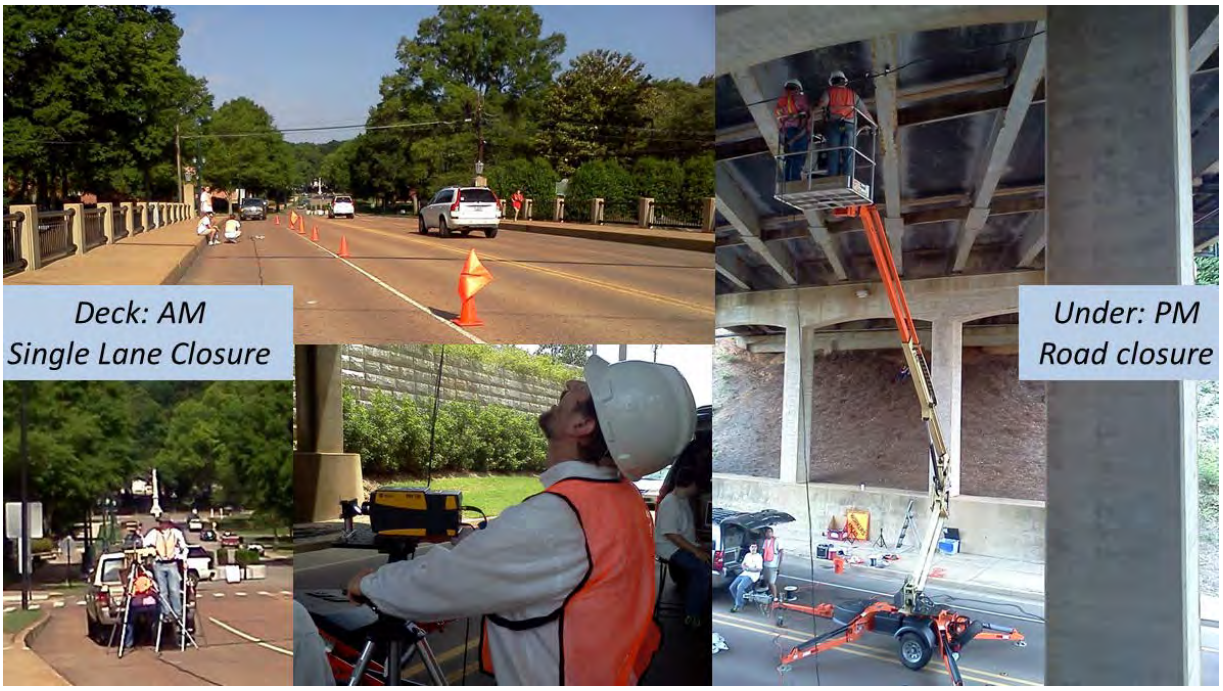


**Figure 27. Photo collage of the Eastgate Bridge testing.**

## Bridge Description

The Eastgate Bridge is located on University Avenue across from the Gertrude C. Ford Center and is a heavily used central connector by the Circle/Grove and the Ford Center. Figure 28 presents its current layout. According to drawings, the bridge was designed in 1939 by the now Mississippi Department of Transportation as a Federal State-Aid project. Its current owner and maintenance are in question, however.

Originally a highway overpass with a railroad underneath, the bridge itself is 34 feet tall with 32.6 feet clear underneath. It now supports four lanes of traffic as well as two pedestrian sidewalks and major campus utilities. The bridge has a 39 degree right forward skew, as shown in the next two sketches. Including several expansion joints, it consists of two 50 foot outer decks as well as a 60 foot middle deck, where most of the measurements for the testing were taken.

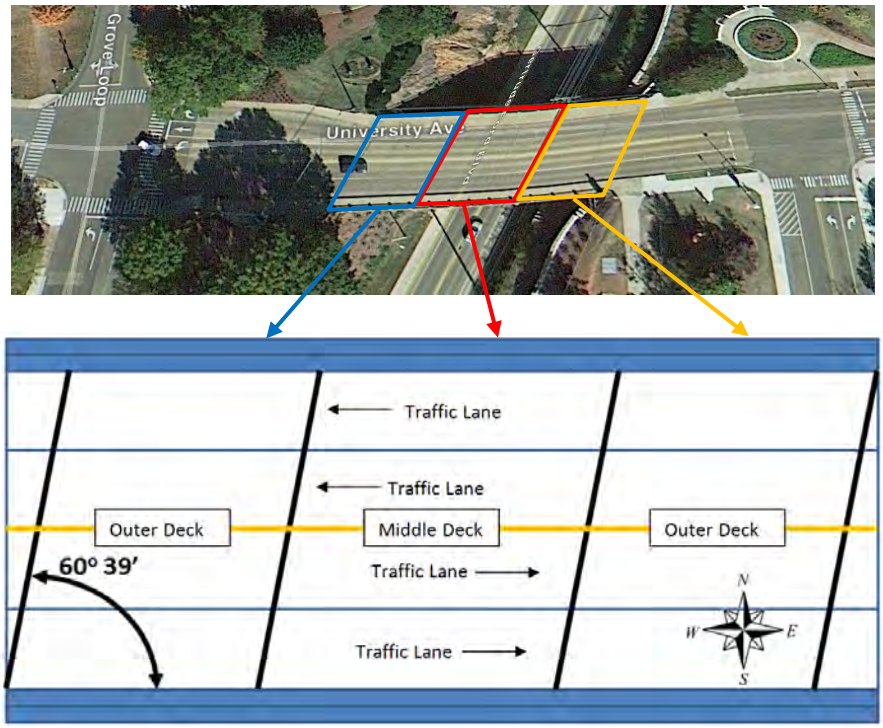


**Figure 28. Google Earth image (top) and illustration (bottom) of the Eastgate Bridge.**

The bridge consists of reinforced concrete decking supported by steel girders, which are then in turn supported by reinforced concrete multi-column piers. The girders are approximately 36 inches deep and 150 pounds per foot, which may susceptible to local deformations. A schematic cross-section of the bridge is shown in Figure 29.

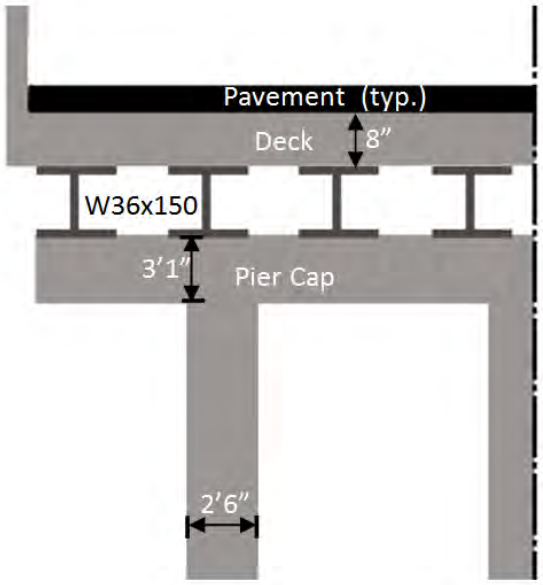


**Figure 29. A cross-section of the Ford Center Bridge (not to scale).**

## Bridge Testing

Testing on the visible bridge deck proceeded as planned. However, a serious problem was visually identified underneath the bridge. From the ground, all structural members and joints seemed reasonable for a 70-year-old bridge. Significant corrosion and abutment washes were detected, but the overall bridge appeared in good condition. The deficiency occurred in the steam plates or mending plates at nearly mid-span. The plates are trapping water that is from leaking expansion joints. The result is severe corrosion and broken clamps: these large, heavy plates may fall into traffic. This problem is illustrated in the next figure, which was provided to all authorities immediately following the inspection.

**Figure 30. 3 of 4 broken plate clamps (left) and an undisturbed setup on Beam 2 (right).**

Figure 31 shows the three employed measurement systems. A tri-axial accelerometer was formed by attaching three seismic sensors onto a machined and tapped aluminum cube, and this was used to capture accelerations on the deck of the bridge. A laser Doppler

vibrometer (LDV) was also used on both the top and bottom of the bridge to capture surface vibration. The aluminum cube also had attached a reflector on one of its sides which the LDV utilized when measuring velocities at an angle from bridge abutments. Magnetic sensors were used for underside measurements of the full-scale bridge. Magnetic bases were attached to two seismic accelerometers, and a prism corner cube array was glued to a magnetic base.

**Figure 31. Tri-axial accelerometer (left), laser Doppler vibrometer (middle), and magnetic accelerometers and corner cube reflector array (right).**

Data was gathered by a National Instruments (NI) CompactDAQ-9172 data acquisition system (DAQ) and a laptop with the NI LabView program. The instruments in Figure 31 were wired to the DAQ using long shielded BNC cables. The DAQ was attached to the laptop via USB where the data recording could be triggered through a custom LabView interface designed specifically for the Ford Center Bridge setup. A sample rate of 2000 samples per second and a sample length of 30 seconds were selected for use in the test; with publication assistance, similar tests were surveyed and preliminary frequency expectations were used for guidance. Files were saved from each run of the program as comma separated value files for later post-processing.

One problem in all signals with ambient excitation is high frequency noise pollution. This higher frequency noise can cause problems when identifying frequency peaks. Two potential solutions are possible: data filtering and/or data cleansing. Data filtering is easily implemented via built-in MATLAB functions. After reading filter literature and testing different filters on previous data, it was decided that the Butterworth low-pass filter usually yield the best results for low frequency ranges of interest. The Ford Center Bridge data with an applied Butterworth low-pass filter, however, produced no meaningful result. Even with a relatively low threshold, the time history magnitude was only slightly reduced, and the frequency response functions appeared identical. Thus, an alternate method was required.

Another solution to high frequency noise is data cleansing via cropping. The data portions with no apparent excitation and very small magnitude are cropped out of the time history, preserving data portions where larger excitation sources can be seen. When viewing the frequency response of the cropped data, the signal appears cleaner with reduced high frequency noise. Cropping a certain event can positively affect the data and make it easier to

determine modal information by eliminating much of the higher frequency noise. However, cropping does not always improve the signal. Excessive cropping can result in the loss of information leading to a poor quality response function. Cropping has its usefulness and even excessive cropping may prove beneficial for certain noisy, difficult peaks; conscientious inspection of the original signal is always important. Note that longer sample times may also be required to ensure that the cropped time history generates enough frequency resolution for accurate peak identification.

One final consideration is environmental condition, and Mississippi in May can offer extreme temperature variation. The surface temperature of the bridge deck was measured every 15 minutes during testing. Measurements were taken using an infrared thermometer pointed at the roadway from a distance of approximately 4 feet. The temperature variance is shown in Figure 27 along with a linear fit trend line. From the start of testing at 8:30am until the conclusion of deck testing at 11:45am, there was a temperature difference of 29.5°F. Ferrar (*19*) observed that New Mexico temperatures caused a 24% variation in natural frequencies, which can falsely indicate damage. For the testing beneath the bridge, the temperature remained fairly constant at near 92°F.

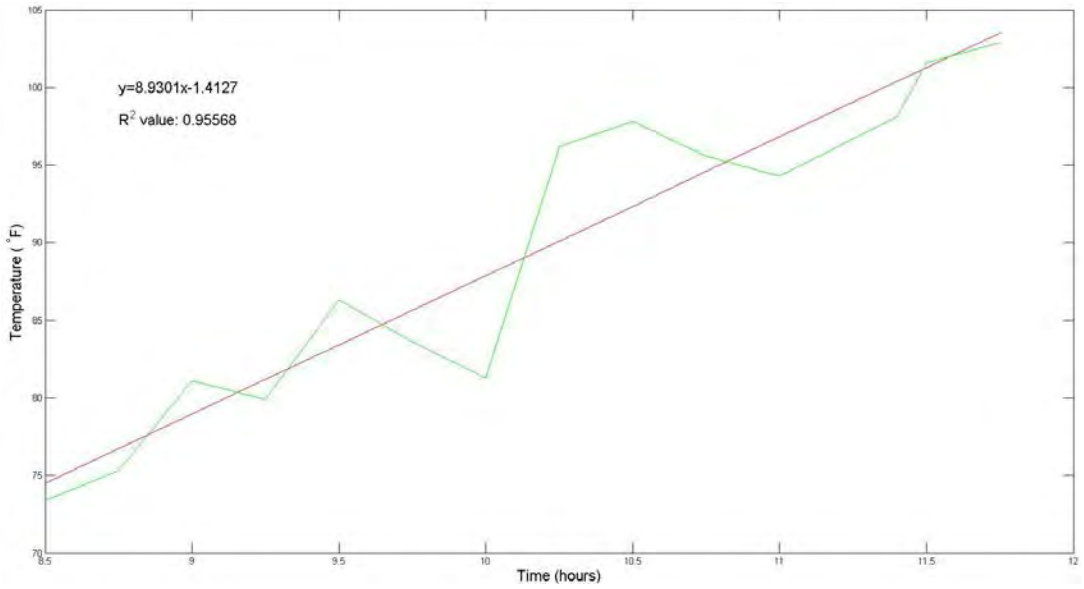


**Figure 32. Temperature variance on bridge deck with time.**

Measurements were scheduled to be taken at specific points on the bridge deck as well as on the girders underneath the deck. Testing commenced on the top of the bridge with the measuring and marking of instrument locations. The bridge deck had a total of 36 measurements scheduled: 28 on the center deck, 4 on the outer decks, and 4 on the abutments. Figure 33 illustrates the relative instrument locations for the top of the bridge. Note that one lane of traffic was closed each time measurements had to be taken on one side of the bridge. After one side was complete, the lane was reopened, and the other side was then closed to take the final side's measurements.

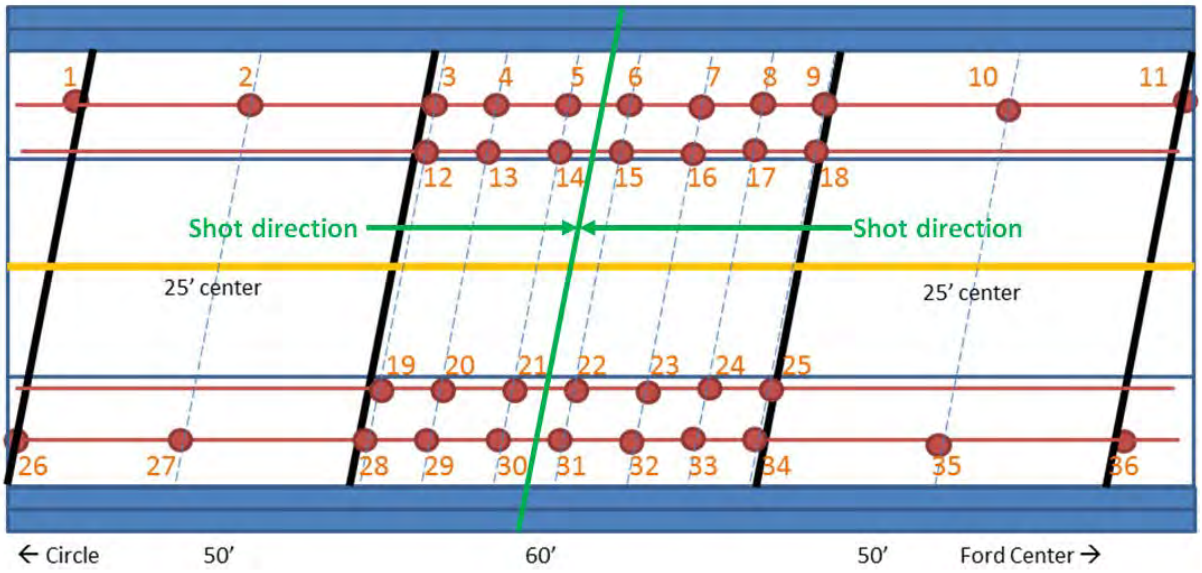


**Figure 33. An illustration of target measurement locations.**

The instrumentation schematic for the bridge deck is shown in Figure 34. Measurements in the grid of selected points were taken using the constructed tri-axial accelerometer (1.094 mV/g) and the LDV (PDV 100, Polytec, Inc.). The LDV was mounted on a tripod on an abutment, and the LDV beam was pointed onto a reflector attached to the accelerometer cube. The accelerometer and LDV signals were digitized using an A/D converter via LabVIEW and saved into a computer memory.

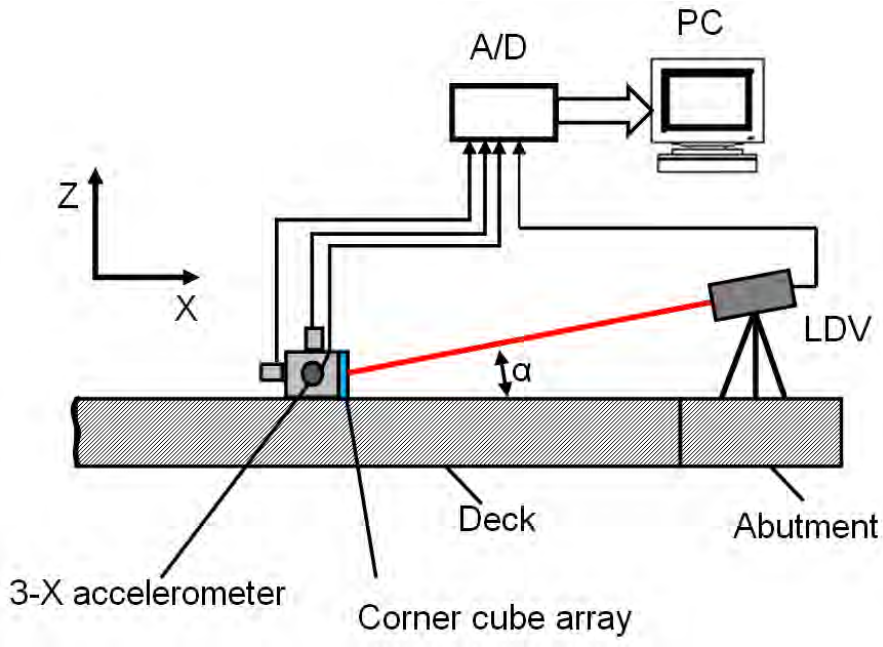


**Figure 34. Schematic of the vibration measurements on the bridge deck.**

After gathering data on the bridge deck, the equipment was moved to underneath the bridge. Unlike prior measurements, those underneath the center span used two single-axis accelerometers attached to the steel girders by magnets. The LDV methodology for taking measurements on the bottom of the bridge was also different. Instead of shooting at an angle, the LDV took only vertical shots from directly under the girder. The twenty points shown in Figure 35 were scheduled for testing.

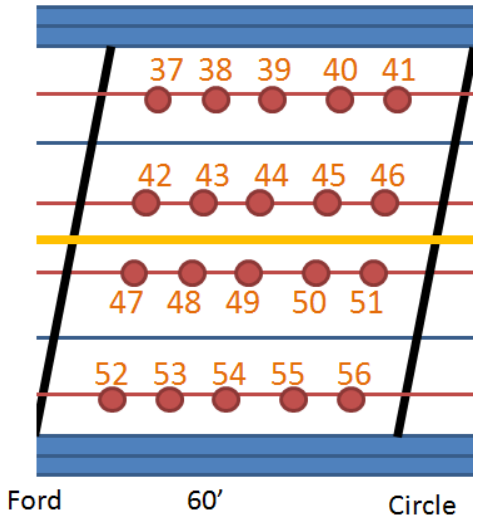


**Figure 35. An illustration demonstrating measurement locations under the center slab.**

The roadway under the bridge was closed for the entirety of the bottom testing. The girders underneath the center deck were reached with the assistance of a rented boom lift, and safety precautions were taken. Four of the planned points were not tested – points 41, 46, 51, and 52: these end points proved to be awkward for the boom lift and then deemed non-essential.

The instrumentation schematic for underneath the bridge is shown in Figure 36. Girder vibration underneath the center deck of the bridge was measured in the array of sixteen selected points, approximately 10 feet apart. The LDV with tripod was standing on the ground below the bridge and shooting in the vertical direction at a corner cube array reflector (Figure 36). The corner cube array increases the amount of reflected light, improving the efficiency and accuracy of LDV. The distance from the LDV to the girder surface approximately 28 feet (8.5 meters) of the 32.6 foot clear distance underneath. Two seismic accelerometers (10 mV/g) also measured sway (Y-direction) and bending (Z-direction) girder vibrations. The accelerometer and LDV signals were digitized using an A/D converter via LabVIEW and saved into a computer memory. At two girder points, the vibration was additionally measured using an LDV focused onto the unconditioned girder surface. These measurements were completed in order to verify the ability of LDV to measure the bridge vibration without using retroreflectors.

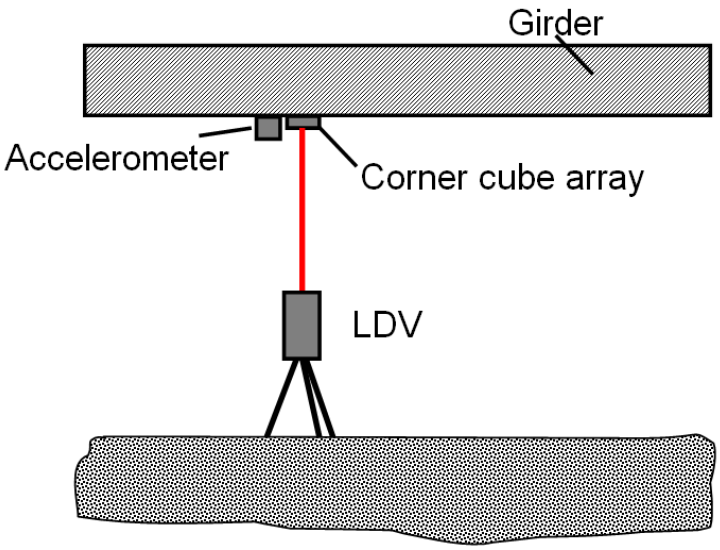


**Figure 36. Schematic of vibration measurement underneath the bridge.**

## 4. Structural Health Monitoring (SHM) Algorithm Development

Dr. Ervin and her team completed the development of an integrated structural health program. The flowchart is provided in Figure 37. There are four major modules: 1) input, 2) modal analysis, 3) health algorithms, and 4) output. The input is dominated by numerous data types and formats that can be provided for spatially diverse structures. Time history input is any comma-separated text file. Furthermore, the degrees of freedom and their locations must be recorded universally. Modal decomposition is a simple concept but one that is difficult to automate: to have full control of the algorithms, the team developed their own code. The team built one integrated program that employs several health algorithms. The user then correlates two modes upon which numerous structural health algorithms are applied. Visual output was completed for user ease: color-coded output is displayed to the screen, and these plots were provided throughout this report.

The next step was beta testing of the program. First, generation of faux ideal data for a simple damaged cantilever was successfully processed. Next, experimentally obtained data from previous testing in the Multi Function Dynamics Laboratory was processed through the new program. After some debugging, the results were consistent with those obtained by expensive commercial software, StarModal.

On December 5, 2012, supplementary testing for comprehensive debugging was performed on the truss bridge in Figure 38. This bridge was constructed by the UM student chapter of the American Society of Civil Engineers (ASCE). The bridge specifications were set by the 2013 competition, but senior students designed the truss. The bridge has an overall cantilever design and has bolted joints with welded connectors. No artificial manipulation of the bridge was conducted: that is, the "as-is" or "in situ" condition is used as the baseline for damage detection. Members of the bridge were sequentially removed to represent complete component loss. Multiple locations were altered so that damage of each joint can be evaluated through data analysis.

The National Center for Physical Acoustics allowed the loan of two batteries and a pure sine inverter. These were used to power a previously acquired National Instruments CompactDAQ data acquisition system that was wired to three accelerometers with magnetic mounts. A previously acquired laptop recorded X, Y, and Z sensor traces with an upgraded version of NI LabView: the base version had been previously acquired, and the upgrade was purchased by this grant at an excellent 75% discount. A 12-pound impact hammer was used to generate signals, but ambient data was also captured. Five seconds of data was recorded at 50,000 samples per second for each joint of the steel truss.

Employing 60 unique time history traces, mode shapes for the baseline case have been identified. The boundary conditions were shown to be dominant, as in the leg lifting of Figure 39. A unique interference occurred due to the rattling of the deck rail (red in Figure 38), so bandstop filtering was required. Harmonic identification was also challenging, but it was easier in the more damped concrete scale model bridge.

Overall, the structural health evaluation program developed by the Multi Function Dynamics Laboratory worked for all results presented herein. Of course, several bouts of debugging were required, but damage indices were able to be obtained via this software. The damage indication plots presented in other report sections were obtained via this developed software. The numerical damage thresholds will need further study for multiple structural

configurations, and a Ph.D. student has been hired to continue this work.

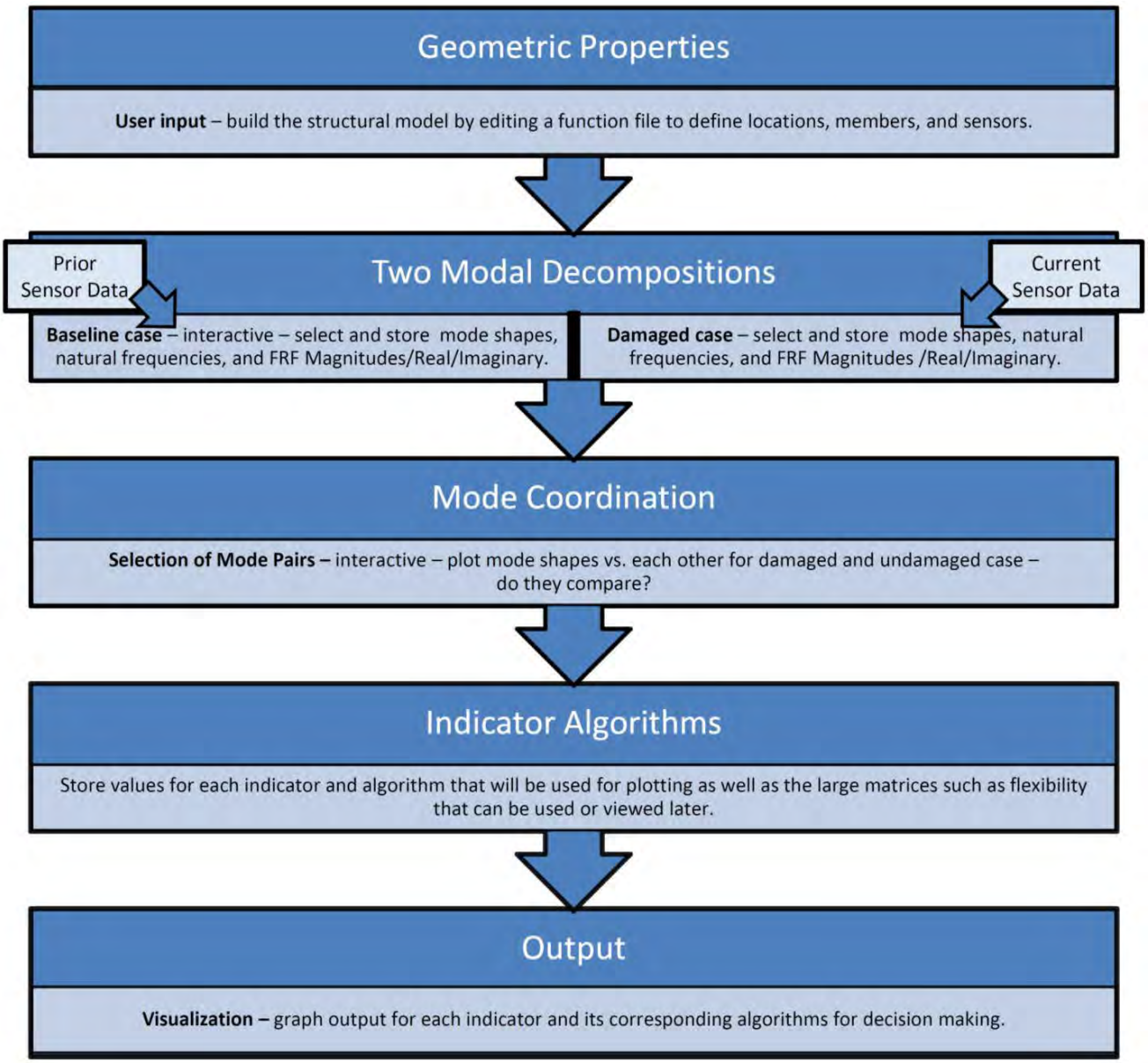


**Figure 37. Flowchart of comprehensive structural health program.**

**Figure 38. Testing in progress on the student-ASCE cantilever steel truss. Baseline shown.**

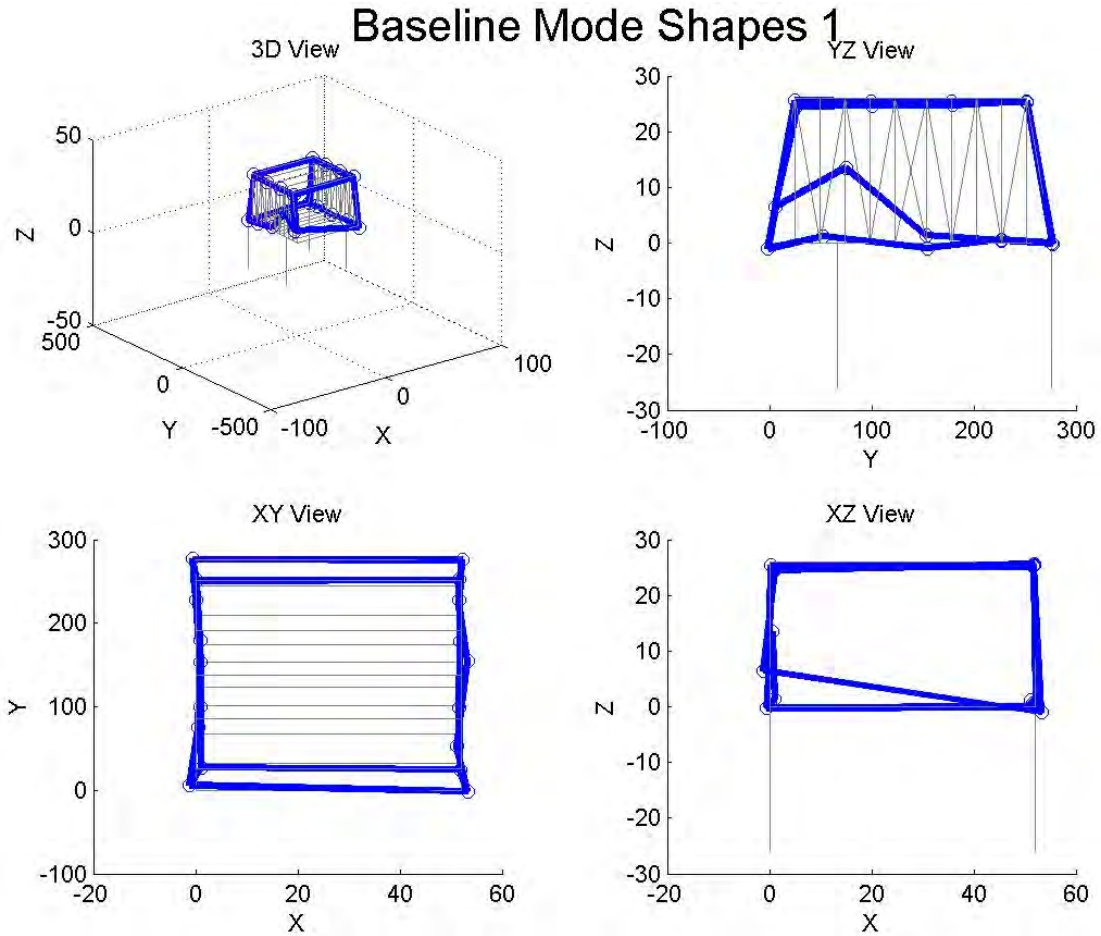


**Figure 39. Example of mode shape visualization. Baseline Mode 1 is the lifting of one ground support pier.**

## 5. Finite Element (FE) Modeling

Modeling with commercial software occurred throughout the project. The finite element activity has been performed to primarily support the model and operational bridge experiments.

### Scale Model Bridge

In the planning stage, preliminary models of a three-span simply supported reinforced concrete slab/pier bridge were developed. Various span lengths and other parameters were considered to establish a range of expected modal frequencies that would meet the goals of the testing within the constraints of available laboratory space and the project budget. The FE model of the lab experiment was also used to help examine a feasible method to represent softening damage in bridge substructures using rubber bearings under the deck slabs. Details of preliminary models used in the planning phase are described in a thesis (*20*) prepared by a student, Kyle Bethay, who received partial support for his graduate studies from the project.

In the production stage, the finite element (FE) analysis of the scale model bridge specimen was performed using SAP2000 structural analysis software (*18*). Figure 41 shows a perspective view of the FE model, which is comprised of 597 joints, 446 shell elements, 80 frame elements, and 3054 degrees-of-freedom (DOF). The choice of shell elements was based upon the bridge's construction of entirely concrete slabs poured at the laboratory site. Thus, all components (deck slab, pier wall, and footing) were essentially defined by a middle surface area and a thickness, which was assumed constant for each component. Note that Figure 40 shows only the middle surface, but the element membrane and bending stiffness for each element incorporates its thickness.

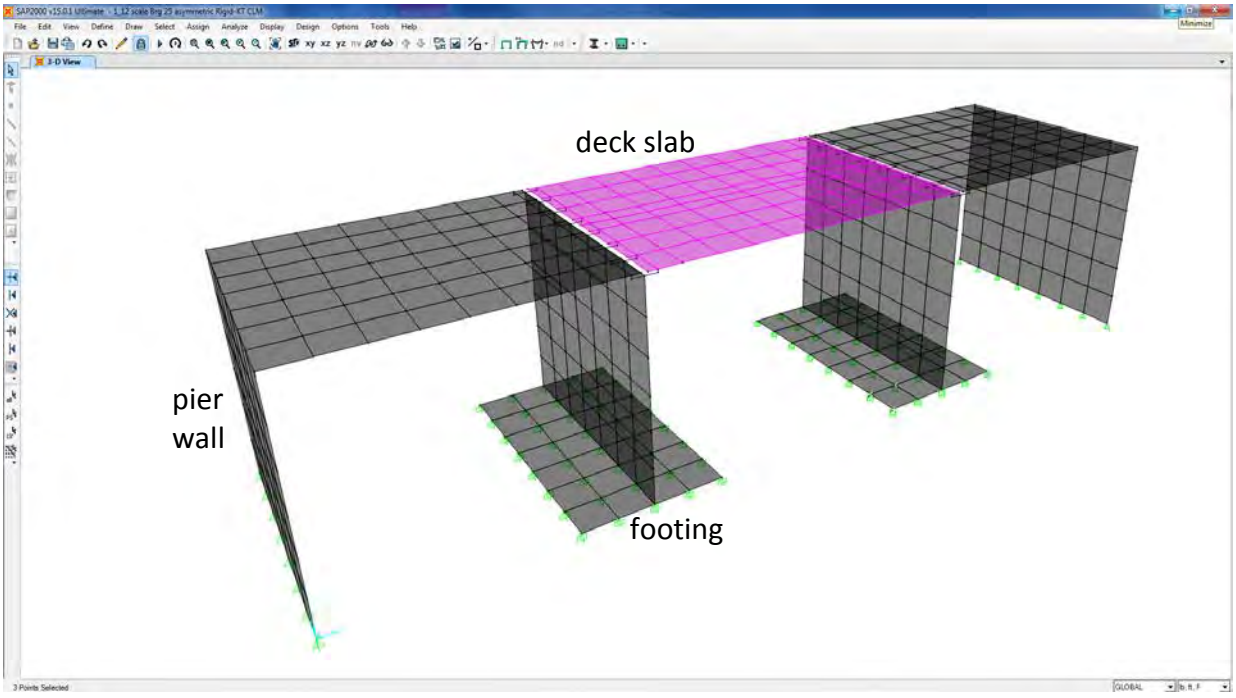


**Figure 40. SAP2000 model of reinforced concrete bridge specimen.**

The most challenging modeling aspect is the contact surface between components. The nature of the contact between concrete deck slab and concrete pier wall proves to be quite complex at low levels of vibration in the presence of gravity and friction. The interaction between pier wall and deck slab components is further complicated by the fact that the vertical and horizontal shell elements do not allow for an interfacial area or contact surface. Bearing pads were used to represent softening in the experiments; in order to capture the deformation in basic modes (axial, shear, and bending), frame elements were used to represent contact. Figure 41 shows a detail of an interfacial region.

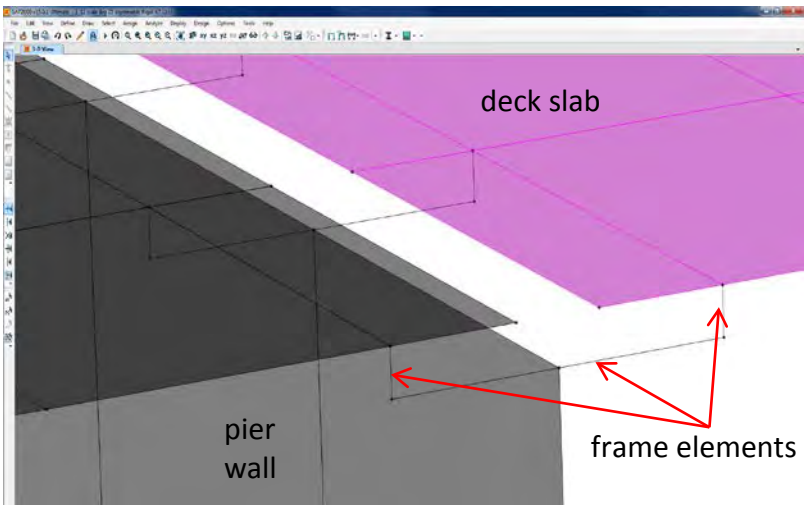


**Figure 41. Interaction detail for SAP2000 model of the scale bridge specimen.**

For the different components, the FE model inputs for the shell elements included height, width, and thickness as well as material mechanical properties, specifically, Young's modulus $E_c$ and Poisson's ratio $\nu$ for the poured concrete. The ACI 318 formula $E_c = 57000 \cdot \sqrt{f_c'}$ was used to estimate the Young's modulus for the concrete based on unconfined compression tests, which identified an unusually high strength $f_c'$ of 7000 pounds per square inch (*21*). The weight density of 150 pounds per cubic foot was assumed for standard weight concrete.

The shell element mesh was designed to generally maintain a six-inch square size. The mesh at the deck slab ends accommodated the frame element connection and the half-inch gap between adjacent deck slabs. Stiffness analysis of an isolated slab with this mesh design was performed under uniform static pressure and simple edge support conditions; this configuration was in good agreement with plate bending theory and thus was validated. Modal vibration analysis was also performed, and the fundamental bending frequency was within one percent of elementary beam theory.

The FE model input for the frame elements included equivalent mechanical properties that are selected to represent bearing stiffness *k*. Equivalent properties for the vertical frame elements were determined based on direct lab measurements, online vendor specifications, and elementary mechanics theory. The vertical frame elements were selected to have a fixed height *L* of 1 inch, a fixed section area *A* of 4 square inches, and an effective Young's modulus *E* in order to obtain the desired equivalent vertical stiffness $= \frac{E \cdot A}{L}$. For shear

deformation, the software used a shear modulus of $\frac{E}{2(1+\nu)}$. To avoid complete freedom of rotation or hinge action, a small moment of inertia *I* was assigned to the frame members. This eliminates zero energy (zero frequency) modes of the deck slabs. The horizontal frame elements were assigned a fixed length *L* of 4 inches, the width of the bearing pad. The equivalent mechanical properties were selected to behave essentially as a rigid member: steel's $E = 29{,}000\ ksi, A = 1\ ft^2$, and $I = 1\ ft^4$. This behavior enables rotation at the top surface of the pier walls to be transmitted to the bearings and then to the deck slabs.

As the green symbols in Figure 40 indicate, the support conditions in the FE model consisted of both fixed and pin supports. All joints of the footings had all six translational/rotational DOF restrained, and all joints of the end pier walls had all three translational DOF restrained. Preliminary calculations of frictional restraint showed that the structure's self-weight is sufficient to hold all points in contact with the ground, essentially preventing translation. The large thickness of the footings prevents any bending in these elements, holding the mid-surface fixed against rotation. As a result, the footing's shell elements are completely restrained and provide only a visual representation.

## Full Scale Bridge

### Prior Study

The Eastgate Bridge has been modeled under a previous study with the focus on seismic vulnerability of select on-campus structures. A three-dimensional finite element model of this operational bridge including soil-structure interaction was available. Figure 42 shows an isometric view of the model (*22*,*23*). Emphasis for this model is placed on structural response characterization of the embankments and substructures. The superstructure is modeled using shell elements for the concrete deck slab and beam elements for the steel girders and transverse stiffeners. The finite element mesh consists of 2,226 nodes; 1,676 elements (8 spring elements, 546 bending elements, 376 plate elements, 504 continuum elements, and 242 infinite elements); and 8,100 DOF.

The prior model was analyzed using the ABAQUS general purpose software (*24*) and provided initial expectations for natural frequencies (Table 2) and characteristic mode shapes. The details of the prior model, however, were selected with extreme loading and nonlinear material response in mind. The specific concern was pier response to a catastrophic earthquake. The deck, in particular, in the vicinity of the pier supports was thus not given the level of detail in that model since overall load transfer to the pier columns under large ground motion was the primary concern.

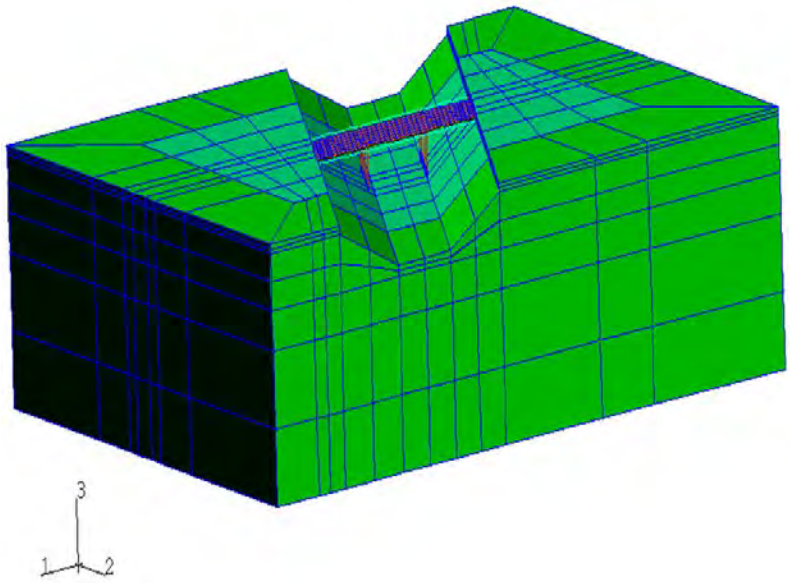


**Figure 42. ABAQUS soil-structure interaction model of the operational bridge.**

**Table 2. Characteristic modes for ABAQUS soil-structural interaction model of the operational bridge.**

| Frequency (Hz) | Description |
|---|---|
| 2.75 | Center deck vertical translation accompanied by out-of-plane composite deck bending |
| 3.34 | Global deck longitudinal translation accompanied by out-of-plane pier column bending |
| 3.47 | Global deck transverse translation accompanied by in-plane pier column bending |

**Present Study**

In contrast, for the present study, the response is governed by ambient excitation under normal operating conditions. The low-level vibrations used to capture modal characteristics of the in-service bridge calls for emphasis on the deck superstructure. A new model was therefore created which more carefully considers a typical composite deck section. The large numbers of degrees-of-freedom required for the detailed modeling approach limited the scope of the model to a single deck span. The interaction between the spans associated with pier movement is not considered significant in this case where the simple supports and stiff piers essentially decouple the adjacent spans' dynamic responses.

The as-built structure in Figure 43 was physically investigated. The potential influence of superstructure support conditions on low-amplitude vibration characteristics was examined. Sensitivity of modal analysis and forced vibration response data to variations in the superstructure/substructure component characterization was explored.

**Figure 43**. **Photos of Eastgate bridge showing views of the substructure and abutments.**

The production FE model was created using a more current version of the ABAQUS software (*25*). Figure 46 shows an isometric view of the superstructure, which is modeled entirely using 3-D continuum elements. Sizes of the elements were selected to maintain an acceptable aspect ratio less than 1:20 with respect to the steel shapes that include thin sections (flanges and web). The choice of modeling approach led to a model almost six times as computationally intensive as that in the previous study, even though only one component subsystem is included. The resulting model is comprised of 11,869 nodes; 1,856 elements; and 35,607 DOF. Curiously, the advances in computing hardware from the time of the prior study enabled the current model to be analyzed on a Windows-based desktop workstation rather than a Cray supercomputer and a Silicon Graphics workstation.

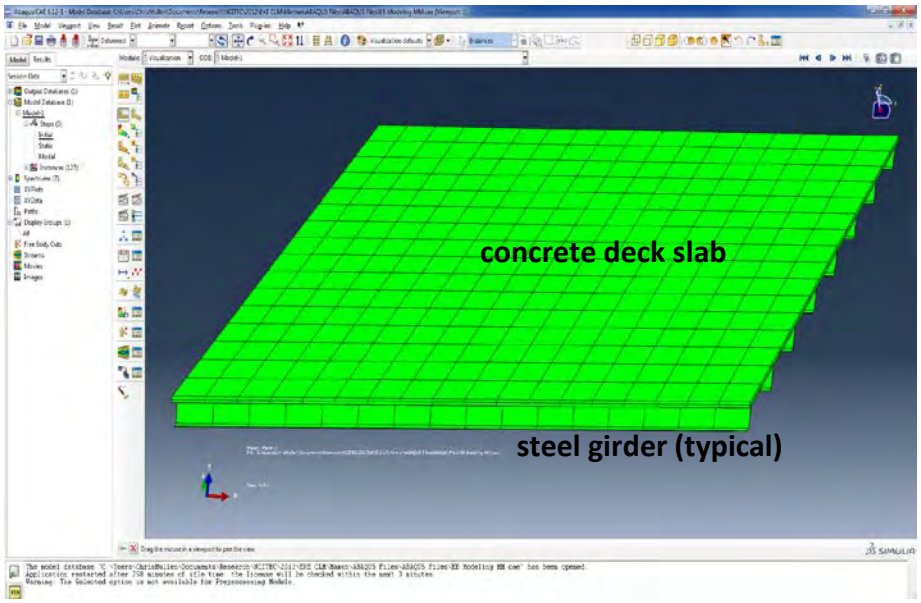


**Figure 44. ABAQUS model of the center span of the operational bridge.**

The model input for the solid elements included the mechanical properties for the poured concrete and rolled steel shapes. Designed by the former State Highway Department in Mississippi (now Mississippi Department of Transportation Bridge Division), specifications called for all concrete to be Class B. Consistent with current specifications for this class, the Young's modulus $E_c$ was estimated based on an assumed strength $f_c'$ of 3,100 pounds per square inch. The design drawings were used to establish the aforementioned deck slab dimensions, which include a 60-foot span and 60-degree skew. Section dimensions for the rolled shapes were estimated from data available from AISC steel practice (*26*).

# DISCUSSION OF RESULTS

In this section, the results from primary activities will be discussed. Note that the structural health program results are presented throughout.

## Experiment 1: Non-Contact Rail Inspection

Figure 45 shows examples of vibration signals of the railway structure recorded with the accelerometer and the still LDV. Note that the units are different so the magnitudes do not correlate. However, each change of direction should correspond.

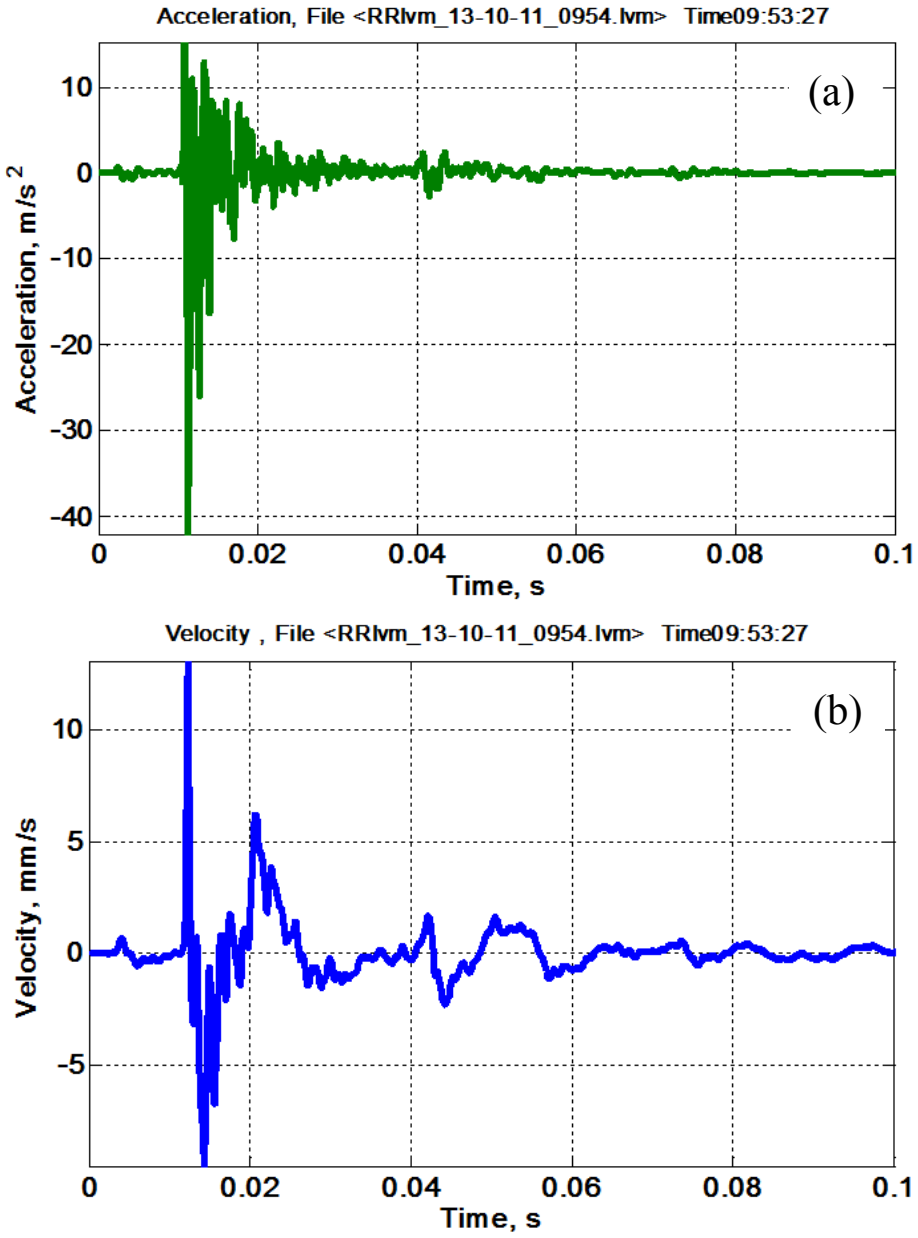


**Figure 45. Examples of the undamaged railway track response to impact excitation recorded with (a) an accelerometer and (b) a stationary LDV.**

Figure 46 shows examples of vibration signals of the railway structure recorded with the accelerometer and the moving LDV. When compared to the stationary measurements, the major effect of the LDV's transverse motion is the occurrence of narrow spikes in the LDV signal, as in Figure 46(b). These spikes result from Doppler signal dropouts and phase discontinuities of speckle field formed by diffusely reflected laser light. These short spikes increase LDV measurement noise which can mask small vibrations (*16,17*). The effect of these spikes is insignificant as shown by the measurements conducted in the current series of experiments.

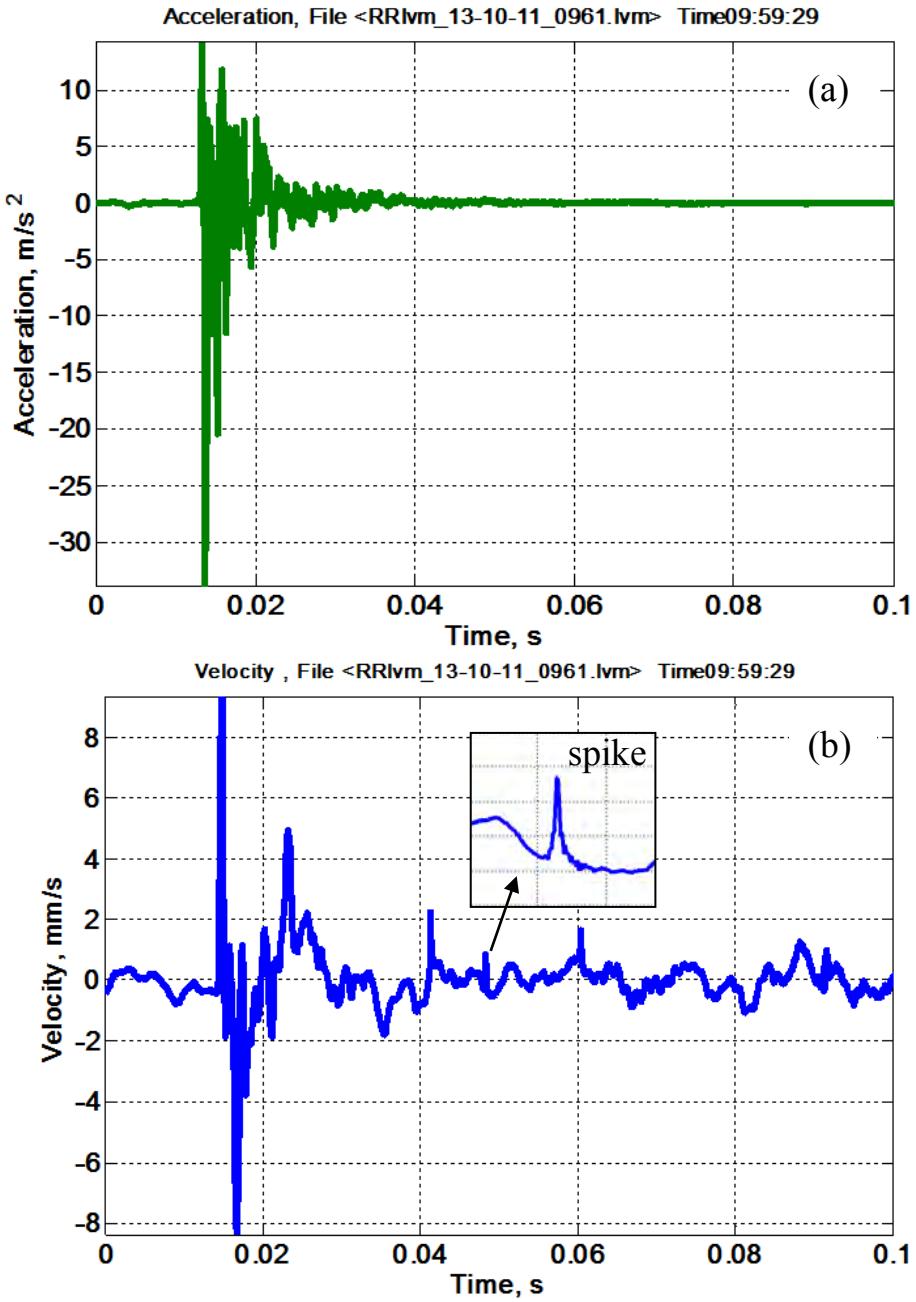


**Figure 46. Examples of the railway track response to impact excitation recorded with (a) an accelerometer and (b) a continuously moving LDV at 20 mm/s.**

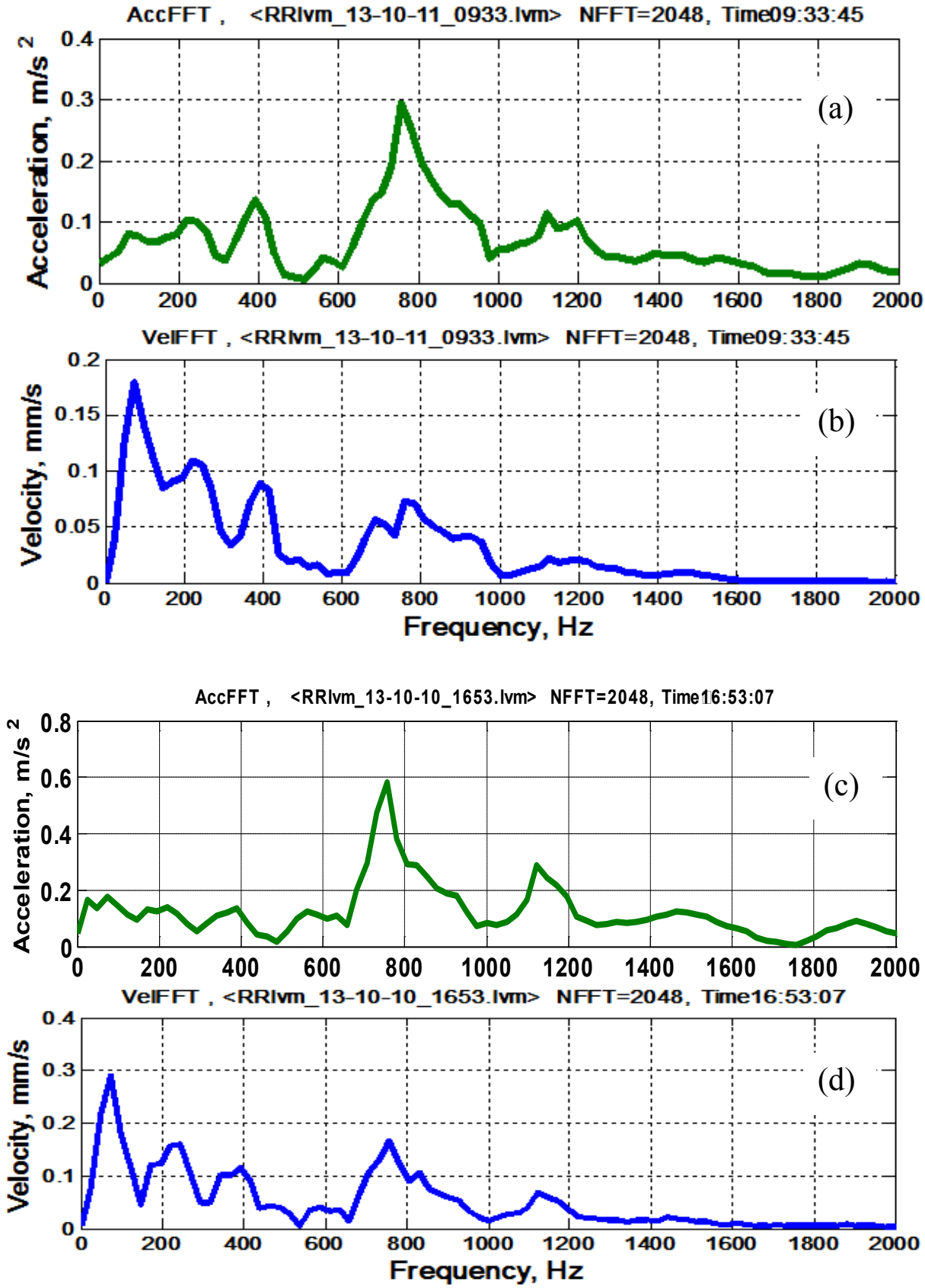


**Figure 47. Frequency spectra for the baseline rail. Run 1 with (a) accelerometer and (b) still LDV; Run 2 with (c) accelerometer and (d) moving LDV.**

Figure 47 illustrates the frequency spectra of the undamaged baseline railway track. Vibration spectra measured with the LDV in both still and moving modes are practically identical. They show resonant peaks at the same frequencies. Slight differences are due to natural variations in impact excitation, which was manually repeated and was not identical for each event. An example of variation in vibration spectra from one impact to another can be seen by comparing acceleration spectra in Figure 47(a) and (c). Since these plots usually contain the same frequency information, the extra accelerometer response will not be presented in future plots.

Figures 48 to 51 present frequency spectra of the railway track with different defects. Each has been measured with an accelerometer and the LDV in both still and moving modes. The significant differences in spectra between baseline and defective structures are marked by red circles.

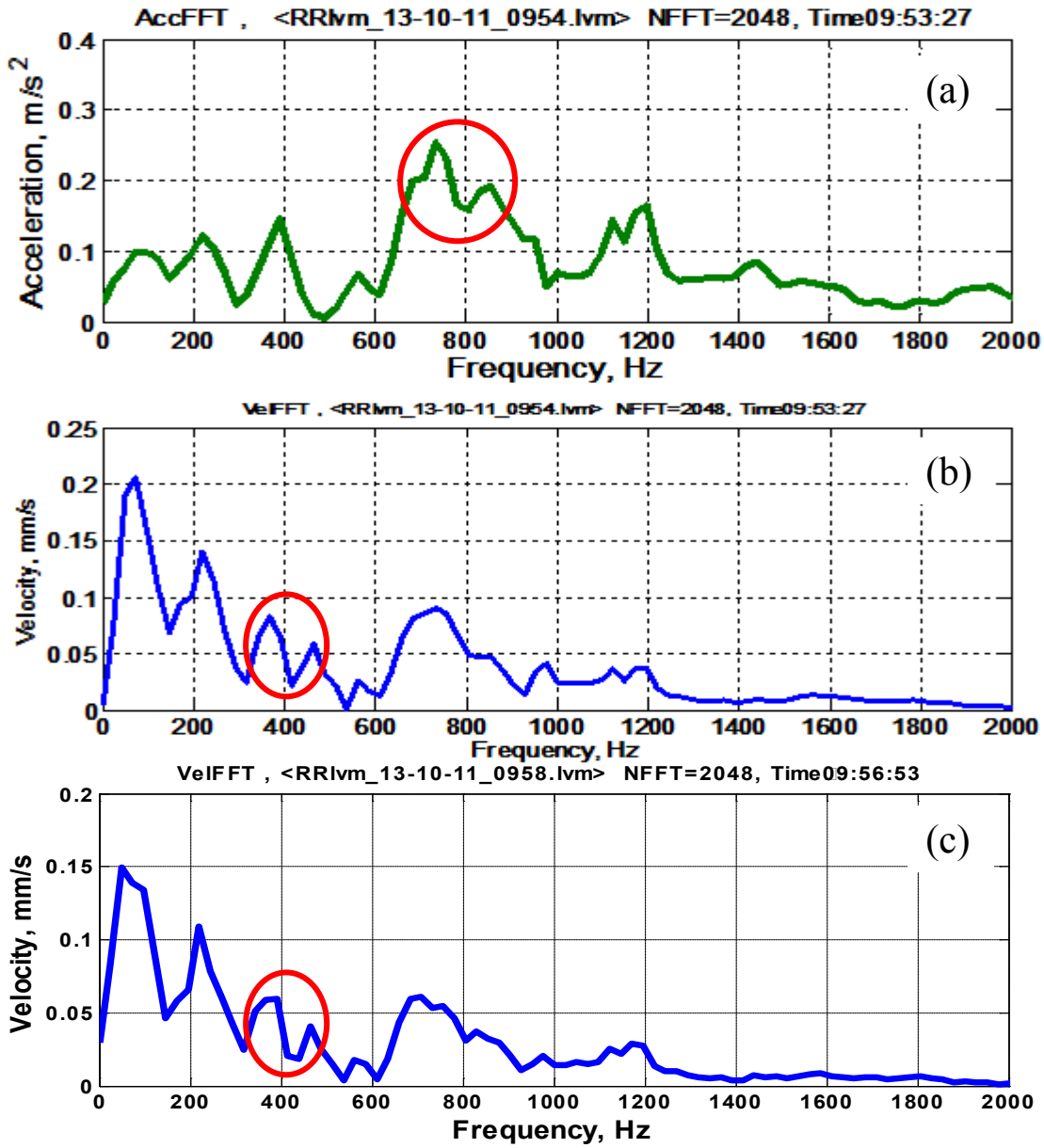


**Figure 48. Frequency spectra for the rail with one loose screw in center tie plate: (a) accelerometer, (b) still LDV, (c) moving LDV.**

Figure 48 shows frequency spectra of the railway track with the induced defect of one loose tie-plate screw. This case represents minimal damage, as just one of four screws is altered that attaches the tie plate to the tie. The e-clips holding the rail to the tie plate are unaffected. The circles indicate two major changes in the spectra due to this damage. First, the defect causes variation in the peak around 800 Hz in the acceleration spectrum. Second, the peak at 400 Hz splits in the both LDV vibration spectra.

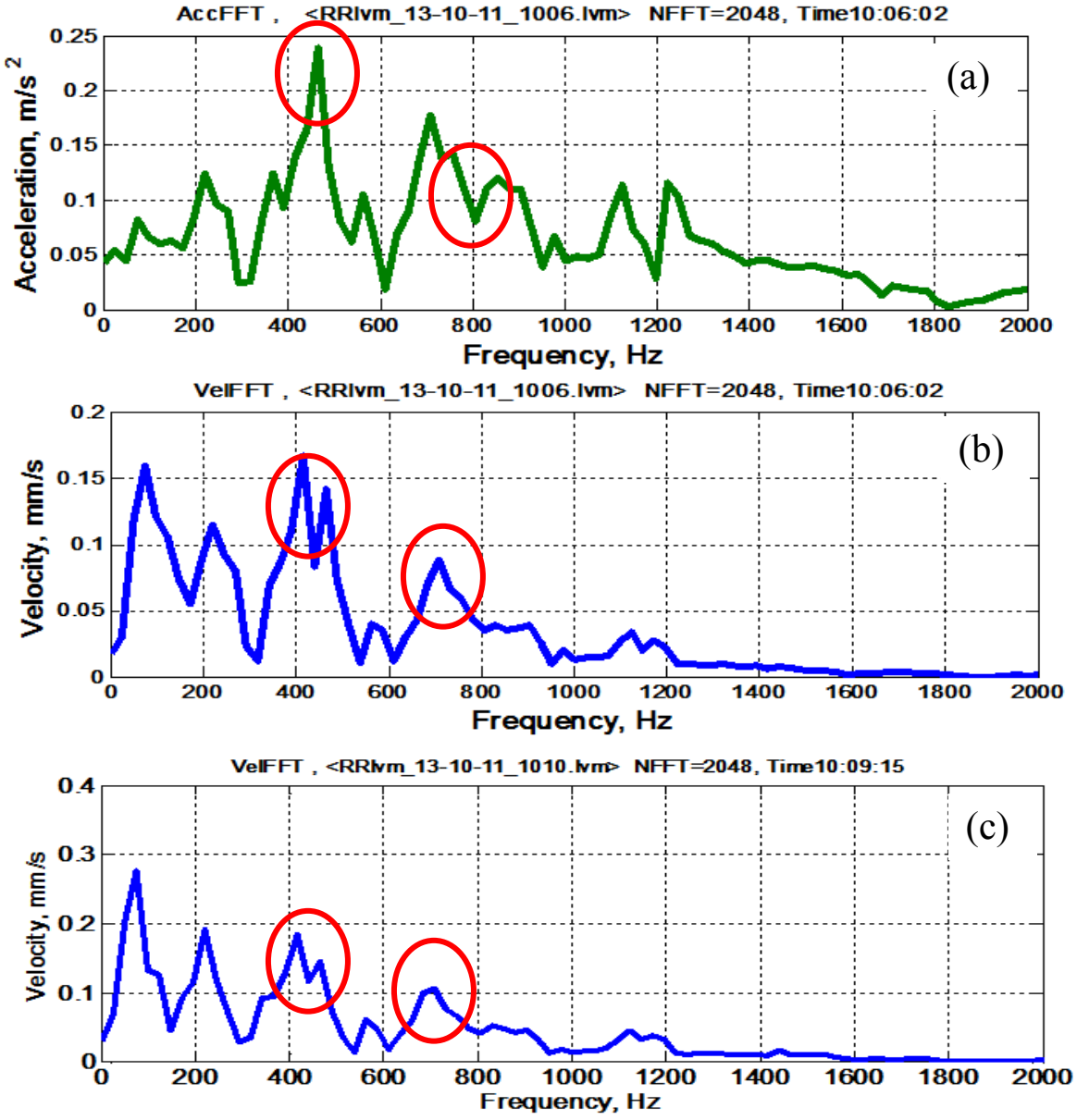


**Figure 49. Frequency spectra for the rail with two loose screws in center tie plate: (a) accelerometer, (b) still LDV, (c) moving LDV.**

Figure 49 shows frequency spectra of the railway track with the induced defect of two loose tie-plate screws. This represents an incremental increase in the damage state. As the circles show, this defect causes more significant changes in the vibration spectra. The peak around 800 Hz in the acceleration spectrum splits. Peaks around 400 Hz are shifted to higher frequencies for both acceleration and velocity spectra; they are also split into two peaks in both LDV vibration spectra.

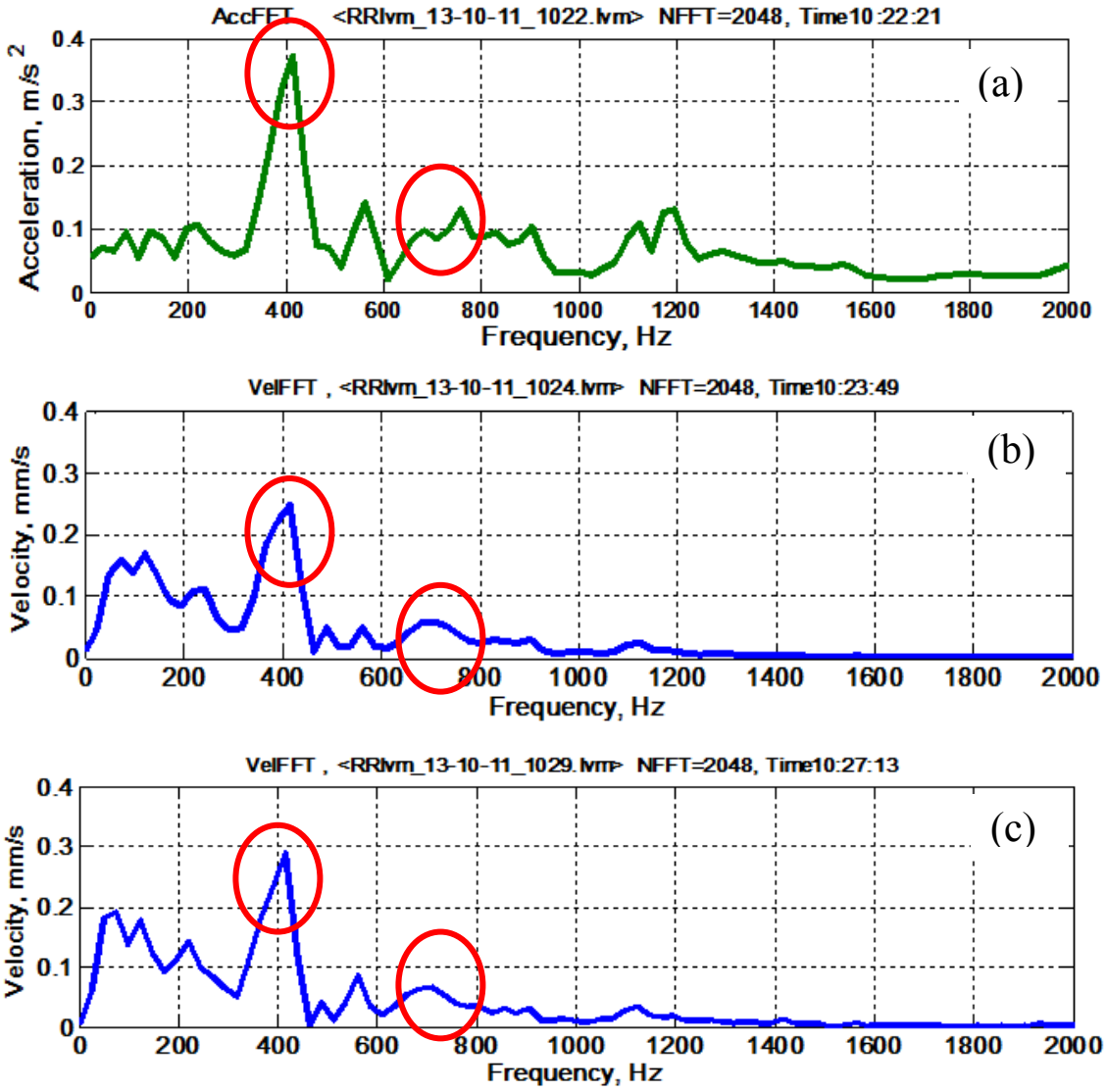


**Figure 50. Frequency spectra for the rail with four loose screws in center tie plate: (a) accelerometer, (b) still LDV, (c) moving LDV.**

Figure 50 shows frequency spectra of the railway track with the induced defect of four loose tie-plate screws. This represents the maximum release in the connection between the plate and the tie. As the circles show, this defect causes major changes in the LDV vibration spectra. There is a significant magnitude increase of the peak near 400 Hz. The area near 800 Hz also experiences lesser response.

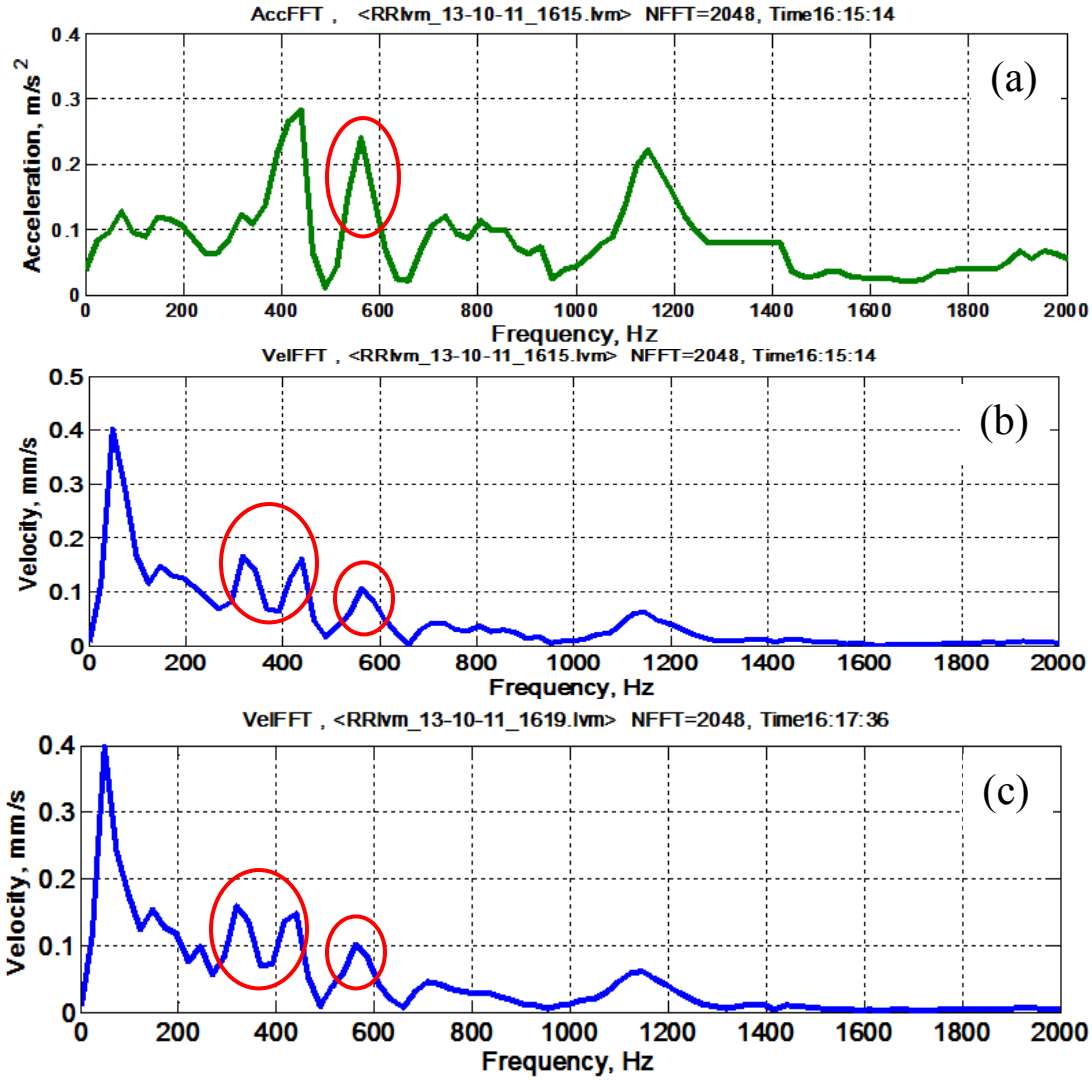


**Figure 51. Frequency spectra for the rail with cracked tie plate: (a) accelerometer, (b) still LDV, (c) moving LDV.**

Figure 51 shows frequency spectra of the railway track with the induced defect of a cracked tie plate. In addition to loose screws, the tie-plate was cut in half and inserted underneath the rail. As the circles show, the peak magnitude further increases near 400 Hz, and lesser response occurs near 800 Hz.

The conducted experiments **qualitatively** show that structural defects of a railway track can be detected by measuring the rail vibrations. Both the accelerometer and the LDV showed enough sensitivity to observe variable frequency content between the damaged cases: split and amplified modes were identifiable. The motion of the LDV did not noticeably increase the LDV noise, but the speed of LDV in the experiments was slow, just 20 mm/s. Additional research is required in order to assess the ability of detection of structural defects of a railway track using a LDV moving with higher speeds.

In order to **quantitatively** compare the data, the developed structural health program was applied. The selected damaged case was four loose screws from Figure 50, which represents the incremental damage of the same nature. The frequency range of structural interest is often 0 Hz to 250 Hz, and thus eight and nine modes were identified for the baseline and the damaged cases, respectively. Modes were coordinated by inspection of mode shape similarities: this is a subjective and qualitative process.

Natural frequencies should decrease with damage, and they generally do here in Figure 52. There was no significant change to Mode 3's frequency, which requires an examination of the associated mode shapes. These are provided in Table 3: note that qualitative comparisons are difficult. This visualization tool is helpful to observe the bending modes of the rail, and Coordinated Mode 3 corresponds to the center tie deflecting downwards (the negative z-direction). In fact, one damage index (MAC) showed that Mode 3 was 97% damaged. These results mean that the four loose screws decoupled the tie from the rail and allowed it to vertically "rattle." Coordinated Mode 1 also showed 92% damage, which means that torsion of the center tie also occurs.

Six damage indication algorithms were applied, and the results are illustrated in Figure 53. The algorithms are discussed in detail in the next section of this report. While variation occurs, most indicators show significant damage at the center tie and most commonly on the right side of the tie. This again provides confidence that the LDV is sensitive enough to use for damage detection.

Note that the color-coded thresholds are arbitrary and will require more research to set for any given setup.

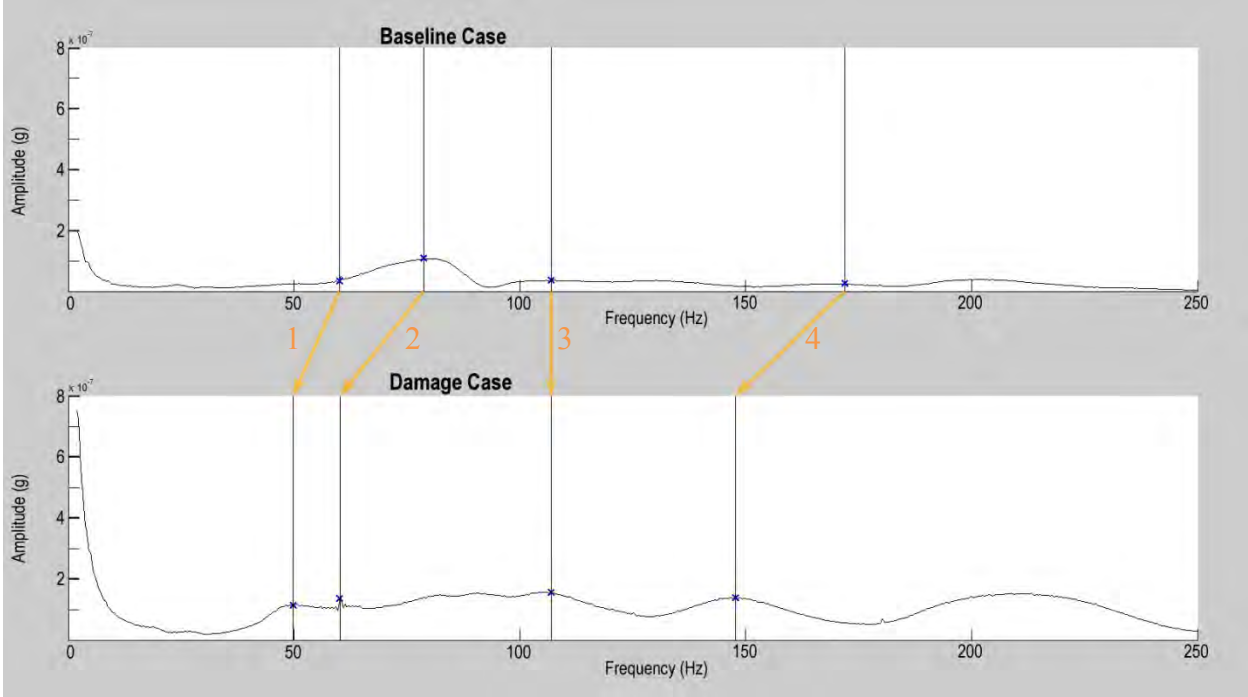


**Figure 52. Natural frequencies of coordinated rail modes shift downward due to damage.**

**Table 3. Coordinated rail mode shape plots.**

Coordinated Mode 1

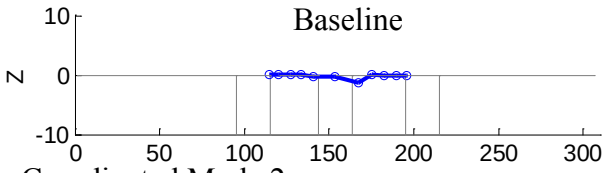


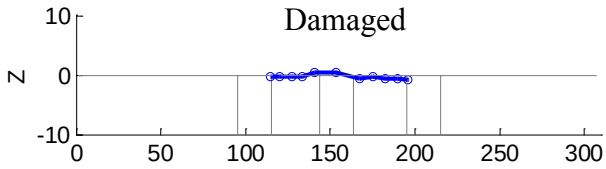


Coordinated Mode 2

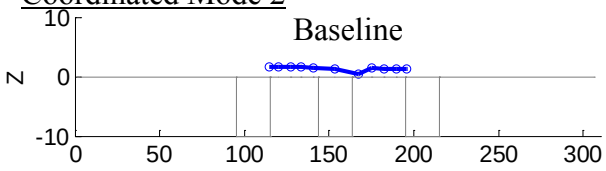


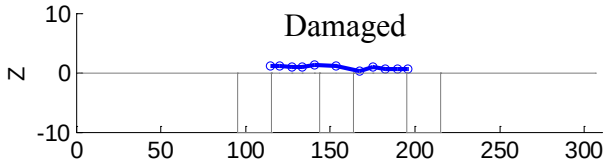


Coordinated Mode 3

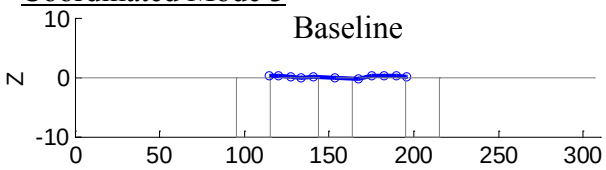


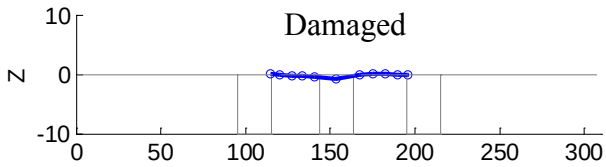


Coordinated Mode 4

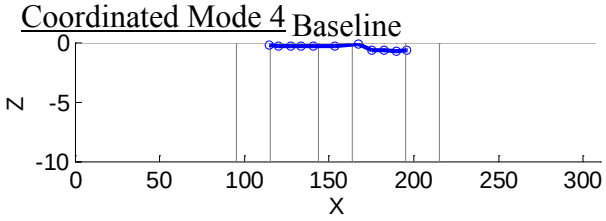


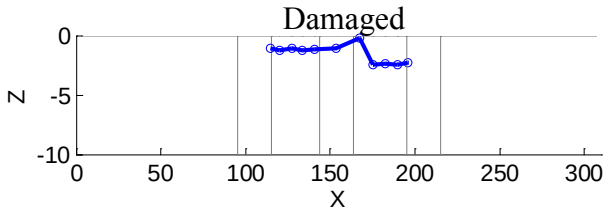

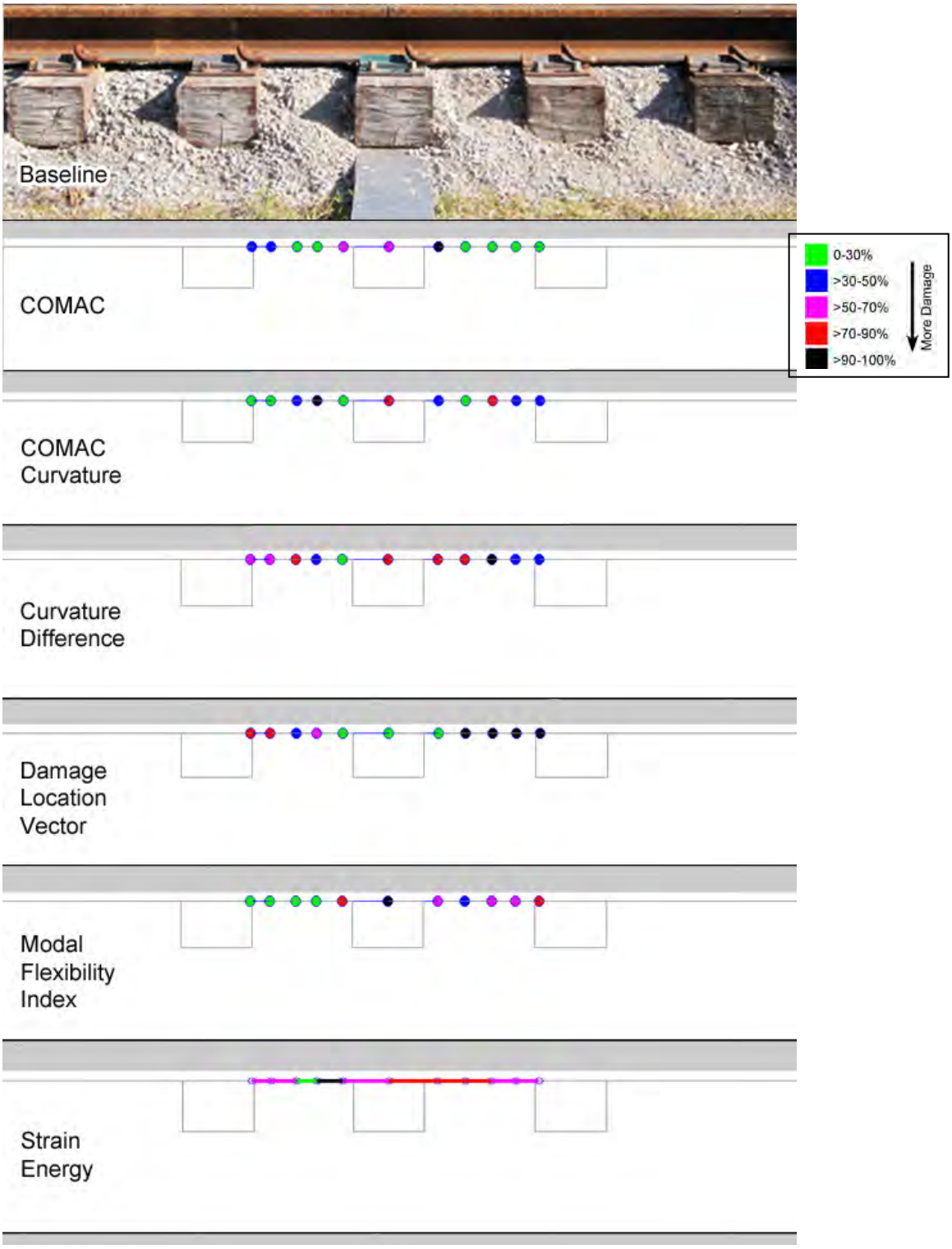


**Figure 53. Visual damage indication results of the structural health program.**

## Experiment 2: Bridge Scale Model

With concrete to concrete gravity connections, the "undamaged" measurements are used as a baseline for comparison. The 171 signals (57 locations at three directions each) are summed into the cumulative frequency response shown in Figure 54. Thirty-one modes were identified less than 250 Hz, the most common structural-to-acoustic limit. Major peaks occur near 131 Hz and 140 Hz with five lesser peaks (near 152, 178, 201, 212, and 230 Hz). The associated mode shapes include translation, bending, torsion, and coupled combinations of these. Low frequency rigid body translation modes and their directions can be used to identify potential sway weaknesses; the strongest axis was the x-direction, which indicates good confinement in the longitudinal direction. Although the joint connections were strictly concrete, as-built imperfections in boundary conditions caused mode coupling. A record of the baseline is essential to quantification of later damage, which will be at the boundaries.

Additionally, slab distortion modes were identified from 15 to 28 Hz. These local modes would not alter with damage and thus are excluded.

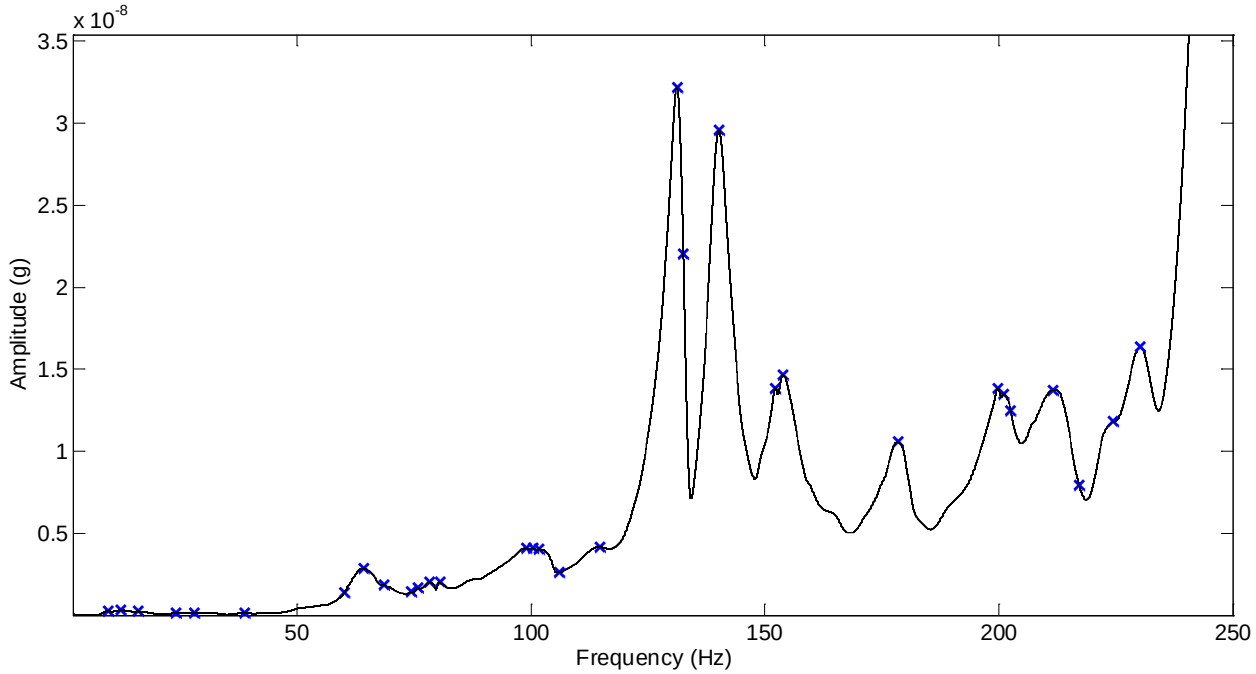


**Figure 54. The baseline's cumulative frequency response function and natural frequencies (x).**

Substructural damage was then induced at the pier. The center slab was lifted by a hydraulic jack, and a rubber bearing was inserted. With varying thickness and material, the rubber simulates different levels of connection softening due to soil, pile, or pier. Multiple damaged configurations were tested, and their vibrational response was compared to the baseline case. Note that the asymmetry of this setup actually assists in damage detection. The results presented herein are generated by inserting a 4"x42"x1/16" rubber strip underneath the right end of the center slab (Figure 55). Buna-N rubber was selected with a shore durometer of 70 (type A), the same hardness as automotive tire tread.

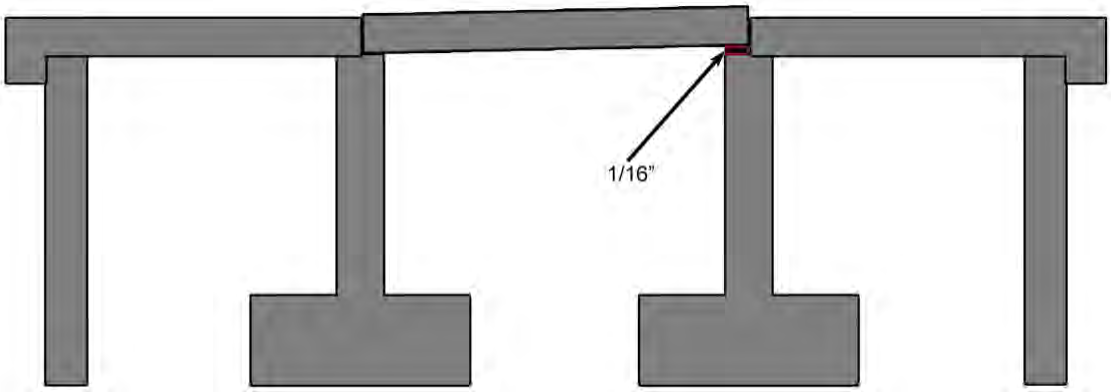


**Figure 55. Damaged configuration with a single softened connection.**

Within the same upper limit of 250 Hz, twenty-six modes were identified for the damaged case. The mode shapes were calculated and compared to the baseline: while similarity proved somewhat subjective, the 1/16" 70A rubber influenced the modal information as expected. Natural frequencies should decrease with damage; this is due to a decrease in stiffness with virtually no change in mass.

For **qualitative** comparison, Figure 56 depicts the resulting seven coordinated modes with amplification. Direction matters when directly comparing mode shapes, so the baseline/damaged coupled modes of 178/158 Hz and 200/168 Hz were excluded although similar in nature. While most literature compares one, two, or three modes, this work successfully matched the five coordinating modes provided in Table 4. All natural frequencies decreased in no discernible pattern. Selected views of coordinated modes are shown in Table 5. Coordinated Mode 1 is a rigid body translation in the y-direction, indicating that the most likely motion for this slab is sidesway: this is a common failure mode for bridges, so piers are often simulated via a push-over analysis. The damaged case shows similar sidesway behavior to the baseline. Coordinated Mode 2 exhibits rotation about the x-axis and translation in the y-direction; thus, this is a mode that couples rigid body rotation with rigid body translation. Compared to the baseline, the damaged case shows much more translation and slightly more coupled rotation. Coordinated Mode 3 couples rotation about the z-axis with bending in the positive z-direction. Compared to the baseline, the damaged case shows more disorganized bending and the right side (where the rubber was placed) shows significantly more translation. Coordinated Mode 4 is a slab rotation about the z-axis and bending in the negative z-direction. Some slight translation is also detected. Compared to the baseline, the damaged case shows less organization overall. Coordinated Mode 5 exhibits rotation about the x-axis that becomes disorganized when pier damage is inflicted. This mode is also coupled with second-order bending in the z-direction and slab distortion.

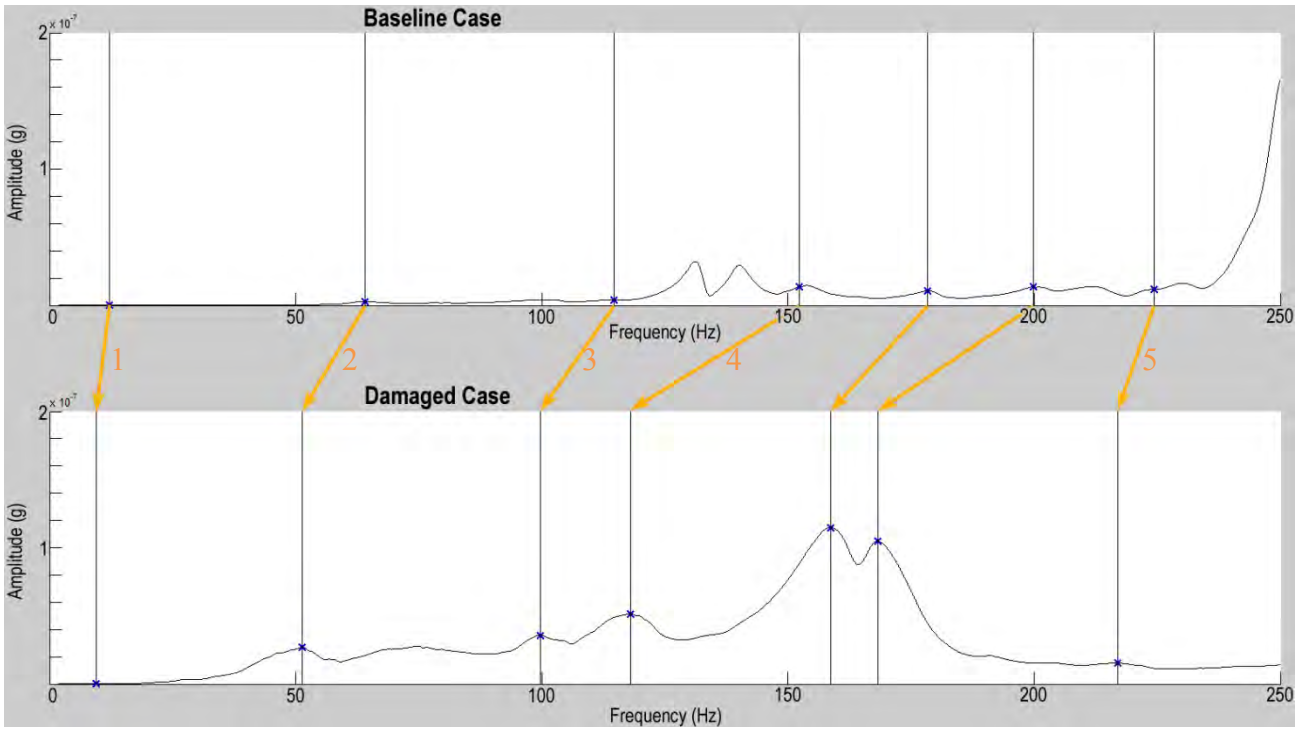


**Figure 56. Natural frequencies of coordinated scale bridge modes shift downward due to damage.**

**Table 4. Resulting coordinated modes.**

| Coordinated Mode Number | Baseline Frequency (Hz) | Damaged Frequency (Hz) | Modal Description |
|---|---|---|---|
| 1 | 12.23 | 9.53 | Translation |
| 2 | 64.17 | 51.40 | Rotation & Translation |
| 3 | 114.63 | 99.71 | Torsion & Bending |
| 4 | 153.83 | 118.10 | Bending & Translation |
| 5 | 224.41 | 216.99 | Rotation & Bending |

**Table 5. Coordinated scale bridge mode shape plots (selected views).**

Coordinated Mode 1

Baseline

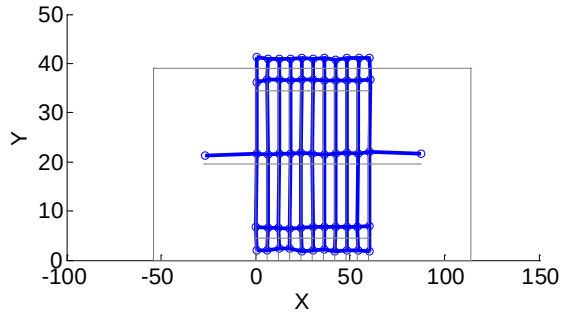


Damaged

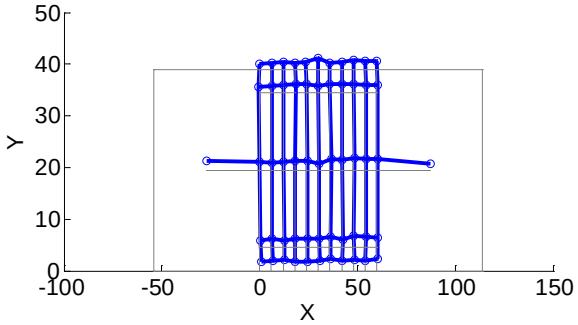


Coordinated Mode 2

Baseline

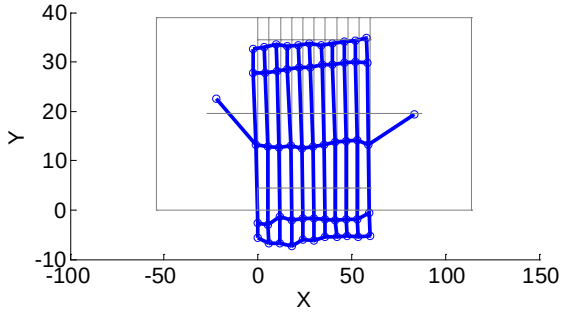


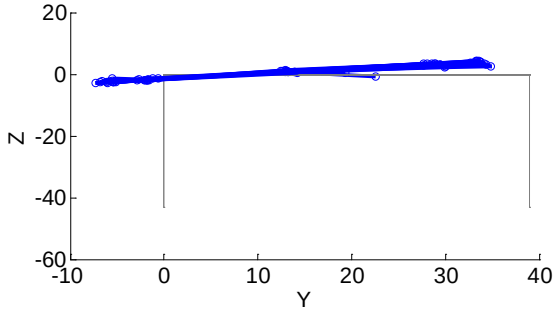


Damaged

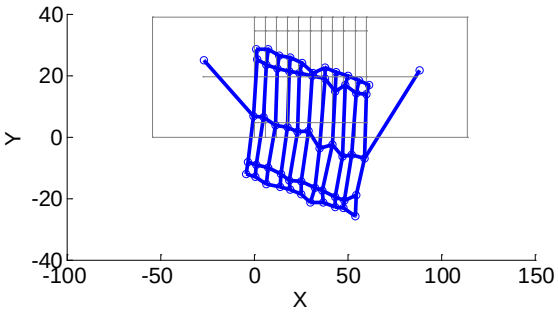


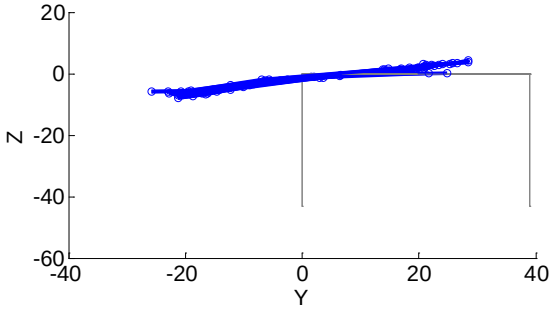


Coordinated Mode 3

Baseline

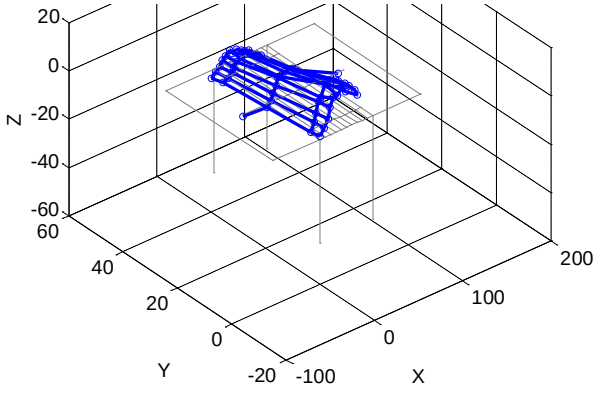


Damaged

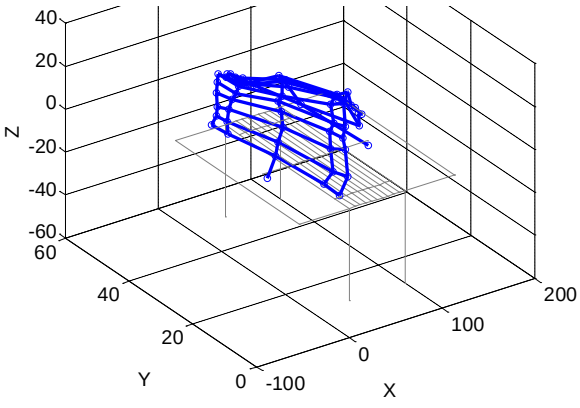

*(Table 5 continued)*

Coordinated Mode 4

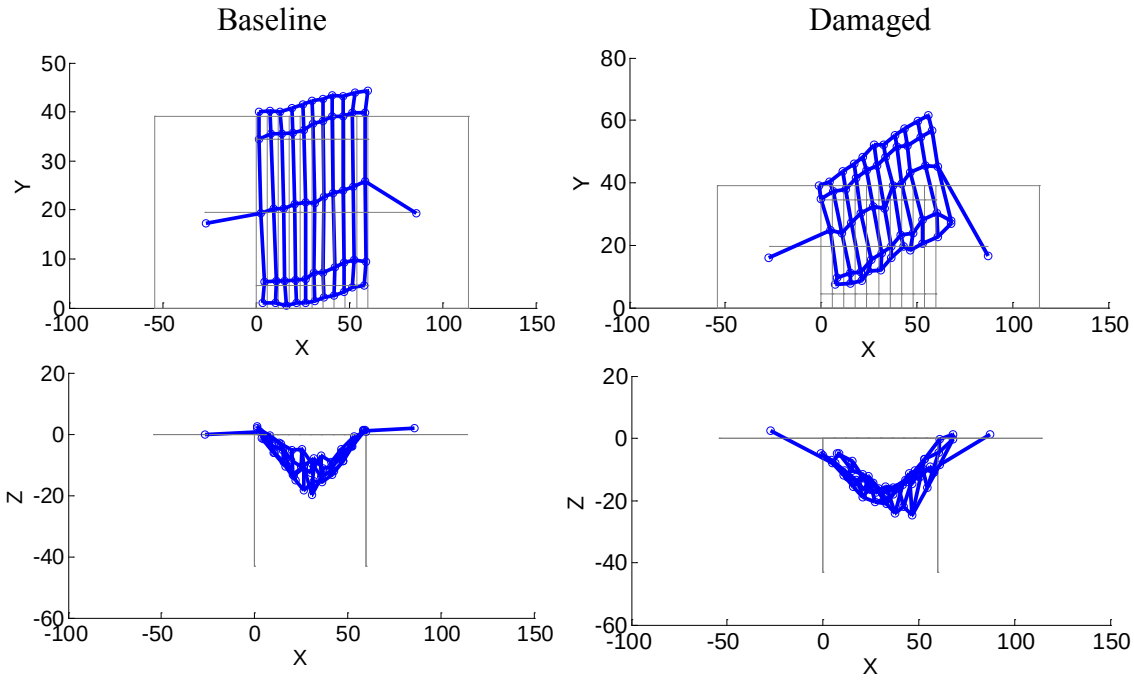


Coordinated Mode 5

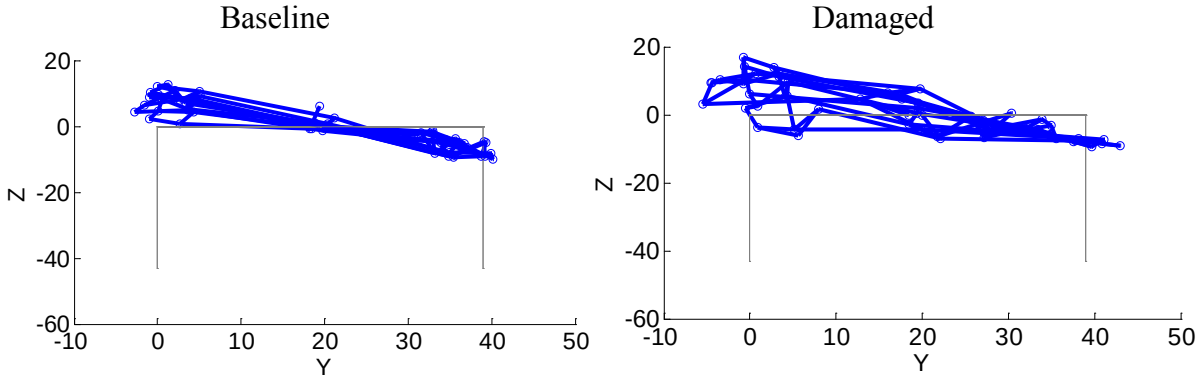

In order to **quantitatively** compare these modes, multiple structural health metrics were employed. The developed program has twelve different algorithms based upon seven indices, but not all are applicable to every data set. Key results are reported herein.

Modal Assurance Criteria (MAC) directly correlates an undamaged mode shape to a damaged mode shape. The MAC value is determined by applying the following equation to each row of the damaged and undamaged mode shape matrices:

$$\boldsymbol{MAC_i} = \frac{|\boldsymbol{\varphi_i \varphi_i^*}|}{(\boldsymbol{\varphi_i \varphi_i^T})(\boldsymbol{\varphi_i^{*T} \varphi_i^*})} \quad \textbf{(1)}$$

where $\phi_i$ is the undamaged mode shape for the *i*th mode and $\phi_i^*$ is the damaged mode shape for the *i*th mode. Note that *T* represents the transpose of the matrix. The result is an *i x 1* matrix with values for the correlation of each mode. A value of one represents full correlation (no damage) whereas a value of zero represents no correlation (possibility of major damage). Thus, level of damage is indicated but not location (*27*).

The results for the scale model bridge are provided in Table 6. Note that level is indicated, but not location. Red represents the minimum correlating measures, Modes 2 and 5 in the x-direction, which indicate the rubber greatly affected rigid body rotation. Green represents the maximum correlating measures, Modes 1 through 4 in the y-direction. It also appears that modes can show conflicting results and the thresholds seem arbitrary.

**Table 6. Modal Assurance Criteria (MAC) results for each direction by mode.**

| | **MAC (x)** | **MAC (y)** | **MAC (z)** |
|---|---|---|---|
| Mode 1 | 0.412 | 0.962 | 0.349 |
| Mode 2 | 0.006 | 0.900 | 0.579 |
| Mode 3 | 0.853 | 0.914 | 0.789 |
| Mode 4 | 0.388 | 0.926 | 0.776 |
| Mode 5 | 0.118 | 0.397 | 0.534 |

Coordinate Modal Assurance Criterion (COMAC) correlates changes in mode shape points, *j*, after summing over all modes, *m*. COMAC values are determined by applying the formula

$$COMAC_j = \frac{(\sum_{i=1}^{m} |\varphi_{ij} \cdot \varphi_{ij}^*|)^2}{\sum_{i=1}^{m} \varphi_{ij}^2 \cdot \sum_{i=1}^{m} \varphi_{ij}^{*2}} \quad . \quad (2)$$

The result is a *1 x j* matrix with values for the correlation of each point for all modes. Like MAC, a value of one represents full correlation (no damage) whereas a value of zero represents no correlation (possibility of major damage). However, COMAC does indicate location *j* of damage (*28*).

COMAC results are presented in graphic form in Figure 57. Although the thresholds have been selected arbitrarily, green represents little indicated damage at that point (potentially "safe") while red and black represent much indicated damage at that point (potentially "unsafe"). Overall, these results show a great sensitivity to damage, but the thresholds need more study to prevent false positives. Here, there are too many positives to isolate that damage occurred at the right side of the center slab.

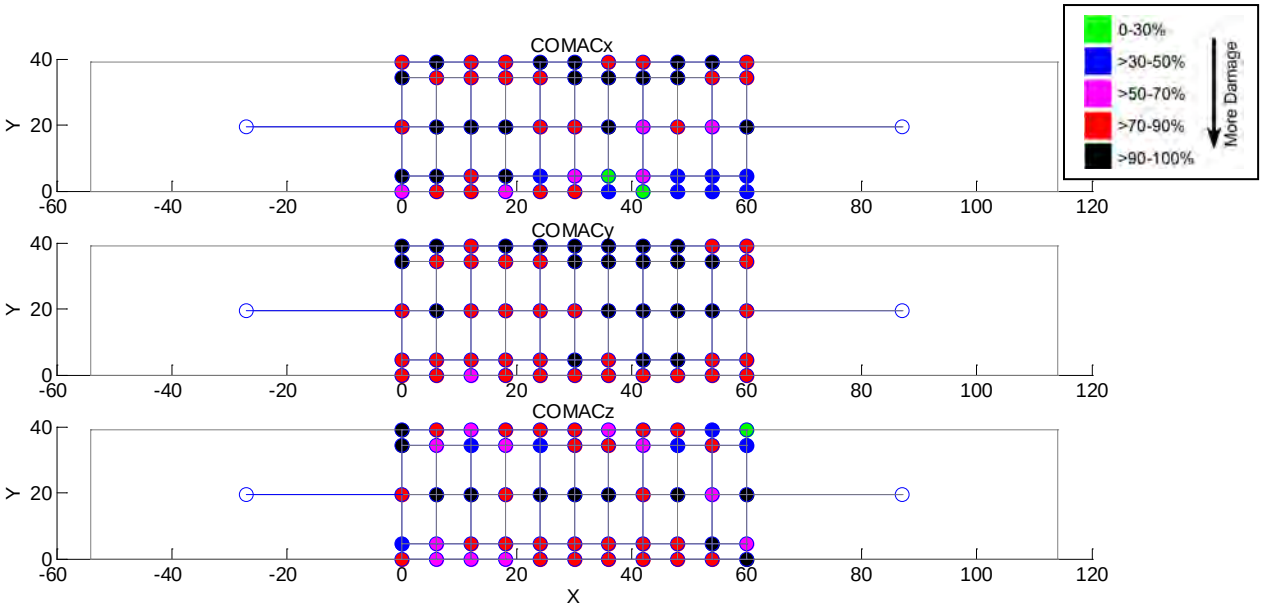


**Figure 57. Coordinate Modal Assurance Criterion (COMAC) results for each direction by location.**

The flexibility of a structure can be estimated using the mode shapes ϕ with the natural frequencies ω. Since the actual stiffness matrix is unknown, a proportional flexibility matrix *F* is found for both the damaged and undamaged cases. The inverse of the square of the natural frequency is multiplied by the square of each point's value (*29*). For example, for the undamaged case, the flexibility matrix is

$$F_{ij} = \frac{1}{\omega_i^2} \varphi_{ij} \varphi_{ij}^T \, . \qquad \textbf{(3)}$$

This can then be used in three possible damage indicators:

- Absolute Difference – Subtracting the proportional flexibility matrix of the undamaged structure from the proportional flexibility matrix of the damaged structure and taking the absolute value. The largest values of absolute change represent possible locations of damage.
- Percent Difference – Taking the absolute value of the difference between the proportional flexibility matrices of the damaged and undamaged cases and dividing that value by the proportional flexibility matrix of the undamaged structure. The largest values of percent change represent possible locations of damage.
- Normalized Modal Flexibility Index (ZMFI) – Finding the Modal Flexibility Index (MFI) by using the diagonal terms of the proportional flexibility matrix. This value is then normalized to obtain the ZMFI. Values not within the range of -2 to 2 indicate possible damage locations with a 95% confidence level (*30*).

For the scale model bridge, the absolute difference method on modal flexibility resulted in extremely small values on the order of $10^{-14}$. No trends could be identified. The percent difference method resulted in extremely large values: the maxima were 2.2E4%, 6.9E5%, and 1.2E8% in the x, y, and z-directions, respectively. If a threshold of 100% indicates damage, many false positives would result. However, Mode 2 values were significant for both x and z-directions, which is consistent with MAC. As illustrated in Figure 58, the normalized modal flexibility index showed less sensitivity and did not cause false positives. A concentration of damage occurs on the right side in the y-direction: this is a good result for this case, and it shows that the sway has been released by the inserted rubber.

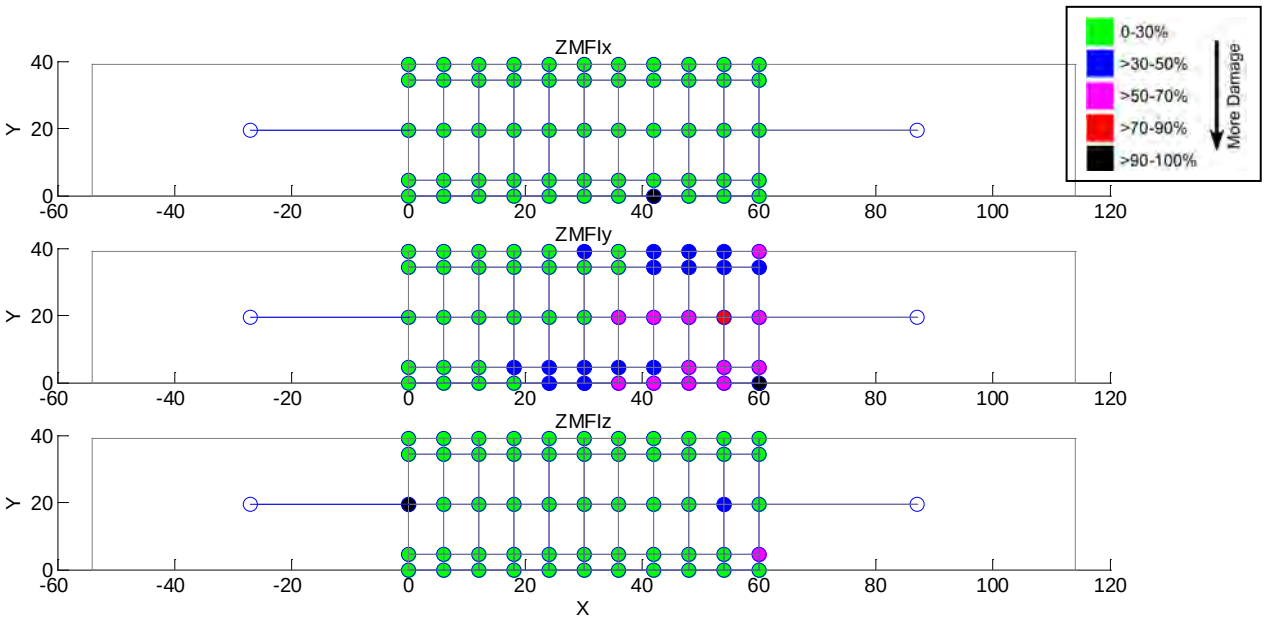


**Figure 58. Normalized Modal Flexibility Index (ZMFI) results for each direction by location.**

Curvature estimates provide more sensitive metrics than direct mode shape comparisons. The curvature of a mode shape is found by taking the second derivative of the modal displacement. A second order central finite difference estimate is used to find the second derivative between the displacement points; forward and backward finite difference estimates are used to find the first and last value, respectively. The relative locations of the data points are required for these numerical estimates. As in (*27*) and (*30*), the curvature is calculated for both damaged and undamaged modes and then can be used in four possible damage indicators:

- Absolute Difference – The absolute value of the difference between the curvature calculated using the damaged modal displacement and that calculated using the undamaged modal displacement.
- Division – The damaged curvature divided by the undamaged curvature.
- Total Division – Sum of all of the modes for the damaged curvature divided by the sum of all of the modes for the undamaged curvature. This gives a value for each node.
- COMAC – coordinate modal assurance criterion of the damaged and undamaged curvature matrices (*31*).

The absolute difference method on curvature showed the strange results in Figure 59: no damage in the x-direction, intermediate damage in the y-direction, and complete damage in the z-direction. The algorithm was checked several times, but it appears that this method is a failure. Division and total division of curvatures also did not result in any discernible trends. However, performing COMAC on the curvature did indicate right side damage in the z-direction. Figure 60 shows a concentration of red near the right side, but changes are not as apparent in x or y-directions.

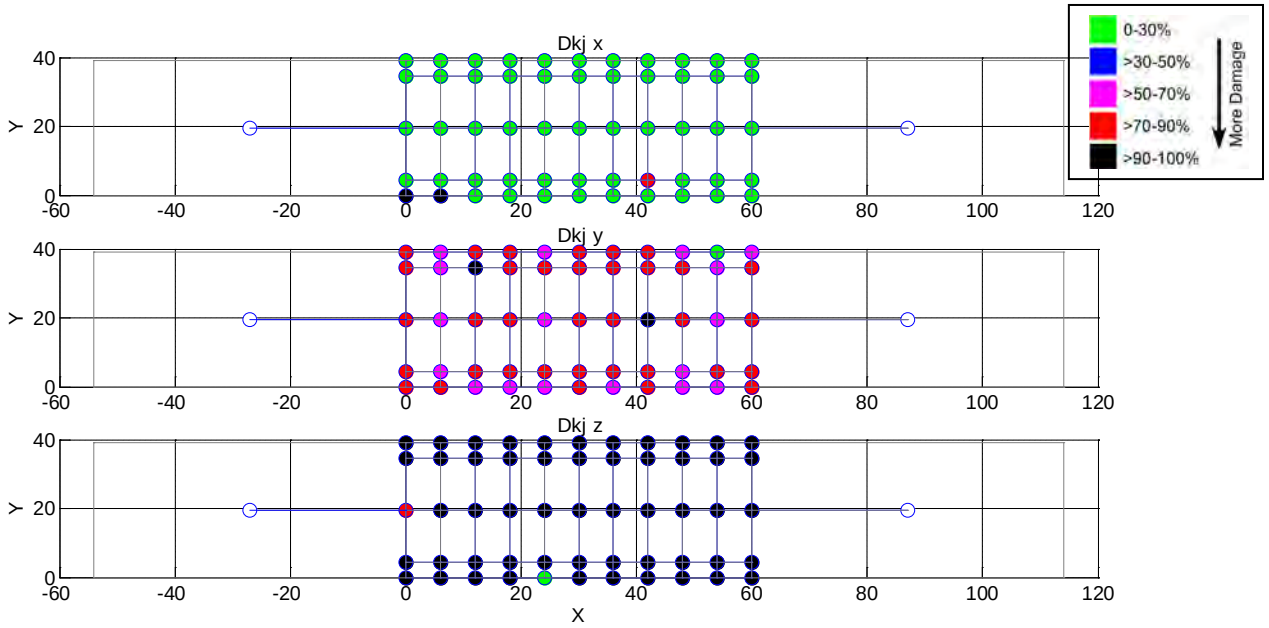


**Figure 59. Absolute difference on curvature results for each direction by location.**

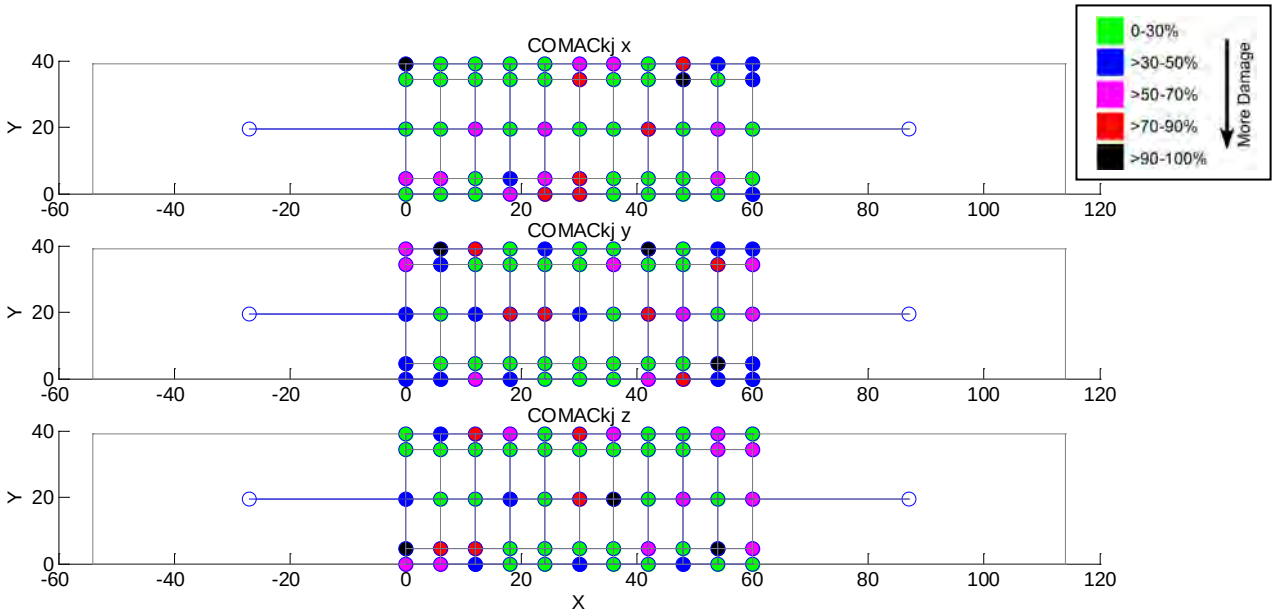


**Figure 60. COMAC on curvature results for each direction by location.**

Calculation of the Damage Location Vector (DLV) involves direct comparison of two frequency response functions: no modal decomposition is required, an advantage. The DLV is found by subtracting the undamaged frequency response magnitude from the damaged frequency response magnitude. The result is then summed across all modes to obtain an indicator quantifying the fluctuations in the frequency response functions (*32*).

The Damage Location Vector in the y-direction provides excellent results as shown in Figure 61. Damage increases towards the right side, peaking in the 80% range. Note that this is consistent with the Normalized Modal Flexibility Index. The outer sensor lines show damage in the x-direction, perhaps indicating an increase in torsion. The z-direction has some outer sensor line sensitivity and both end conditions show some damage.

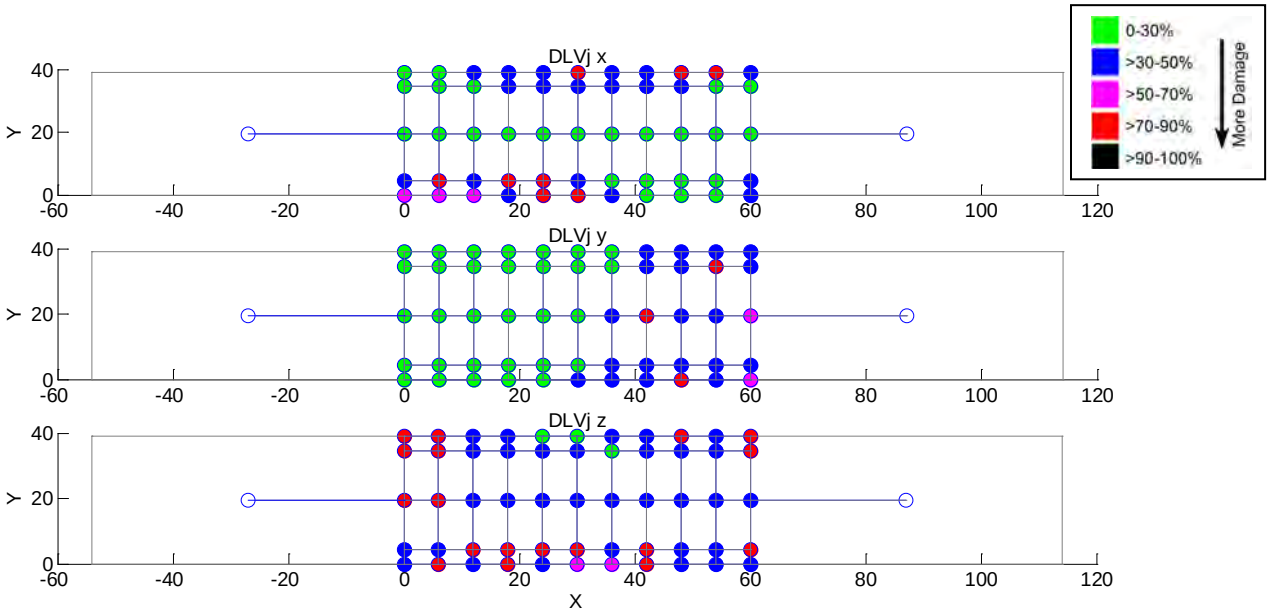


**Figure 61. Damage Location Vector (DLV) results for each direction by location.**

Two other damage indices are programmed for special cases. The strain energy method requires material and geometry information in the forms of modulus of elasticity, *E*, and area moment of inertia, *I*. The mode shape area method is best applied when there is a high density of spatial data.

## Experiment 3: Full Scale Bridge Test

Results are presented herein for both the deck surface and the underneath girder testing.

### Deck Testing Results

Observations about the bridge were also made based on the uniqueness of each vehicle's time history. A typical time history is shown in Figure 62: note that all three axes of data are overlaid. Large jumps in the amplitude are visible on each vehicle trace. These jumps (shown by red arrows) are thought to occur due to settlement on both of the bridge abutments. This settlement has caused the sudden increase in the excitation due to the elevation difference at expansion joints, creating a jarring force and an audible noise when the vehicle crosses. This is similar to time histories when a vehicle hits a pothole, for example.

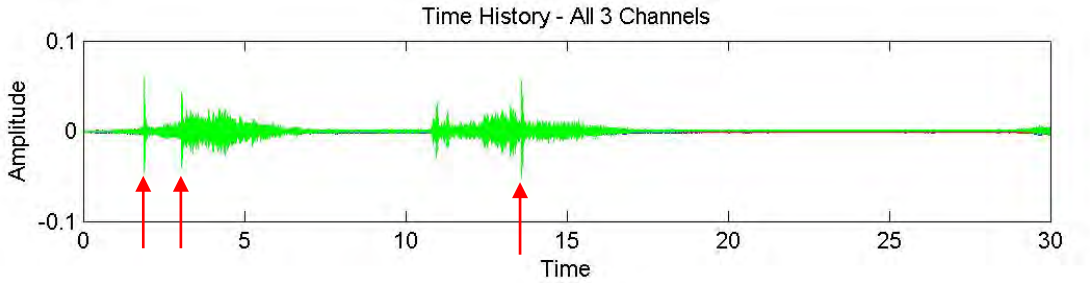


**Figure 62. Time history on point 25 showing the crossing of two cars during a 30-second period.**

The LDV measures a projection of a velocity vector onto the direction of the LDV beam (*33*). A vector diagram in shown in Figure 63. The velocity magnitude at a given time moment measured with a LDV is defined by

$$V = V_z \sin\alpha + V_x \cos\alpha \qquad (4)$$

where α is the grazing angle of the LDV beam, and $\mathbf{V_z}$ and $\mathbf{V_x}$ are the velocity components along Z- and X-axes, respectively.

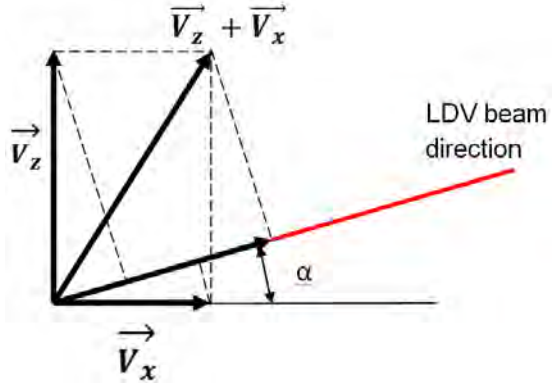


**Figure 63. Vector diagram for the LDV vibration measurements on the top of the bridge.**

The sensitivity of a LDV to Z- and X-components of vibration depends on the grazing angle value. In the current experiment, the value of the grazing angle α varied with the position of a measurement point from 4.5 degrees for the points at the center line of the middle deck to 13 degrees for the points at the edge of outer decks. Low grazing angle geometry makes measurements more sensitive to X-component than to Z-component. For example, for 4.5 degrees angle, the sensitivity to X-component is approximately 13 times higher than to Z-component using the previous equation. Thus, low angle measurement geometry can be accurately used for vibration measurements only if a contribution of one of the components to the LDV signal is significantly smaller than the contribution of the other component, which can be neglected.

In order to assess the ability of LDV to measure bridge vibrations in a low grazing angle configuration, accelerometer measurements at several points at the center line of the middle deck have been used for comparison. Figure 64 shows vibration spectra of Z- and X-components measured with accelerometers at points 6, 15, 22 and 31 (refer to Fig. 33). This result shows that longitudinal vibrations (X-direction) are 10 to 30 times lesser than deck bending vibrations (Z-direction). Since the LDV sensitivity at 4.5 degrees angle is 13 times higher for X than Z, these smaller X-direction vibrations contribute the same order of value to the LDV signal as the more dominant Z-direction vibrations.

The overall result is signal interference that may appear as highly coupled signals. The completed full-scale experiment shows that using a single point LDV located at a bridge abutment employing a low grazing angle is likely to be unsuccessful: the configuration does not allow measurements of separate vibration components of the bridge.

Possible adjustments can be made to improve the success of remote vibration measurement of bridge decks. First, a high grazing angle configuration must be enforced. A right-angle shot would be ideal, so, for example, a single LDV installed on a high mast can make the direction of the LDV beam closer to vertical. Second, corrections can be employed by exploiting multiple measurements. Two LDVs can measure the vibration at the same point on the bridge surface using different angles. Lastly, a different instrument can be implemented. LDV model RSV-150 (approximately $100,000 from Polytec, Inc.) could be recommended as a tool for remote vibration measurement of bridges. Due to higher laser power and larger receiving aperture, it will allow vibration sensing of bridge components without using retroreflectors at longer distances.

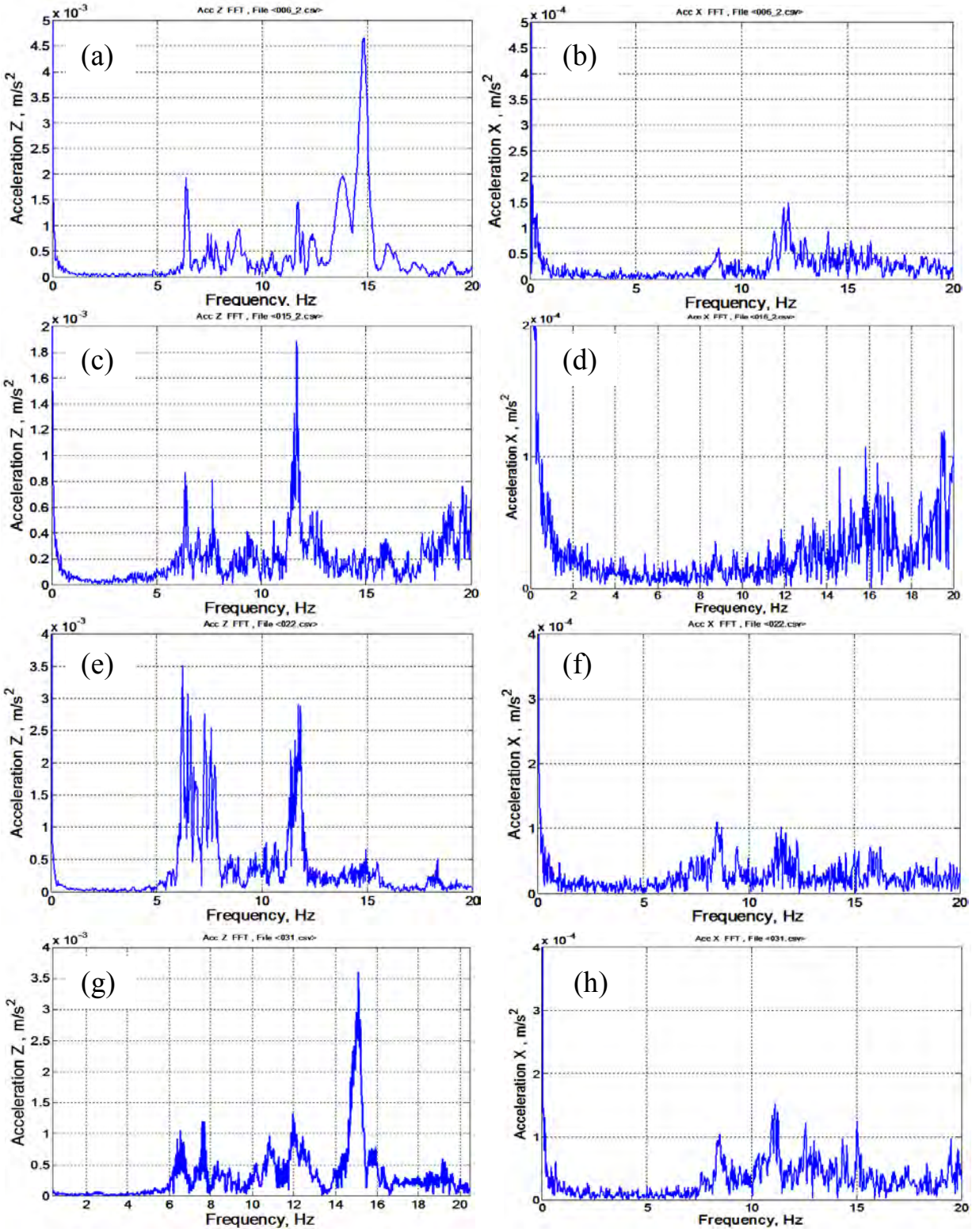


**Figure 64. Vibration spectra of four points along the centerline of the target deck. (a), (b) -Z- and X- components in point 6; (c), (d) -Z- and X- components in point 15; (e), (f) -Z- and X- components in point 22; (g), (h) -Z- and X- components in point 31.**

## Girder Testing Results

The bottom accelerometers also had connection interference, sometimes extreme, due to the BNC cords which were hanging from the girders. The incidental motion of these cords caused some data dropout. The accelerometers on the bottom of the bridge exhibited sensor drift as compared to their deck counterparts. Figure 65 demonstrates the effect of this issue on the frequency response. The red boxes show that sensitivity to frequencies less than about 5 Hz is eliminated: the sensor drift in the time history causes the frequency results to be skewed.

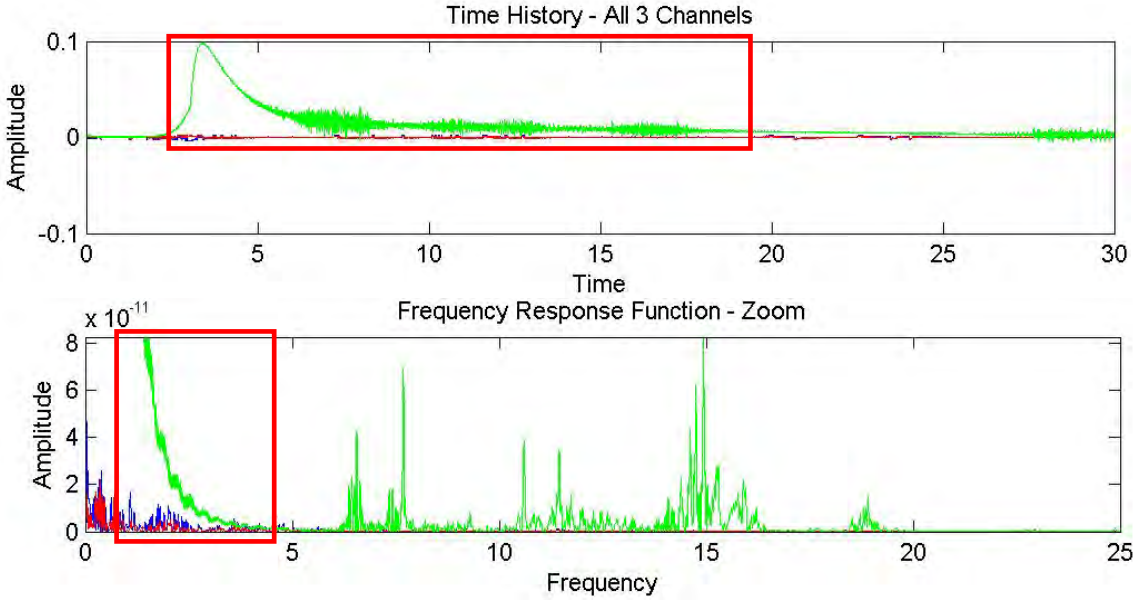


**Figure 65. Sensor drift effects for Point 39 in both time history (top) and frequency response (bottom).**

Figure 66 shows representative examples of vibration signals and their spectra obtained with the LDV pointed at a corner cube array and the accelerometer. Note that the excitation was caused by a vehicle passing across the bridge from 15 to 25 seconds and another vehicle entering the area after 25 seconds. The two time histories have different units but similar traces; the LDV shows a bit more susceptibility to noise due to its characteristic sensitivity. The vibration spectra measured with the LDV and the accelerometer appear very similar, showing natural frequency peaks at the same locations.

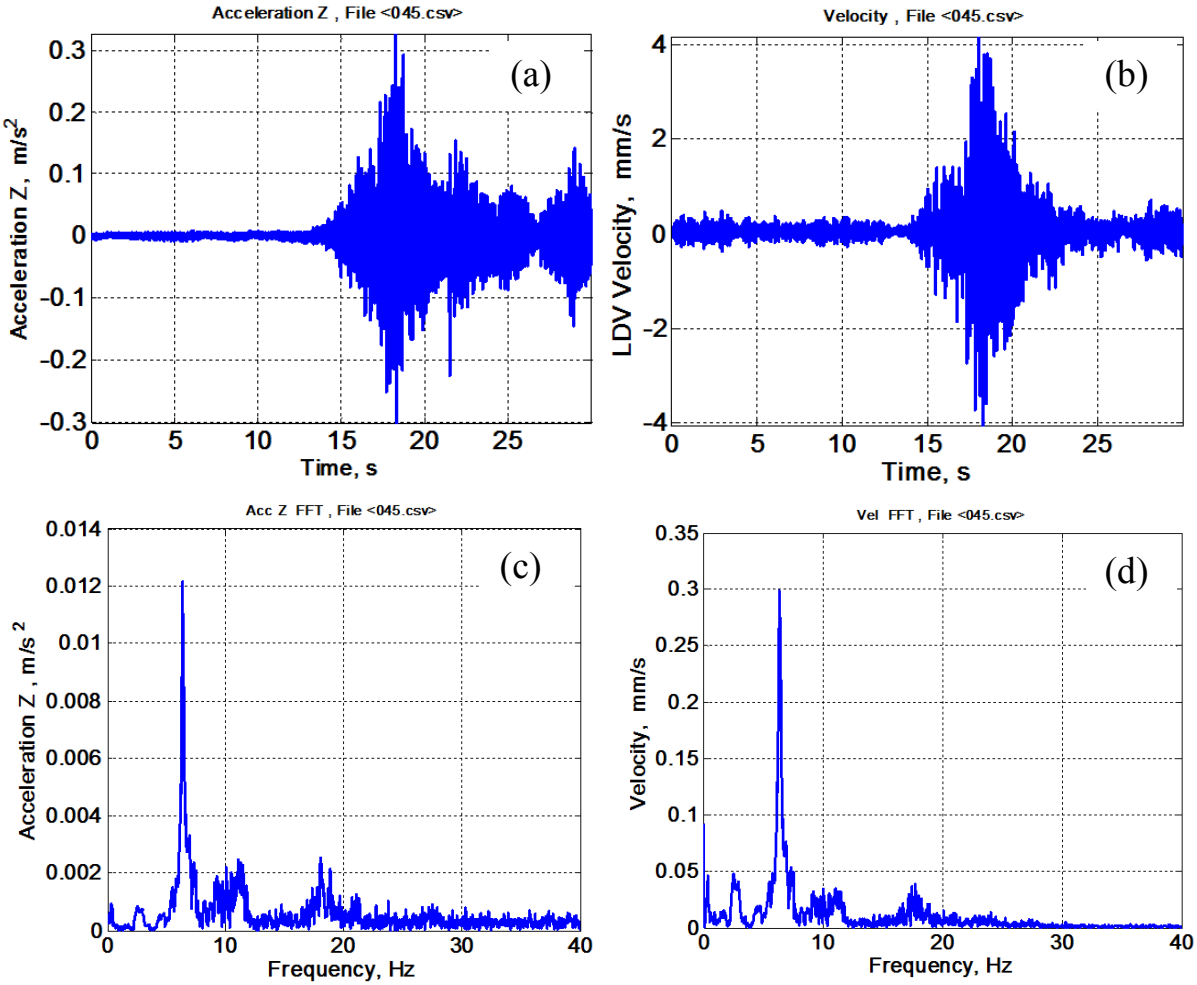


**Figure 66. Simultaneous time histories for Point 45 of the (a) accelerometer and (b) LDV with a reflector. Corresponding frequency spectra for (c) acceleration and (d) velocity.**

In order to make a quantitative comparison of LDV and accelerometer measurements, the pseudovelocity spectrum of Figure 67(a) was calculated from the acceleration spectrum. This calculated velocity spectrum shown in red is practically identical in peak behavior to the LDV's, shown in blue (Figure 66(d)), except near 0 Hz. The large DC value in Figure 67(a) spectrum is due to an artifact of the conversion of acceleration into velocity.

A standard way to evaluate the similarity of two signals is to calculate their coherence function. The coherence between the accelerometer and the LDV spectra is shown in Figure 67(b). The coherence function value is more than 0.9, except frequencies below 2 Hz and between 15 and 25 Hz. These high values indicate strong similarity between the LDV and accelerometer signals. The low coherence function values less than 2 Hz is due to the greater sensitivity of the LDV. However, the low coherence between 15 to 25 Hz is significant and could be caused by a vibration response of the LDV tripod. The difference in the two spectra in this frequency range is shown by the box in Figure 67(a).

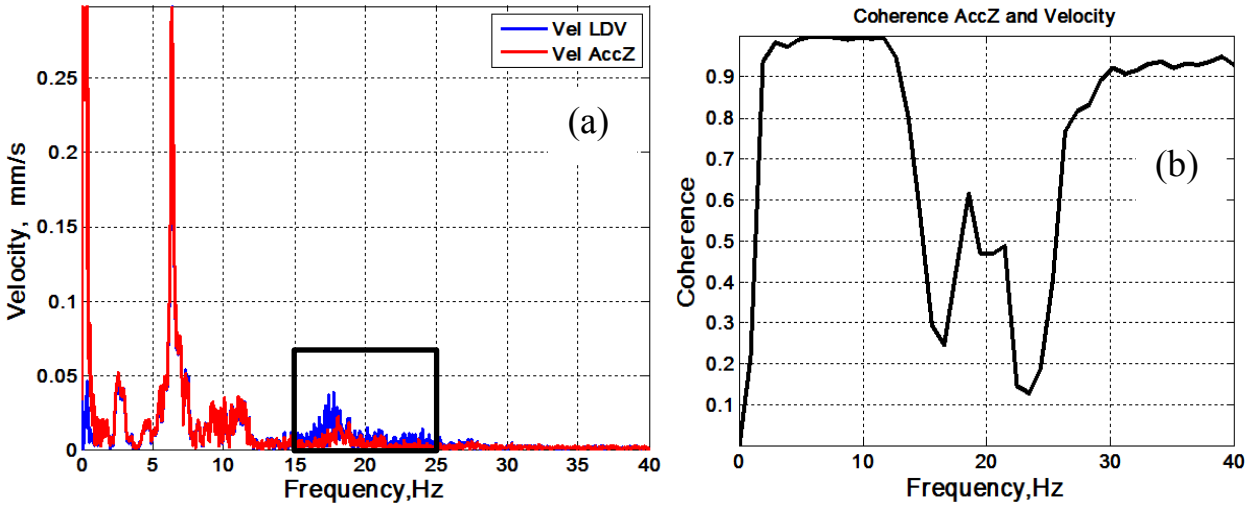


**Figure 67. Quantitative comparison for Point 45 via (a) velocity spectrum with the LDV (blue) and as calculated from the acceleration spectra (red) and (b) their coherence function.**

Figure 68 shows representative examples of vibration signals and their spectra obtained with the LDV pointed at the unconditioned girder surface and the accelerometer. That is, no corner cube array was used. Some angular adjustment and focusing of the laser beam on the object surface was necessary in order to maximize the light power reflected back and reduce velocity noise. The two time histories have similar traces, but the LDV shows more noise due to lack of a fully reflective surface. The vibration spectra measured with the LDV and the accelerometer appear very similar, showing natural frequency peaks at the same locations.

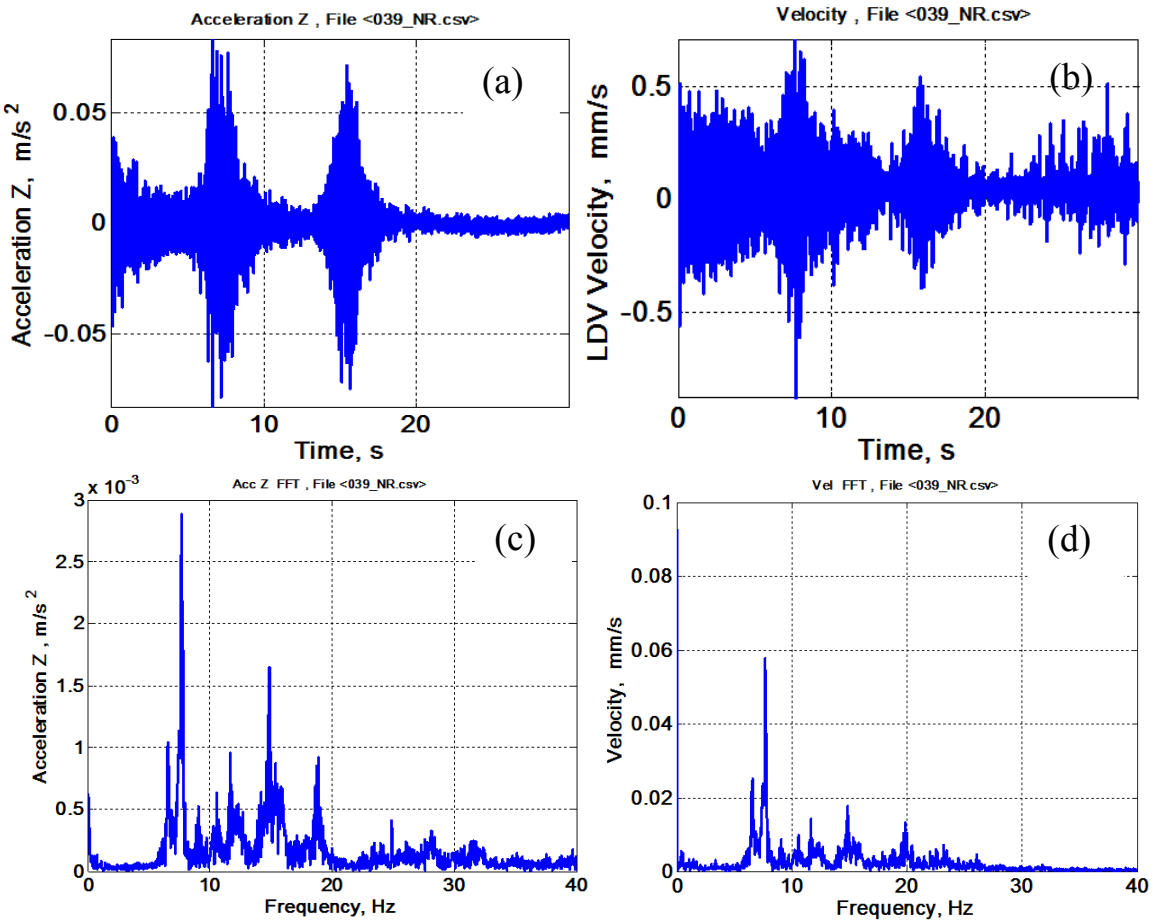


**Figure 68. Simultaneous time histories for Point 39 of the (a) accelerometer and (b) LDV without a reflector (girder surface). Corresponding frequency spectra for (c) acceleration and (d) velocity.**

In order to make a quantitative comparison of LDV and accelerometer measurements, the pseudovelocity spectrum of Figure 69(a) was calculated from the acceleration spectrum. This calculated velocity spectrum shown in red shows practically the same peak behavior to the LDV's, shown in blue (Figure 68(d)). The large DC value near 0 Hz in Figure 69(a) spectrum is again due to an artifact of the conversion of acceleration into velocity. There is a difference in the spectra for the frequencies above 17 Hz, which may be caused by a vibration response of the LDV tripod.

The coherence function between the accelerometer and the LDV spectra is shown in Figure 69(b). The overall coherence is much lower between the accelerometer and the LDV when the latter is pointing at a bare surface rather than a retroreflector. The reason could be higher LDV noise caused by lower amount of reflected light. The low coherence between 17 to 25 Hz is again significant and could be caused by a vibration response of the LDV tripod. The difference in the two spectra in this frequency range is shown by the box in Figure 69(a).

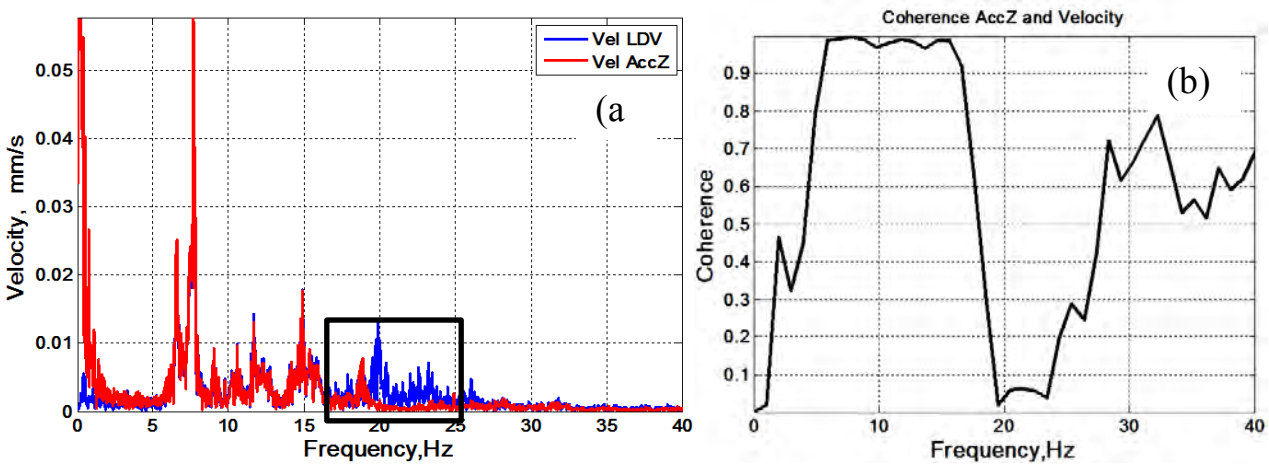


**Figure 69. Quantitative comparison for Point 39 via (a) velocity spectrum with the LDV (blue) and as calculated from the acceleration spectra (red) and (b) their coherence function.**

Overall, measurements underneath the bridge provide vibration spectra peaks which are in excellent agreement with the vibration spectra measured with accelerometers. The major vibration of the bridge is successfully captured by a LDV in both scenarios, with and without a retroreflector. Thus, an LDV can replace accelerometers in bridge vibration measurements of girders.

Possible adjustments can be made to improve the success of remote vibration measurement of bridge girders. A high grazing angle configuration must be enforced; a right-angle shot showed excellent results herein. While a reflector is not required, a reflective surface will provide the best results. Surface conditioning is recommended if members are severely corroded or dirty. Alternatively, a different instrument can be implemented. LDV model RSV-150 (approximately $100,000 from Polytec, Inc.) could overcome signal loss via higher laser power and larger receiving aperture.

## Finite Element (FE) Modeling

Performed throughout the project, the finite element contributions support both the model and operational bridge experiments.

### Scale Model Bridge

Utilizing the completed model, eigenvalue analysis was performed using the software to obtain the frequencies less than 250 Hz. A few of the characteristic modes with no bearings (large *E*) are shown in Figure 70 and summarized in Table 7. The first three modes cause deck deformation and thus are deemed characteristic (longitudinal translation, torsion with lateral translation, and vertical bending). As predicted by the planning study, all natural frequencies and in some cases mode order vary with assumed Young's modulus for the contact elements. The center deck vertical bending mode varies from 127 Hz to 170 Hz depending upon the contact stiffness while a smaller variation is observed in the deck torsion mode.

**Table 7. Selected characteristic modes of the SAP2000 scale bridge baseline model.**

| Frequency (Hz) | Description |
|---|---|
| 53.6 | Global deck longitudinal translation accompanied by out-of-plane pier cantilever bending and associated in-phase deck bending in double curvature |
| 162.9 | Global deck transverse translation accompanied by in-plane pier cantilever bending and associated deck torsion |
| 170.0 | Global deck vertical translation accompanied by no-sway pier end rotation / bending and associated out-of-phase deck vertical translation / bending |

**Qualitative** visual comparison of the characteristic modes with no rubber bearings indicates that the interaction between components is not currently represented well in the idealized FE modeling approach. While component deformation patterns (bending and torsion) match reasonably well, the frequencies and order of frequencies do not align well. This indicates that significant model updating and calibration of FE models will be required when applying the current approach to assessing degradation. Despite the lack of agreement in frequency response, the present study indicates reasonable agreement between the FE and experimental results in the absence of interaction effects.

An ongoing academic study offers an opportunity to identify some improvements in the current modeling approach that might give better agreement for the current model bridge case. Specifically, a decoupling of the lateral and vertical interaction bearing stiffness could provide a mechanism for exploring the sensitivity of the characteristic modes to these relative stiffness values.

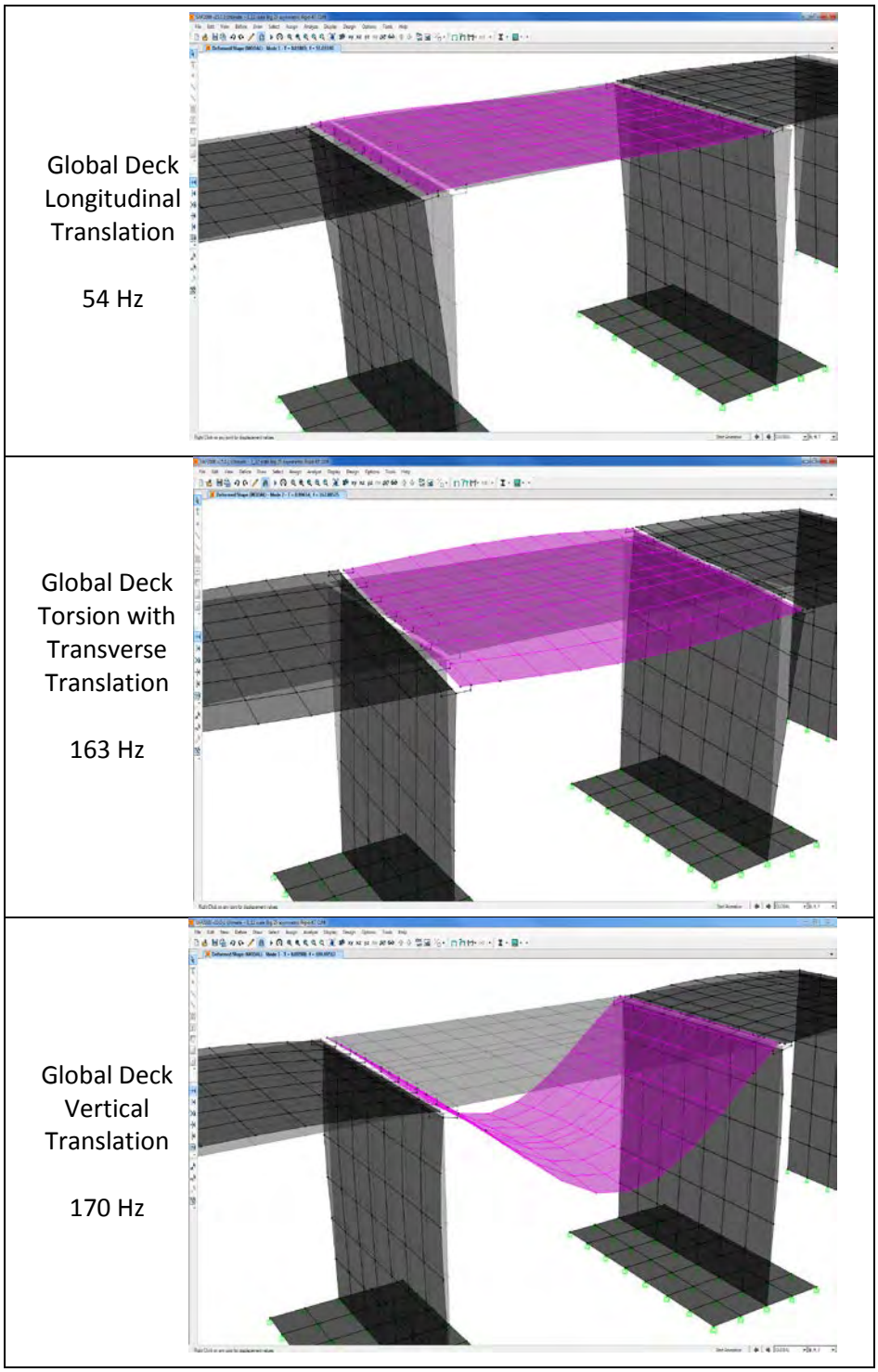


**Figure 70. Selected characteristic modes of the SAP2000 scale bridge baseline model.**

**Quantitative** comparison reveals that these frequencies appear high as compared to experimental data. In fact, modeled Mode 1 is exactly the opposite of the experimental modes. That is, the model allows more longitudinal translation while the lateral sideway is more dominant in the experiment. This difference leads to the conclusion that the modeled boundary conditions need refinement.

The value of the other two modeled mode shapes need to be quantitatively evaluated in order to determine their applicability to damage detection. To this end, the developed structural health program was employed for direct modal comparison. This is not for damage detection: the program is used to directly compare the experimental to modeled baseline to evaluate modeled mode shape value.

In order to better tune the model, quantitative modal comparison was performed. Modeled Mode 2 is a torsion mode that shows just 0.5% similarity to the experiments via Modal Assurance Criteria (MAC). The fundamental bending mode, Modeled Mode 3, shows a 65% similarity using MAC. Note that no rigid body rotation modes were allowed by the model, but the experiment showed this as another characteristic mode.

These values do not provide the locations of any discrepancies, which is why Coordinated Modal Assurance Criteria (COMAC) is often used in commercial programs as a comparison for the similarity of two modes. COMAC is used here to compare two sets of modes: the experimental baseline versus the SAP2000 finite element model. As illustrated in Figure 71, the x-direction centerline indicates disagreement that is most likely due to the experimental coupling of bending with some torsion. The y-direction shows a diagonal bias, indicating disagreement in the torsional mode. Lastly, the z-direction disagrees nearly everywhere. Tuning boundary conditions will be required for release or enforcement of DOFs to allow torsion and bending adjustments.

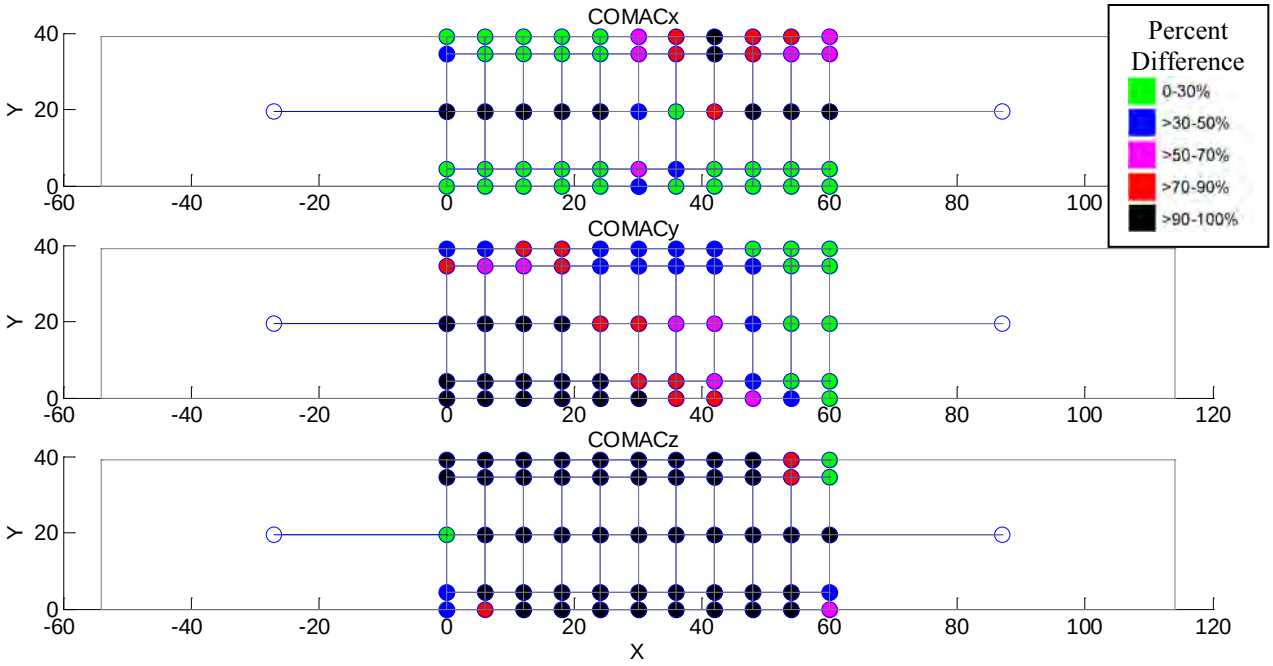


**Figure 71. Mode set comparison using COMAC for the experimental baseline versus the FE model.**

Other indicators were run for comparisons, but these are non-traditional for FE verification. Absolute difference in curvature showed very low levels in the x-direction, poor matching in the y-direction, and sporadic z-direction disagreement. Division of mode shape curvature exhibited extreme values along the longitudinal and transverse centerlines for both x and z-directions. COMAC on mode shape curvature showed similar results to the COMAC of Figure 71. The percent difference method on Modal Flexibility demonstrated large disagreements between x and z-directions, up to 4.8E5%. Lastly, the Normalized Modal Flexibility Index exhibited complete disagreement in both y and z-directions but reasonable results in the x-direction. Overall, the centerline shows the least agreement, implying that the bending mode most requires boundary tuning.

**Full Scale Bridge**

Eigenvalue analysis was performed to obtain the natural frequencies less than 250 Hz. With the large number of DOF, hundreds of resonances were found. Emphasis was thus placed upon identifying mode shapes representing significant movement of the system's center of gravity. That is, global deck motions were deemed characteristic while modes with local girder deformation, for example, were omitted. Figure 72 provides a few of these significant modes, which are generally representative of mode shapes in stiffened plates. Table 8 summarizes the resonant frequencies with their mode descriptions.

**Table 8. Characteristic modes for ABAQUS center span deck model of operational bridge**

| Frequency (Hz) | Description |
|---|---|
| 4.99 | Center deck vertical translation accompanied by out-of-plane composite deck bending |
| 5.41 | Center deck mid span rotation accompanied by out-of-plane composite deck bending / torsion |
| 9.21 | Center deck mid span rotation accompanied by higher mode out-of-plane composite deck bending / torsion |

Specific details in the superstructure, substructure, and surrounding soil are influential to field vibration testing observations; thus, modeling of any bridge depends upon the research focus. When compared, the prior soil-structure interaction study and the current center span deck study generate differences in modal properties. Resonances and modes depend a great deal upon the components, their interactions, and connectivity details as well as the relative importance of different model features in specific operating environments.

All these variations cause assessment of the influence of specific damage modes from vibration measurements difficult to identify. Some knowledge of the damage mechanisms and construction details must be established, and modeling certainly provides insight into how a specific damage mechanism can affect structural motion. In certain cases, the specific effect of damage on individual modes can be indicated for health evaluation, but the challenge is identifying these modes and their sensitivity to material and mechanical behavior. In the case of the present study, the composite deck construction behaves as a stiffened plate, but other configurations may respond differently.

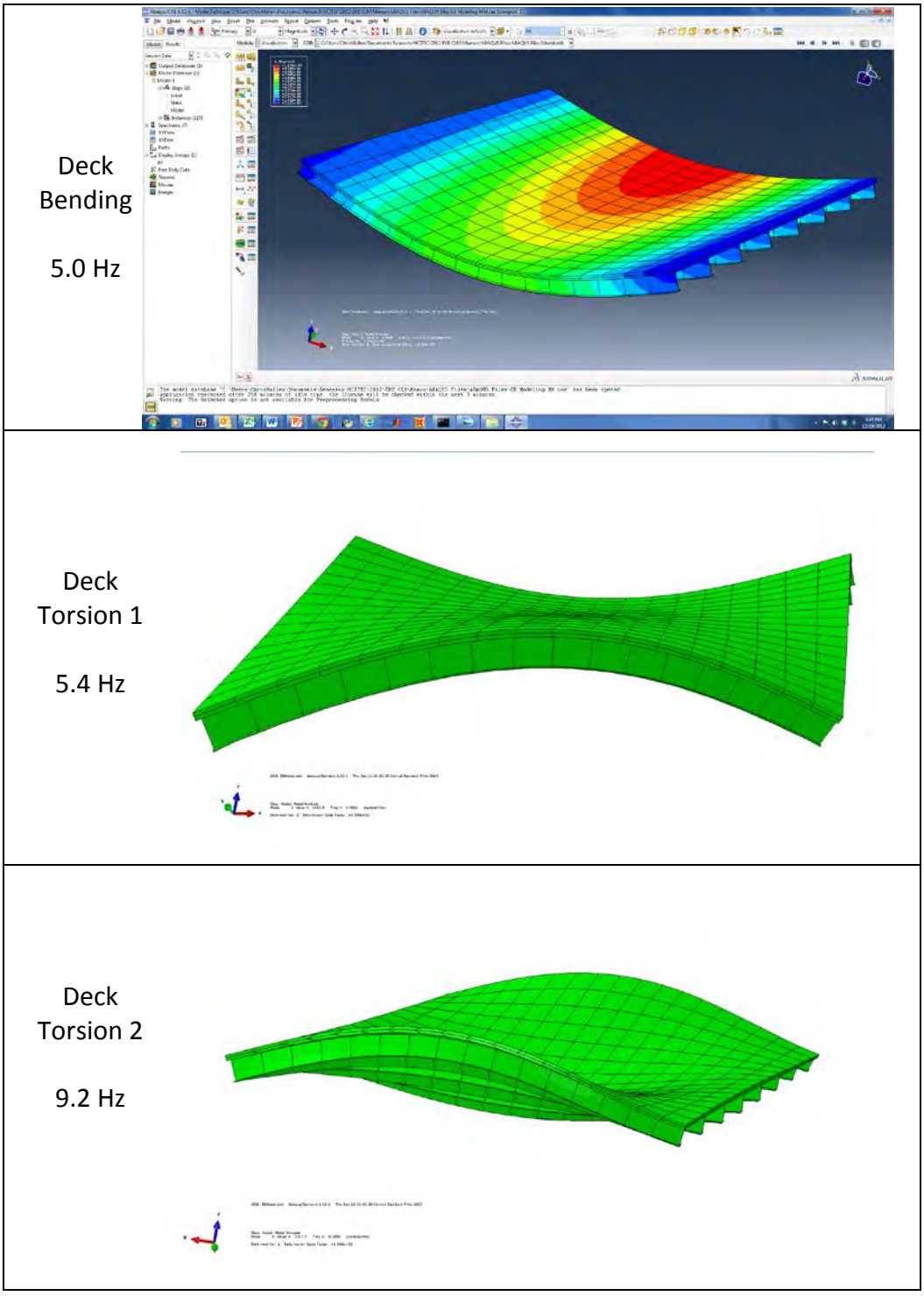


**Figure 72. Characteristic modes for ABAQUS model of the center span of the operational bridge.**

# CONCLUSIONS

Overall conclusions from the integrated project are first presented herein. Conclusions are then provided from each of the five primary activities of the project.

Contact non-destructive testing methods can be used for assessment of structural integrity but only in selected locations, which limits their practicality for inspection of large infrastructure. Due to the size of rail and road bridges, large spacing between test locations can result in poor mode capture and thus miss defects. Overcoming this obstacle, non-contact laser Doppler vibrometer (LDV) measurement can quickly provide dynamic characteristics of the structure at any selected location.

Employing reasonable spatial grids, LDV vibration measurements were sufficient to capture modal content in multiple experiments. The damage detection program output provided confidence that LDV velocity signals are sensitive enough to use for damage detection, and health indicators can judge the severity and approximate location of damage. Once attached to a sturdy base, the moving LDV also provided good resonance information despite some slight interference. Limitations include measurement distance and geometrical resolution.

In short, LDV use is a feasible option to augment inspection of rail and road bridges.

## 1. Experiment 1: Non-Contact Rail Inspection

The work herein demonstrates that damaged substructural components could be detected by analysis of the measured rail vibration. Vibration measurement via an LDV was experimentally evaluated, and modal content of the signal was sufficient to identify four coordinated modes. Each mode experienced decreased natural frequencies with damage, and qualitative analysis revealed an approximate location of damage. Quantitative analysis using damage indicators showed center tie damage, especially on the right side. The signals revealed a decoupling of the tie from the rail which allowed it to vertically “rattle” (Mode 3). Mode 1 showed 92% damage, which means that twisting motion of the center tie was released.

When compared to the stationary measurements, the major effect of the LDV’s transverse motion is the occurrence of narrow spikes in the recorded signal. These short spikes increase measurement noise which can mask small vibrations. However, the effect of these spikes was insignificant in the current series of experiments.

The rail testing also helped in decision-making on three bridge testing aspects:

sampling rate, length of sample, and measurement grid. For low frequency infrastructure, extreme oversampling (50,000 Samples/sec) causes too much noise in the resulting frequency responses. A sample that is too short causes poor resolution in the frequency response; on the other hand, a sample that is too long results in noise. Lastly, the spatial distribution of measurement nodes is dependent upon the highest mode shape to be captured. The rail testing shows that having a few measurement points outside of the target region can put the mode shapes in better context.

## 2. Experiment 2: Bridge Scale Model

Natural frequency identification and mode correlation can be quite subjective: mode shape plots assisted in these tasks, but much time was expended to analyze each potential resonance. In addition to the dense 55 measurement points on the target slab, the measurement on each approach slab proved very helpful in separating dissimilar modes. That is, local motions are better correlated to global motions through measurements of approach spans.

All natural frequencies decreased with increasing damage, but other resonant peaks can even appear or disappear. Modal coordination via deflected shape is vital to detecting damage location. Also, severe damage prevents coordination because the frequency response has experienced major shifts. This required the presented damaged case to use quite thin rubber to represent joint damage.

Low frequency rigid body translation modes and their directions can be used to identify potential sway weakness, a common failure mode for bridges. The strongest axis was the x-direction, which indicates good confinement in the longitudinal direction. Although the joint connections were strictly concrete, as-built imperfections in boundary conditions caused mode coupling.

Quantitative comparisons were performed with several damage indicating algorithms. The two best performers were the normalized modal flexibility index and the damage location vector. Each identified a concentration of y-direction damage near the artificially defective pier, where sway constraints were released. Each also showed fewer false positives, indicating good sensitivity for damage detection. The COMAC on mode curvature was somewhat acceptable since it demonstrated good sensitivity. Along with COMAC, absolute and percent differences on modal flexibility show a great sensitivity for not only damage but also false positives. Absolute difference, division, and total division on mode curvature did not show discernible results.

## 3. Experiment 3: Full Scale Bridge Test

The greatest lesson learned from the field vibration measurements on Eastgate Bridge regarded instrumentation. Girder measurements underneath the bridge with the LDV were much more successful, producing less noisy signals. Although the traditional sensors had cabling issues, the non-contact measurements were synchronous, even with a low power laser and, slightly lesser so, no applied reflector. These measurements were vertical at 10 meters, which is quite different than the deck measurements that required the LDV to be setup on an abutment. An LDV can measure only one vibration velocity component in the direction of the laser beam; the overall result of the low grazing angle of the LDV beam was vectorial signal interference that appeared as highly coupled signals. That is, the configuration does not allow measurements of separate vibration components of the bridge.

Field measurement required operation of an LDV at a standoff distance from 9 to 25 meters, which is within the standard range of the employed PDV 100. However, the maximum standoff distance also depends upon the properties of the object surface. Performance at long distances can be significantly affected by the small amount of reflected light. Laboratory tests were performed to evaluate velocity noise at different distances and reflecting surfaces. This LDV was capable of sensitive vibration measurements at ten meters without reflecting aids. With fine position adjustments, measurements on unconditioned metal, concrete, and gravel surfaces showed low noise floors at this distance. A cooperative retroreflector was necessary to enhance object reflectivity at a distance of more than ten meters. The prism increases the amount of light reflected back to the LDV and improves its efficiency and accuracy. Retroreflector use allowed low noise measurements up to 27 meters.

During in-service testing, the maximum amplitude from any sensor was 0.07g while the longest event was 15 seconds. The amplitude allows a comparison between the actual in-use bridge excitation and the scale model bridge laboratory excitation. Both the maximum amplitude and longest event length yield benchmark information regarding traffic excitation on an in-service bridge. Large spikes in the time history were attributed to settlement that had occurred on the abutments of the bridge. Excitation sources on full-scale structures are not uniform, and shock loads may result.

## 4. Structural Health Monitoring (SHM) Algorithm Development

The developed structural health program was initiated, and damage indicators were successfully explored herein. This program provides a new capability for the Multi Function

Dynamics Laboratory: future research will expand this competence. The most challenging part of the program is modal coordination, so the first developmental aspect will be additional features to make this less subjective.

Multiple schemes of signal filtering and windowing were added to the structural health program, but the best results occurred with data cleansing. Cropping greater magnitude events from a larger time history can clean up a signal by removing higher frequency noise. This requires that the sample length should be much longer than usually expected. Excessive cropping can also cause a loss of pertinent information that is present in the original signal.

## 5. Finite Element (FE) Modeling

The SAP2000 scale model bridge model was able to identify characteristic deck modes for the symmetric direct contact (no bearing) case. The mode shapes agree well with results of modal extraction from measurements. The natural frequencies are not identical due to contact surface modeling, and differences are easily eliminated by calibrating the modulus parameter for the artificial interaction frame elements.

A related characteristic bending mode was identified for the ABAQUS model of the center slab of the operational bridge. The significant skew affected the mode shape and girders present beneath the slab. The bending mode's frequency of the full-scale bridge versus the scale model is two orders of magnitude lower. The larger span and greater mass of real infrastructure lower natural frequency, and FE models account for scale as well as complex configurations (i.e., composite concrete deck slab and steel girders). The issue of scalability was addressed through the development of multiple finite element models and subsequent modal extractions. The quantitative relationship between damage and frequency for a characteristic mode involving vertical deck mass translation and associated deck bending was firmly established in (*20*). The effect of varying support stiffness in symmetric and asymmetric fashion was also studied through the variation of the artificial Young's modulus of the frame elements representing support bearings.

Lastly, the resonant frequency and mode shape of the full-scale composite deck model is comparable in magnitude to that of a previous model that included the adjacent spans and support substructure (*22*,*23*). A higher frequency was observed herein which is attributable to the interaction between the deck and other substructural components: mass and stiffness of bearings, columns, piers, footings, piles, and soil. The importance of modeling these details is highlighted in this work; an upcoming NCITEC 2013 project will address this in further detail.

# RECOMMENDATIONS

Overall recommendations from the integrated project are first presented herein. Additional recommendations are then provided from each of the five primary activities of the project.

A mobile vehicle equipped with at least one laser Doppler vibrometer (LDV) is worth investment by federal agencies. The precursory sensitivity studies herein demonstrate that the concept would work: an LDV moving on a vehicle can provide the dynamic characteristics of a bridge and its substructure. This product would be able to quantitatively gauge incremental damage, such as corrosion, without visual inspection. Rather than climbing into a lift, the operator could simply drive the vehicle over any bridge at inspection intervals, and an on-board screen would indicate where he/she should further examine. This would minimize traffic disturbance and bridge downtime while maximizing public safety and state resources. More research is needed to determine ideal vehicle configuration, vehicle suspension, and traveling speed as well as best indicators and environmental effects.

Condition-based maintenance in real-time is a large hurdle to overcome due to the nature of decision-making on both modal coordination and corrective action. Still, the developed health evaluation program can be augmented with these capabilities after more trials. For instance, perhaps practical real-time analysis could be achieved by the third bridge inspection over time. Civil infrastructure is an ideal damage detection application because it has small incremental changes as it deteriorates and ages.

Bridges are best tested in operational situations, but safety is a major concern. In-service traffic excitation is sufficient to provide modal information, and the best case would be multiple large vehicles traversing the bridge at various speeds. True ambient excitation may not provide enough frequency sensitivity to supply required mode shapes to locate damage.

Wind is often provides more excitation than a vehicle; however, a windy day can cause interference in the LDV signal. Air turbulence can affect optical measurements at long distances over 100 meters. Air turbulence can increase interference due to random variation of air's refractive index as well as speckle noise caused by beam wandering. While the reflected light can be sufficient with an unconditioned surface under normal circumstances, long distances will require cooperative retroreflectors, such as corner-cube prisms, tapes, and paints. Alternatively, an LDV with higher laser poser and larger aperture can be employed.

From the results of this project, several recommendations can be made regarding LDV use for infrastructure inspection. The overall result of a low grazing angle is signal interference that appears as highly coupled signals. This imposes limitations on setup geometry, so measurements from bridge abutments are likely to be unsuccessful if shooting

from a standard tripod from over ten meters (30 feet) away. It is also best for the LDV beam to coincide with vibration component of interest. For example, in order to measure bending (Z) component, the LDV should be located vertically over or under the bridge. Another limitation is the mechanical stability of the LDV itself. The LDV must be mounted on a mechanically stable platform, and any natural frequencies of the platform must be isolated before signal post-processing.

If stationary measurements are captured, the selected spatial resolution should be carefully selected based upon highest expected mode shape. An exhaustive search is not required, but a greater number of measurements near potential damage locations would provide better quantitative results. Additionally, a few extra measurements outside the target zone (on any attached approach) prove extremely beneficial in modal decomposition.

Care must be taken in sensor selection. Specifically, sensitivity can generate additional noise (if too sensitive) or can cause information loss (if too insensitive). Sensor drift drastically affects frequencies below 5 Hz, so low frequency response of the sensor must be evaluated. Any sensors should also be given adequate time for the signals to level out before recording signals. Cabling must be robust. Any significant motion during measurement can cause data stream loss. Coupling of sensor(s) leads to false excitation readings by transferring a percentage of the excitation from one to another that should not be excited. Coupled modes may be magnified by geometry, so sensors should be carefully aligned in the field. The instrumentation scheme should be quality-tested before taking field data.

1. Experiment 1: Non-Contact Rail Inspection

The traveling velocity of the LDV needs further examination. This initial study's slow speed is impractical, and greater speeds may introduce more interference and reduce sensitivity. Also, the use of multiple LDV beams may be advantageous and is the focus of a 2014 NCITEC research effort.

2. Experiment 2: Bridge Scale Model

Necessary experimental study is underway via a M.S. thesis and a Ph.D. dissertation. Various damage cases are being examined with the goal of identifying damage after abnormal events. Incremental damage has been identifiable herein, but significant damage could be inflicted in one large shock, such as an earthquake or an accident. The undamaged or baseline modes must be matched to similar modes for the damaged case; if the "damage" or differences are too great in the modes, their coordination is not evident, which could lead to false positives on damage indication. Thus, the challenges in mode coordination require

more attention to reduce subjectivity.

Briefly, the finite element model effort has shown that mode shapes can be approximated. These modes can be used as a baseline case in the health program, but any modeling variation reduces damage detection sensitivity and increases the possibility of false positives. Better guidance in model building, especially at supports, is mandatory before a modeled mode shape can be employed as a baseline. The potential benefits are certainly worthwhile: just post-event measurements would be required.

## 3. Experiment 3: Full Scale Bridge Test

The aforementioned recommendations on LDV use stem from the Eastgate Bridge test. The various configurations require further study to estimate speckle noise effects on detection of structural defects.

Adjustments can be made to improve the success of remote vibration measurement of bridge decks: enforce a high grazing angle (ideally right angle), exploit multiple measurements, or select a different instrument. LDV model RSV-150 is recommended as better remote inspection on bridge decks due to higher laser power and larger receiving aperture.

Measurements underneath the bridge provided excellent frequency spectra. Direct shots and shorter distances allowed major vibrations to be successfully captured both with and without a retroreflector. Thus, the non-contact LDV can replace contact accelerometers in bridge vibration measurements of girders, whose unconditioned surface reflected sufficient light. Corroded or dirty members may require surface conditioning or the more powerful RSV-150.

Note that traditional cabled instrumentation has the additional disadvantage of signal dropout due to cord motion. Wireless data acquisition systems are becoming more widely available but they still have contact and interference disadvantages. The non-contact LDV is a more feasible alternative.

## 4. Structural Health Monitoring (SHM) Algorithm Development

Research is proceeding towards finding the damage indicators that work best for different classes of structures. The health program outputs several different metrics, but which (or which combination) is preeminent for any bridge or even any structure. Various materials and geometries are also expected to affect damage detection. Once the most effective indication method is selected, the damage thresholds need identification for decision-making. Safety thresholds can then be used for maintenance decision-making.

As discussed herein, several technical programming challenges need further study. Mode coordination must be augmented for large damage events and to deliver real-time results. True ambient excitation and associated signal processing could boost sensitivity.

After all technical challenges are resolved, a user interface must be added to the completed health program. It must be tested by state inspectors before any chance of implementation.

## 5. Finite Element (FE) Modeling

Overall, finite element modeling is sensitive enough to capture modal changes due to damage. The applicability of results is limited by restraint idealization, connectivity assumptions, and input properties. If these modeling assumptions agree with the experimental system, it is possible to verify the effects of damage. However, these model parameters are often difficult to identify. Knowledge of damage mechanisms and construction details should be established so that the modeling can provide insight into how specific local damage can affect global structural motion. For instance, the composite deck construction herein behaves as a stiffened plate, but other configurations may respond differently. Nonetheless, the results of this integrated project show promise for FE analysis to supplement vibration measurements and mode coordination.

System variability and damage levels are a focus of a 2013 NCITEC research effort. It is also recommended that future modeling work examine damage threshold sensitivity, a key to practical applications in operating environments.

The current scale bridge study includes a very limited scope of finite element model analysis: modal comparison of model to experiment. The limited analysis reveals the complexity in even a simple geometry bridge structure comprised flat slabs and vertical panels. The support conditions used to simulate damage at various levels further complicate the modal characteristics, causing frequency shifts that require additional study. This has practical implications for broader infrastructure applications and damage identification automation.

Despite the narrow focus, this project highlights the complexity of the operational bridge environment. A more robust study should be conducted to develop suitable finite element models for establishing current and progressive damage states of operational bridges. Such a study should examine various contributing factors including material degradation, substructural systems, and soil conditions. These specific details are influential, as shown by the prior to current study comparison. The differences in modal properties depend a great deal upon component, interaction, and connectivity details as well as different model features for specific operating environments.

# ACRONYMS, ABBREVIATIONS, AND SYMBOLS

| | |
|---|---|
| A | cross-sectional area |
| a.u. | amplitude units |
| A/D | analog/digital |
| ABAQUS | General purpose commercial finite element program; also ABAQUS/CAE |
| ACI | American Concrete Institute |
| AISC | American Institute for Steel Construction |
| ASCE | American Society of Civil Engineers |
| ASTM | American Society for Testing and Materials |
| cm | centimeter(s) |
| COMAC | Coordinate Modal Assurance Criterion |
| DLV | Damage Location Vector (DLV) |
| DOF | degree(s)-of-freedom |
| E | material modulus of elasticity |
| $E_c$ | Young's modulus for concrete |
| $f_c'$ | concrete yield strength from cylinder test |
| FE | finite element |
| $F_{ij}$ | proportional flexibility matrix |
| ft, ' | foot (feet) |
| g | acceleration unit of 9.8 m/s$^2$ or 32.2 ft/s |
| Hz | Hertz |
| i,j,k,m | indices for summations |
| I | second area moment of inertia |
| in, '' | inch(es) |
| k | bearing stiffness |
| ksi | kips per square inch, or 1000 pounds per square inch |
| L | characteristic linear dimension, i.e. height or length |
| LabVIEW | Commercial software of virtual instrumentation by National Instruments |
| lb | pound(s) |
| LDV | Laser Doppler Vibrometer |
| m | meter(s) |
| MAC | Modal Assurance Criteria |
| MFI | Modal Flexibility Index (MFI) |
| mm | millimeter(s) |
| mV | millivolt(s) |
| NCPA | National Center for Physical Acoustics |
| NI | National Instruments |
| PC | personal computer |
| psi | pounds per square inch |
| s | second(s) |
| SAP2000 | Commercial finite element program geared toward structural engineers |
| $^T$ | matrix transpose |

| | |
|---|---|
| Typ. | Typical, as in an engineering drawing |
| V | volt(s) |
| $\mathbf{V}$ | total velocity vector (boldface) |
| $\mathbf{V_x}$ | x-component of velocity (boldface) |
| $\mathbf{V_z}$ | z-component of velocity (boldface) |
| UM | The University of Mississippi |
| ZMFI | Normalized Modal Flexibility Index |
| 3D | three-dimensional |
| 4.8E5 | example of exponential form, i.e. $4.8 \times 10^5$ |
| $\alpha$ | grazing angle of the LDV beam |
| $\nu$ | material Poisson's ratio |
| $\phi_i$ | undamaged mode shape for the *i*th mode; baseline modal deflections |
| $\phi_i^*$ | damaged mode shape for the *i*th mode; damaged modal deflections |
| $\phi_{ij}$ | single location *j* in undamaged mode shape for the *i*th mode |
| $\phi_{ij}^*$ | single location *j* in damaged mode shape for the *i*th mode |
| $\omega_i$ | natural frequency of the *i*th mode |

# REFERENCES


1. Kaewunruen, S., and Remennikov, A.M. “Non-destructive Evaluation for Dynamic Integrity of Railway Track Structure.” Proceedings of the International Conference on Structural Integrity and Failure, Sydney, Australia, Sept. 27-29, 2006, pp. 294-299.
2. Kaewunruen, S., and Remennikov, A.M. “An Alternative Rail Pad Tester for Measuring Dynamic Properties of Rail Pads Under Large Preloads.” Experimental Mechanics, Vol. 48, 2008, pp. 55-64.
3. Kaewunruen, S. and Remennikov, A.M.. “Application of Vibration Measurements and Finite Element Model Updating for Structural Health Monitoring of Ballasted Railtrack Sleepers with Voids and Pockets.” Sapri, R.C.(ed), Mechanical Vibration: Measurement, Effect, and Control, Nova Science Publishers, New York, 2009, pp.621-644.
4. Kaewunruen, S. and Remennikov, A.M. “Dynamic Properties of Railway Track and its Components : A State-of-the-art Review.” Weiss, B.N. (ed) New Research on Acoustics, Nova Science Publishers, Hauppauge, New York, 2008, pp. 197-220.
5. Kaewunruen, S, and Remennikov, A.M. “Dynamic Properties of Railway Track and its Components : Recent Findings and Future Research Directions.” Insight: Non-Destructive Testing and Condition Monitoring, Vol. 52, No. 1, 2010, pp. 20-22.
6. Kaewunruen, S, and Remennikov, A.M. “Dynamic Effect on Vibration Signatures of Cracks in Railway Prestressed Concrete Sleepers.” Advanced Materials Research, Vols. 41-42, 2008, pp. 233-239.
7. Kaewunruen, S, and Remennikov, A.M. "Laboratory Measurements of Dynamic Properties of Rail Pads under Incremental Preload." 19th Australasian Conference on the Mechanics of Structures and Materials, Nov. 29 – Dec. 1, 2006, Christchurch, New Zealand, pp. 319-324.
8. Kaewunruen, S, and Remennikov, A.M. “Monitoring Structural Degradation of Rail Bearing Pads in Laboratory using Impact Excitation Technique.” 1st International Conference on Structural Condition Assessment, Monitoring, and Improvement, Perth, Australia, Dec. 12-14, 2005, pp. 399-405.
9. Kaewunruen, S, and Remennikov, A.M. “Non-destructive Testing (NDT): A Tool for Dynamic Health Monitoring of Railway Track Structures.” Materials Australia, Vol. 39, No. 6, 2006, pp. 14-16.
10. Nassifa, H.H., Gindyb, M., and Davis, J. “Comparison of Laser Doppler Vibrometer with Contact Sensors.” NDT&E International, Vol. 38, 2005, pp. 213-218.
11. Miyashita, T., Ishii, H., Fujino, Y., Shoji, A., and Seki, M. “Clarification of the Effect of High-Speed Train Induced Vibrations on a Railway Steel Box Girder Bridge Using Laser

Doppler Vibrometer." Experimental Vibration Analysis for Civil Engineering Structures, 2005, pp. 349-357.
12. Rezaei, D., and Taheri, F. "A Novel Application of a Laser Doppler Vibrometer in a Health Monitoring System." Journal of Mechanics of Materials and Structures, Vol. 5, No. 2, 2010, pp. 289-304.
13. Miyashita, T., and Nagai, M. "Vibration-based Structural Health Monitoring for Bridges using Laser Doppler Vibrometers and MEMS-based Technologies." Steel Structures, Vol. 8, 2008, pp. 325-331.
14. Farrar, C.R., Cornwell, P.J., and Doebling, S.W. Structural Health Monitoring Studies of the Alamosa Canyon and I-40 Bridges, LA-13635-MS, Los Alamos National Laboratory Report, 2000.
15. Pavic, A., Pimentel, R., and Waldron, P. "Instrumented Sledge Hammer Impact Excitation: Worked Examples." International Modal Analysis Conference, 1998, pp. 929-935.
16. Aranchuk, V., Lal, A.K., Hess, C.F., Sabatier, J.M., Burgett, R.D., Aranchuk, I., and Mayo, W.T. "Speckle Noise in a Continuously Scanning Multibeam Laser Doppler Vibrometer for Acoustic Landmine Detection." Proceedings of the SPIE, Vol. 6217, Orlando, April 2006, pp. 621716-1.
17. Aranchuk, V., Sabatier, J.M., Lal, A.K., Hess, C.F., Burgett, R.D., and O'Neill, M. "Multi-beam Laser Doppler Vibrometry for Acoustic Landmine Detection using Airborne and Mechanically-coupled Vibration." Proceedings of the SPIE, Vol. 5794, Orlando, March 2005, pp. 624-631.
18. Computers and Structures, Inc. SAP2000 user manual, Version 15. Berkeley, California, 2011.
19. Ferrar, C.R. Structural Health Monitoring Course, Los Alamos Dynamics, Sept. 6-8, 2009.
20. Bethay, J.K. "FE Modeling in Support of Vibration Based Damage Detection in Bridges." Thesis, Master of Science in Engineering Science with Emphasis in Civil Engineering, Department of Civil Engineering, University of Mississippi, Aug. 2013.
21. American Concrete Institute. Building code requirements for the design of concrete structures, Standard ACI 318-11, ACI 2011.
22. Swann, C., R. Hackett, C. Mullen, C. Lutken, and R. Stewart. "Evaluation of Earthquake Effects on Selected Structures and Utilities at the University of Mississippi: A Mitigation Model for Universities." Final Report submitted to Mississippi Emergency Management Agency, Department of Civil Engineering and Mississippi Mineral Resources Institute, The University of Mississippi, Dec. 1999.

23. Mullen, C. and Swann C. “Seismic Response Interaction between Subsurface Geology and Selected Facilities at the University of Mississippi,” Engineering Geology, Vol. 62, 2001, pp. 223-250.
24. Hibbitt, Karlsson, and Sorenson, Inc. ABAQUS theory manual. Version 5.6. Providence, Rhode Island, 1996.
25. Hibbitt, Karlsson, and Sorenson, Inc. ABAQUS CAE user manual. Dissault Systemes Simulia Corp. Version 6.12. Providence, Rhode Island, 2011.
26. American Institute for Steel Construction. Steel Construction Manual, 14th edition, AISC 2010.
27. Pandey, A. K., Biswas, M., and Samman, M. M. “Damage Detection From Changes in Curvature Mode Shapes.” Journal of Sound and Vibration, Vol. 145, No. 2, 1991, pp. 321-332.
28. Heo, G. H., Lee, G., Hyun, D. Y., Choi, M. Y., and Lee, M. W. “Structural Health Monitoring Systems for A Steel Structure Using An Ambient Vibration.” Key Engineering Materials, Vols. 297-300, 2005, pp. 2102-2108.
29. Huth, O., Feltrin, G., Maeck, J., Killic, N., and Motavalli, M. “Damage Indication Using Modal Data: Experiences on a Prestressed Concrete Bridge.” Journal of Structural Engineering, Vol. 131, No. 12, 2005, pp. 1898-1910.
30. Sun, Z. G., Ko, J. M., and Ni, Y. Q. “Modal Indices for Identifying Damage Location in Cable-Stayed Kap Shui Mun Bridge.” Health Monitoring and Management of Civil Infrastructure Systems, Vol. 4337, 2001, pp. 379-389.
31. Baghiee, N., Esfahani, M. R., and Moslem, K. “Studies on Damage and FRP Strengthening of Reinforced Concrete Beams by Vibration Monitoring.” Engineering Structures, Vol. 31, 2001, pp. 875-893.
32. Huynh, D., He, J., and Tran, D. “Damage Location Vector: A Non-destructive Structural Damage Detection Technique.” Computers and Structures, Vol. 83, 2005, pp. 2353-2367.
33. Drain, L.E. The Laser Doppler Technique. John Wiley & Sons, Inc., New York, 1980.

# APPENDIX

Gigabytes of text data was logged during this report. Data is stored for each of the three experimental efforts by the researchers, and the PI is maintaining copies for a minimum of five years. Any requests for the data should be directed to Dr. Ervin at eke@olemiss.edu.

Additional information can be obtained from the publications resulting from this grant. Cumulative external citations are as follows:

Elizabeth K. Ervin, "Algorithm Comparison for Structural Health Metrics," BP133, 2013 Structures Congress, ASCE Structural Engineering Institute, Pittsburgh, PA, May 2-4, 2013. *Presented on May 2.*

Steven B. Worley and Elizabeth K. Ervin, "A Comparison of Structural Health Indicators," RAM Workshop, Society of Reliability Engineers, Huntsville, AL, October 16-17, 2012. *Presented by Worley on Oct 17; second place student presentation.*

James Kyle Bethay, Master's thesis, "FE Modeling in Support of Vibration Based Damage Detection in Bridges," August 2013.

Steven B. Worley and Elizabeth K. Ervin, "Field Testing of the Ford Center Bridge," Mid-South Annual Engineering and Sciences Conference, Oxford, Mississippi, October 28-29, 2013.

Elizabeth K. Ervin, "Three Experimental Applications of Health Algorithms to Improve Infrastructure Inspection," European Workshop on Structural Health Monitoring, July 2014. Abstract submitted.

Steven B. Worley and Dr. Elizabeth K. Ervin, "Considerations on vibration testing techniques of an in-service highway bridge," Journal of Bridge Engineering (in final preparation, submission by January 31, 2013).

Vyacheslav Aranchuk and Elizabeth K. Ervin, "Dynamic Evaluation of Structural Integrity of Railway Tracks using Laser Doppler Vibrometry," NDT & E International (in preparation).

## Experimental Scale Bridge Modes

| Frequency (Hz) | Mode Type | Description |
|---|---|---|
| 9.47 | Translation | Translation in the y-direction and z-direction - Only slight rigid body motion |
| 12.23 | Translation | Translation in the y-direction - no other motion - rigid body |
| 15.96-27.91 | Local | Slab Distortion - local corner motion modes |
| 38.75 | Translation | Outer slab mode - center barely has motion |
| 60.05 | Torsion & Translation | Torsion about the x-axis and translation in the y-direction |
| 64.17 | Torsion & Translation | Torsion about the x-axis and translation in the y-direction |
| 68.55 | Torsion & Translation | Torsion about the x-axis and translation in the y-direction - coupled |
| 74.31 | Torsion & Translation | Slight torsion about the x-axis and translation in the y-direction |
| 75.73 | Torsion & Translation | Slight torsion about the x-axis and translation in the y-direction |
| 78.23 | Torsion | Torsion about the x-axis and torsion about the z-axis (except for no motion at bottom left corner) |
| 80.47 | Torsion | Torsion about the z-axis - weak |
| 98.92 | Torsion & Bending | Strong torsion around the z-axis and bending in the positive z-direction |
| 100.44 | Torsion & Bending | Weaker torsion around the z-axis and bending in the positive z-direction |
| 101.73 | Bending | Bending in the positive z-direction with maximum shifted to the right side - some slab distortion present |
| 106.00 | Bending | Bending in the positive z-direction with maximum shifted to the right side - leftmost points in the x-direction stretch (slab distortion) |
| 114.63 | Torsion & Bending | Torsion about the z-axis but fixed bottom left - bending in the z-direction |
| 131.18 | Translation & Bending | Bending in the negative z-direction with translation in the negative x-direction (magnitude increases in the positive y-direction) - end slabs move up (left side) and down (right side) |
| 132.60 | Translation & Bending | Bending in the negative z-direction with translation in the negative x-direction (same magnitude) - end slabs move up (left side) and down (right side) |
| 140.16 | Bending | Bending in the negative z-direction with translation of the top half in the y-direction (slab endpoints in the x-direction move inwards) - end slabs both move up |
| 152.28 | Bending & Translation | Bending in the negative z-direction with translation in the y-direction - end slabs both move up slightly - also x points move inwards (compression) |
| 153.83 | Bending & Torsion | Bending in the negative z-direction with torsion about the z-axis - end slabs move up (right) and down (left) but only slightly |
| 178.39 | Bending, Torsion, & Translation | Bending in the positive z-direction, torsion about the y-axis and x-axis, and translation in the negative x-direction |
| 199.79 | Bending & Translation | Bending in the positive z-direction with translation in the positive y-direction (bending increases slightly along the positive y-direction) - both end slabs translate opposite of the center slab in the negative y-direction |
| 201.06 | Bending & Translation | Bending in the positive z-direction with translation in the positive y-direction (bending increases slightly along the positive y-direction) - both end slabs translate opposite of the center slab in the negative y-direction |

Experimental Scale Bridge Modes *(continued)*

| Frequency (Hz) | Mode Type | Description |
|---|---|---|
| 202.57 | Bending & Translation | Bending in the positive z-direction with translation in the positive y-direction - both end slabs translate opposite of center slab in the negative y-direction |
| 211.70 | Local Bending | Slab Distortion - local corner motion with slight bending in the z-direction |
| 217.20 | Translation & Torsion | Torsion about the z-axis (positive) and translation in the y-direction - end slabs translate opposite of center slab in the positive y-direction (also bending in the positive z-direction along y = 0 line) |
| 224.41 | Bending | Bending in the positive z-direction until midspan where the bending is near 0 and then bending in the negative z-direction - also torsion about the negative x-axis (some slab distortion) |
| 230.23 | Bending | Bending in the positive z-direction until midspan where the bending is near 0 and then bending in the negative z-direction - center slabs translate opposite of one another (some slab distortion) |

## Eastgate Bridge Modes via Finite Element Model

| Frequency (Hz) | Brief Description |
|---|---|
| 4.9876 | Bending about transverse direction |
| 5.406 | Combined bending and torsion |
| 9.2086 | Bending about longitudinal direction |
| 14.87-16.79 | Coupled deck and girder bending |
| 24.09 | Major deck bending |
| 24.39 | Minor deck bending |
| 28.79 | Major deck bending |
| 32.06 | Major deck bending |
| 37.07 | Major deck bending |
| 41.31-41.55 | Major deck bending |
| 42.85 | Major deck bending |
| 44.06 | Major deck bending |
| 44.78 | Major diagonal deck bending |
| 49.61 | Major deck bending |
| 52.27 | Major diagonal deck bending |
| 54.42 | Major diagonal deck bending |